Czech Technical University in Prague

Faculty of Biomedical Engineering

Doctoral Thesis

April 2020

Ing. Ondřej Klempíř

Dissertation Thesis

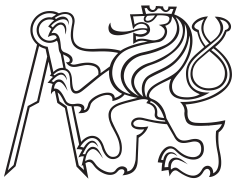

Czech Technical University in Prague

F7

Faculty of Biomedical Engineering
Department of Biomedical Informatics

Analysis of Neural Activity in the Human Basal Ganglia: From Micro to Macro

Ing. Ondřej Klempíř

Supervisor: Mgr. Radim Krupička, Ph.D.
Supervisor–specialist: prof. MUDr. Robert Jech, Ph.D.
Supervisor–specialist: Mgr. Tomáš Sieger, Ph.D.
Ph.D. programme: Biomedical and Clinical Technology
April 2020

Acknowledgements

First of all, thank you to my supervisor, Radim Krupicka, Ph.D., for providing guidance and feedback throughout this thesis. I would also like to acknowledge the co-supervisors and the Department of Biomedical Informatics for their engagement in the study.

I cannot forget to thank my family and friends for all the support.

I would like to express my gratitude to my already deceased relatives and pets who support me spiritually through my life and Ph.D.

And finally, I would like to dedicate this thesis to my beloved Kateřina, because being thankful is not simply enough here... She always understands.

Declaration

I hereby declare that I have written this thesis myself as a result of my original research (or as the co-author of research papers).

All sources of information have been properly stated and referenced.

In Kladno,

In partial fulfillment of the requirements for the degree of Ph.D.

Abstract

Deep brain stimulation (DBS) of the human basal ganglia is an internationally accepted form of treatment option for selected patients with movement disorders. Analysis of brain activity associated with the human basal ganglia is needed at both micro and macro levels. For example, knowledge of micro activity is important for the precise positioning of the DBS electrode into the target brain structure. Moreover, exploring the links between stimulation states and the effect of DBS on motor cortex activity is key to understanding the pathophysiological mechanisms of movement control, as well as the function of its treatment.

The analysis of neurophysiological recordings in the field of neuromodulation, consisting of multiple spatial and temporal scales, is a computationally and conceptually complex task with multiple sources of error and bias that can affect subsequent data interpretation. Additionally, current analysis workflows lack standardisation. Specific biomarkers may help determine targets and patient-specific protocols for neuromodulation therapy of patients with dystonia or Parkinson's disease.

The overall aim of this dissertation is to implement, validate and apply computational algorithms for a complex evaluation of the neuronal recordings originated from the field of neuromodulation. The dissertation is based on a collection of papers which can be associated with three main themes:

1) Development of a comprehensive pipeline for signal preprocessing and computation of the descriptive parameters from the neuronal microrecordings.

2) Designation of novel biomarkers and statistical methods for the identification of dystonia patients responding to the DBS of the Globus Pallidus internus.

3) Provision of more macroscopic insights into understanding of the pathophysiological DBS mechanisms via a near-infrared spectroscopy imaging in patients with microelectrode recording-guided targeting of the subthalamic nucleus.

The individual results chapters are devoted to the classification of microelectrode artifacts by means of convolutional neural network, evaluation of the software tools for automatic spike detection and sorting, test the tools on the large set of real neuronal spiking data, identification of microrecording features as the interoperative markers for dystonia and finally, how DBS affects the patterns of cortex activation in simple motor task and gait. In the course of this dissertation, the R/Shiny web application was developed for the integration and analysis of neural data.

On the micro-level, the general findings indicated the significant correlations of the microrecording biomarker with the long-term DBS effect and contact localization along the medio-lateral direction in dystonia. On the macro-level, we found that DBS performed during simple motor task led to an increase in the activity of the contralateral motor cortex areas and increased activity near the longitudinal fissure during gait.

We assume that this research will contribute to a better understanding of the underlying mechanisms of DBS.

Keywords: electrophysiology, microrecording, spike sorting, digital biomarkers, neuromodulation, deep learning, basal ganglia, near infrared spectroscopy

Abstrakt

Hluboká mozková stimulace (DBS) lidských bazálních ganglií je mezinárodně uznávanou léčebnou metodou pro vybrané pacienty s poruchami pohybu. Analýza aktivity mozku související s oblastí bazálních gangliích je nutná na mikro i makroskopické úrovni. Znalost mikroskopické aktivity je například důležitá pro přesné zavedení DBS elektrod do cílových hlubokých struktur mozku. Neméně důležitý je rovněž výzkum efektu stimulačních stavů DBS na obraz aktivity motorické mozkové kůry, což je klíčové pro pochopení patologických mechanismů řízení pohybu a případné léčby.

Pokročilá analýza neurofyziologických záznamů v oboru neuromodulační terapie, zahrnující širokou škálu prostorových i časových měřítek, je výpočetně i koncepčně náročnou úlohou, která je vystavena různým zdrojům chyb komplikujících následnou interpretaci dat. Současné analýzy také typicky postradájí standardizaci. Specifické biomarkery mohou pomoci stanovit zacílenou terapii a personalizované protokoly pro DBS u pacientů s dystonií či Parkinsonovou nemocí.

Cílem dizertační práce je implementace, validace a aplikace výpočetních nástrojů pro komplexní hodnocení neurálních záznamů pocházejících z oblasti neuromodulační terapie. Tato práce je založena na publikační činnosti autora, kterou lze rozlišit do tří hlavních oblastí:

1) Vývoj metodického řetezce pro předzpracování a výpočet popisných parametrů v neuronálních mikroelektrodových záznamech.

2) Návrh nových biomarkerů a statistických metod pro identifikaci dystonických pacientů odpovídajích na léčbu DBS.

3) Vhled do makroskopických poznatků za účelem popisu patofyziologických mechanismů DBS metodou funkční blízké infračervené spektroskopie u pacientů, kterým byla DBS implatována na základě analýzy mikroelektrodových záznamů.

Jednotlivé originální kapitoly jsou věnovány klasifikaci artefaktů v mikroelektrodových záznamech s využitím konvolučních neuronových sítí, hodnocení softwarových nástrojů pro automatickou detekci a třídení akčních potenciálů v extracelulárních záznamech a testování nástrojů na rozsáhlé databázi reálných dat. Dále identifikace mikroelektrodových příznaků jako interoperační markery pro dystonii a v neposlední řadě, jak DBS ovlivňuje aktivační vzory motorické kůry při jednoduchém pohybu ruky a při chůzi. Mezi další výstupy patří R/Shiny webová aplikace, která byla vyvinuta pro integraci a analýzu neurálních dat.

Z hlediska aktivity na mikro úrovni, výsledky ukázaly významný vztah mezi mikroelektrodovou aktivitou a klinickým účinkem DBS včetně korelace s umístěním DBS elektrody v medio-lateralním směru u dystonií. Na makro úrovni jsme pak našli asociaci, kdy DBS aplikovaná při pohybů prstů vedla k narůstu aktivity kontralaterální motorické kůry a ke zvýšení aktivity v blízkosti oblastí vertexu při chůzi.

Předpokládáme, že tato práce přispěje k lepšímu pochopení mechanismů při hluboké mozkové stimulaci.

Klíčová slova: elektrofyziologie, mikroelektrodové záznamy, třídění neuronů, digitální biomarkery, neuromodulace, hluboké učení, bazální ganglia, blízká infračervená spektroskopie

Contents

Figures

Tables

Part I

Problem Context

Chapter 1

Introduction

The World Health Organization has recorded an increasing incidence of neurological diseases. More than 50 million Europeans suffer from neurological disease, costing nearly 400 billion euros per year in the European Union [1]. Data obtained during multiscale investigations of the (patho)physiological processes of the brain has increased. Several approaches can be used to study the nervous system—one of them is sensing action potentials on the surface of a nerve cell membrane using electrodes (Fig. 1.1).

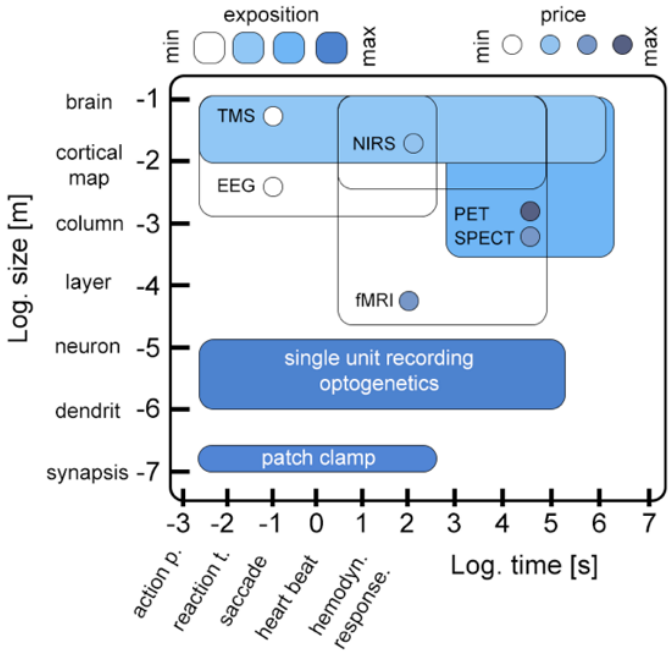

Figure 1.1: Approximate ranges of spatiotemporal sensitivity of neural measurement techniques. Importantly, single unit approaches can measure and control a range of spatiotemporal organization relating to individual neurons and dendrites. Created with inspiration from [2], with quoting.

A lot of neuroscience departments across the globe investigate the pathophysiology associated with movement disorders. According to the recent

opinions, research in differentiating disease states took a great leap forward with the advent of popular neuroimaging methods, which would be an example of measuring macro properties of the brain, at a global level. Showing different patterns of activity (increased or decreased) of certain regions of the brain might explain the pathophysiology. The researchers further suggest the appropriate level to understand higher cortical functions is based on interaction with subcortical structures consistent with views that higher functions can only be understood as a whole-brain activity.

A similar view can be held of electroencephalography/local-field-potential recordings at the macro/mid levels which sum the activity of many cell assemblies, which also has been around for much longer. Pathophysiology may involve both individual neurons and a host of projection from multiple structures. However, to really understand the pathophysiology, as well as the impact of a stimulation intervention, one must go to the micro level, i.e. single unit analysis.

Single unit activity is a navigation tool for deep brain stimulation surgery and it is necessary to recognize and describe involved neurons, which is a conceptually difficult task. This requires emphasizing the development of methods to better describe individual neurons.

New knowledge of the function of the nervous system has been discovered from applying analytical computational methods to the data. It turns out that computer learning and prediction are able to distinguish a healthy control from pathology more accurately than an expert in some diseases based on extracted features and biomarkers [3]; and has the ability to predict, for example, a response to treatment [4]. For instance, most people know IBM for its artificially intelligent supercomputer Watson (now less quiz show champion and more medical genius). It is believed that IBM Watson may soon be the world's best diagnostician. Watson is already capable of storing more medical information than doctors (40 milion of scientific documents in 15 seconds), and unlike humans, its decisions are all evidence-based and free of cognitive biases and overconfidence [5].

Digital biomarkers are consumer-generated physiological and behavioral measures collected through connected digital tools that can be used to explain, influence and/or predict health-related outcomes (Fig. 1.2). Health-related outcomes can vary from disease explanation to drug response prediction [6]. According to the NIH, biomarkers are objectively measured and evaluated indicators of normal biological processes, pathogenic processes, or pharmacologic responses to a therapeutic intervention [7].

Machine learning, artificial intelligence, and deep learning are revolutionizing the field of neuroscience by enabling machines to detect complex patterns and create interpretable models revealing biological mechanisms. Using machine learning, we can analyze neuroscientific data to provide a better understanding of both the normal and pathological processes in brain disorders.

The overall aim of this dissertation is to implement, validate and apply computational algorithms for a complex evaluation of the neuronal record-

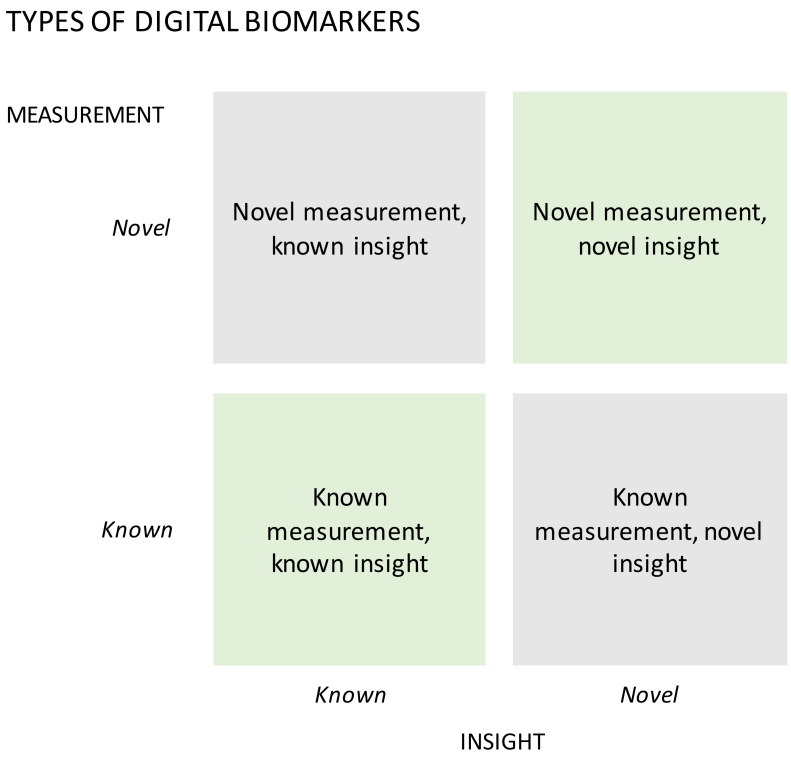

Figure 1.2: Digital biomarkers are classified by novelty in measurement and insight [6].

ings originated from the field of neuromodulation. The main focus of this dissertation research is on data collected from both clinical (Department of Neurology and Center of Clinical Neuroscience, First Faculty of Medicine and General University Hospital, Charles University, Prague) and the public research institutes of the Czech Academy of Sciences (Institute of Physiology, Institute of Physics).

The topicality of the thesis is also reflected in the annual chart The Digital Health Hype Cycle 2020 (Fig. 1.3). A hype cycle is a branded graphical presentation developed and used by the American research, advisory and information technology firm Gartner for representing the maturity, adoption and social application of specific technologies. The hype cycle provides a graphical and conceptual presentation of the maturity of emerging technologies through five phases. [8]

1.1 Structure of the Thesis

The topic of the thesis is introduced in Chapter 1, including the motivation. It is followed by a detailed state-of-the-art (Chapter 2), which introduces the reader to the necessary theoretical background and surveys current

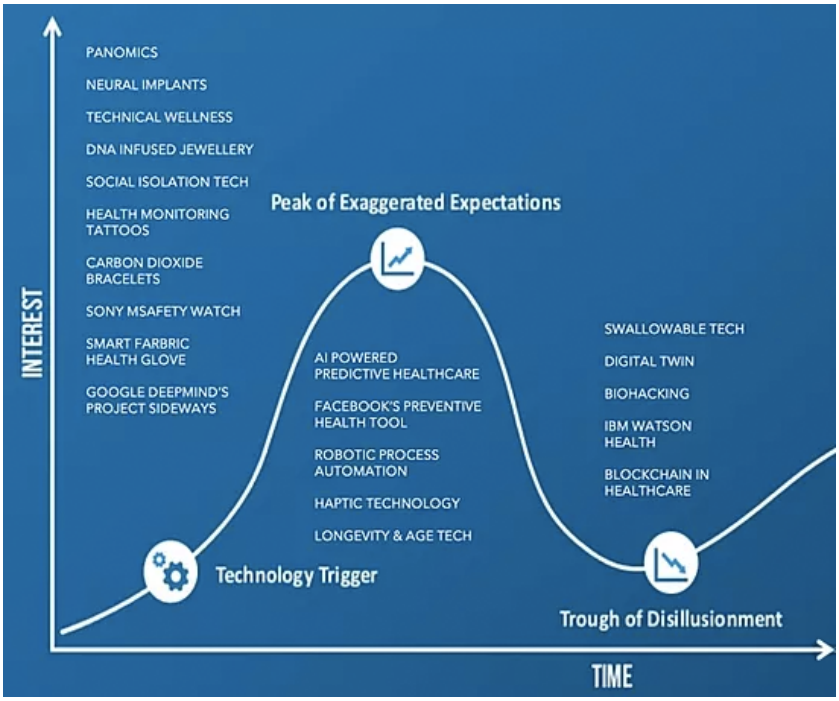

Figure 1.3: Many new neurotechnologies are on the rise. In the context of this thesis I emphasize the following: neural implants (Neuralink)—an American neurotechnology company founded by Elon Musk, reported to be developing implantable brain-computer interfaces, a direct communication pathway between brain and an external device [8].

research. Based on selected electrophysiological methods, state of the art and expertise consultations, I defined the aims of the thesis and formulated the research objectives. Chapter 3 is subjected to a more detailed formulation of the goals of the work. Chapters 4, 5 and 6 deal with the overview of proposed approaches and methodological results. For the purpose of deep brain stimulation, individual neurons need to be detected and described, which is not an easy task. Thus, the proposed algorithms in Chapter 4 and 5, based on the microelectrode array measurements, have shown a great success in extracting various extracellular shapes from the real neurons. It is mainly based on author's publications. Then, the proposed and developed microelectrode biomarkers for an analysis of deep brain stimulation are presented. In Chapters 7 and 8, a set of investigated patients and pilot clinical results of the dissertation are described. The proposed approaches are demonstrated using real datasets. At the end, I summarize the results and suggest possible topics for further research (Chapter 9). The developed R Shiny web application for the integration and analysis of neural data is introduced in the Appendix A section.

Chapter 2

State of the Art

The aim of this chapter is to provide an overview of state-of-the-art approaches for acquisition and processing of neurophysiological recordings from the human basal ganglia; e.g. in order to define biomarkers to identify patients who will benefit from clinical deep brain stimulation. For this purpose, the essential elements of microelectrode processing are examined. Among others, I describe baseline elements of microrecording processing including data collection, preprocessing phase, features computation, spike detection and sorting and advanced spike train data analysis. This chapter will help readers acquire the necessary information about the relevant medical and technical topics which will be needed to understand the rest of this thesis. Thus, this part is supposed to assist during identification and proposal of interesting clinical hypotheses.

2.1 Overview from Micro to Macro

The nervous system is the most comprehensive information processing system. The basic unit of all vertebrate nervous tissue is the neuron. The neuron is electrically excitable and processes information through electrical and chemical signals. Such signals are transmitted between neurons by electrical or neurochemical synapses, causing interconnections and forming neural networks. Each of the neurons consists of dendrites that receive an electrochemical signal from other neurons, a cell body (soma), a nucleus, and an axon that transmits electrochemical information to other neurons (Fig. 2.1A).

An electrical action potential is a short time event during which a rapid increase and subsequent decrease back to the cell membrane potential occurs (Fig. 2.1B). The action potential travels along the axon due to polarity changes in the membrane. First, the Na+ channels open and the ions flow into the axon and induce depolarization. Upon opening of the K+ channels and their flow from the axon, repolarization occurs. This changes the polarity between the external and internal environment of the cell. The impulse on the axon always travels in one direction to the places where the axon

branches and transfers the signal to another neuron [9]. An equally important component of neural activity is neurochemical activity. A vast array of neurochemical markers and corresponding expression information can be used in brain research, reflecting its developmental and pathological roles. [10]

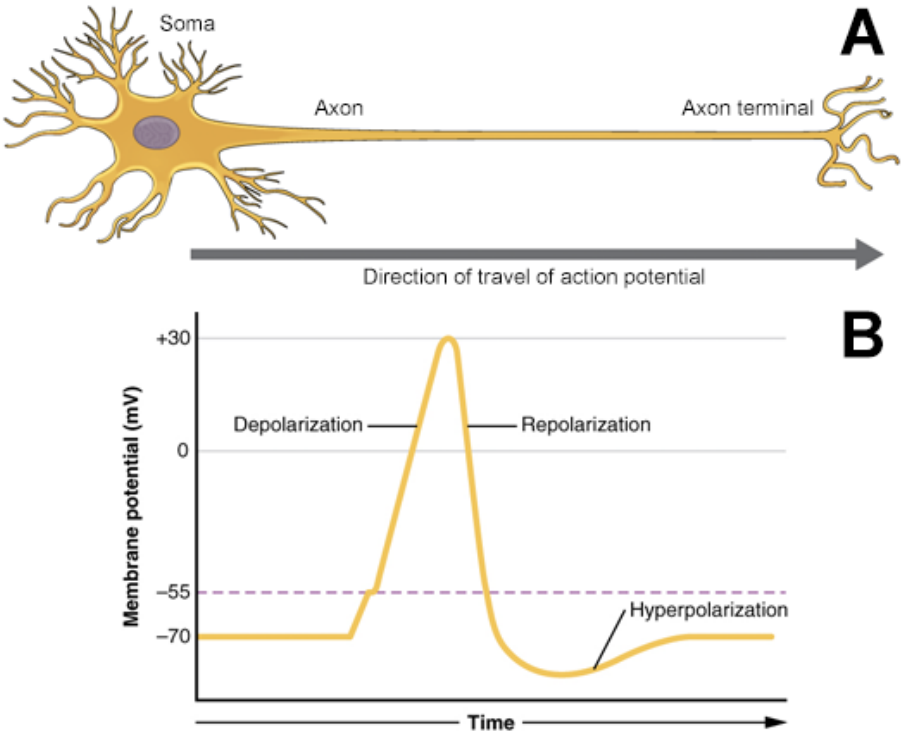

Figure 2.1: Action potential. A: Information can travel down the length of a neuron, from the axon hillock (the base of the axon, where it joins the cell body) to the tip of the axon, where it forms a synapse with the receiving neuron. B: Plotting voltage measured across the cell membrane against time. Images modified from [11].

Individual neurons are grouped into higher hierarchical units forming functional units. The types of electrical activity that can be monitored by instrumentation for diagnostic applications are typically described:

- **Single-unit**, i.e. an extracellular electrical activity at the level of individual neurons.
- **Multi-unit** spiking, i.e. a mixture of spikes from many neurons. The multi-unit activity is analyzed with a tetrode spike sorter to isolate the single units from the multi-unit recordings. [12]
- **Local Field Potentials** (LFP). LFP is an important connection between the macroscopic activity of EEG and the microscopic activity at the neuronal level [13]. Normally the LFP signal has a larger amplitude as the action potentials of the single or multi unit activity.

- **Macroscopy**. Electroencephalography (EEG) is one of the oldest and most widely used methods for the investigation of the electric activity of the brain. The scalp electroencephalogram, recorded by a single electrode, is a spatiotemporally smoothed version of the LFP, integrated over an area of 10 cm^2 or more. EEG mainly sample electrical activity that occurs in the superficial layers of the cortex [13]. Together with other neuroimaging techniques (near infrared spectroscopy, magnetic resonance imaging etc.) it serves to investigate the summation activity of a large number of neurons over various macroscopic areas of the cortex.

The brain is composed of functional areas that are allocated for perception processing including vision, language etc. A different area is responsible for each specific function [14]. Thus, the brain can be distinguished into many subregions that are directly related to a specific motor/sensory pathway (Fig. 2.2). In other words, the regions of interest. Both motor and sensory activity are manifested in premotor cortex (PM), primary somatosensory cortex (S1), primary motor cortex (M1) and supplementary motor cortex (SMA).

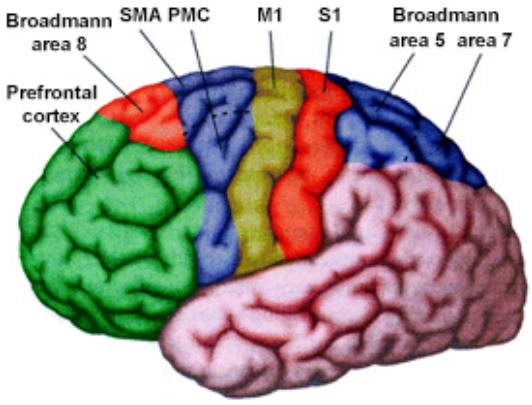

Figure 2.2: The cortical areas involved in motor control (modified from [15]).

M1 is active in the realization of the movement itself. It is mainly influenced by the cerebellum [16]. PMC, on the other hand, is triggered during motion planning or imagination and is under the strong control of the basal ganglia [16]. It is known to be used in the onset of more complex motion patterns. SMA is involved in the activation of axial muscles and proximal limb muscles, in the action of bilateral movements [16], realizing more complex movement patterns. It is also under the control of the basal ganglia. S1 receives pressure, pain, and thermal sensory information from receptors located e.g. in the skin. From a physiological point of view, the simple movement of the fingers of the left hand is reflected in the right part of the brain and vice versa (Fig. 2.3).

The control of voluntary movement depends on proper coordination of the motor and sensory system at all levels. In addition to the sensorimotor cortical areas that are necessary for planning and providing voluntary movement,

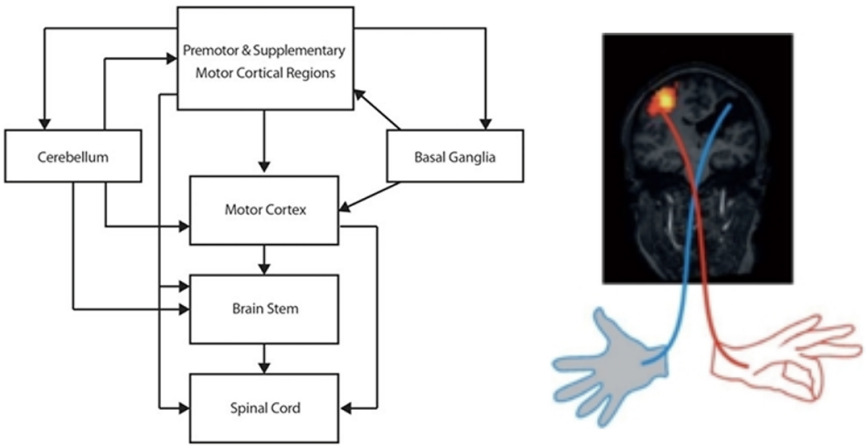

Figure 2.3: Left: A schematic depiction of the organization of the motor system. Muscles of the limbs and body are activated through neurons in the spinal cord. These receive input from nuclei in the brainstem and from various cortical areas. Activation in the motor cortex is modulated by connections with the cerebellum and the basal ganglia [15]. Right: The simple movement of the fingers of the left hand is reflected in the right part of the brain and vice versa [14].

interactions with subcortical regions involving the basal ganglia and the thalamus are also involved. These are mainly involved in managing learned automatic movements and suppressing unwanted movement patterns. This is related to specific disorders of movement management encountered in many neurological disorders.

2.2 Disorders of Basal Ganglia Function

The basal ganglia (BG) is a group of subcortical nuclei, of varied origin, in the brains of vertebrates including humans, which are situated at the base of the forebrain. It has been known since the mid-1980s that the basal ganglia (Fig. 2.4) are arranged in topographically and functionally specific circuits that also involve discrete regions of the thalamus and cortex (the „segregated circuit hypothesis“). These circuits are named after the function of the cortical areas from which they originate as motor, associative, limbic, and oculomotor circuits. With some exceptions, the different circuits are similar in their general anatomical arrangement. In terms of the basal ganglia involvement in the pathophysiology of movement disorders (also known as extrapyramidal symptoms), the motor circuit is of particular relevance. [17]

BG control excitation and inhibition of cortex, therefore requiring two distinct pathways: a direct pathway (cortex → striatum → globus pallidus internus) was assumed to facilitate motor cortical activity, while an indirect pathway (cortex → striatum → globus pallidus externus → subthalamic nucleus → globus pallidus internus) was assumed to inhibit motor-cortical

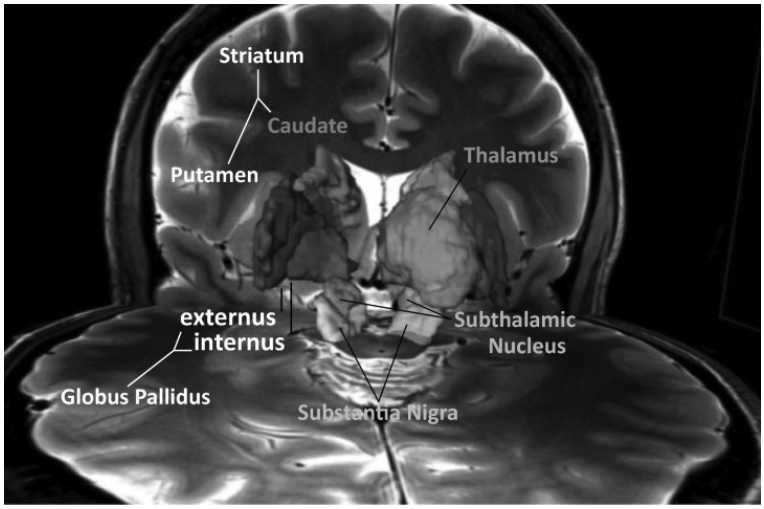

Figure 2.4: Three dimensional visualization illustrates intimate topography of the subcortical constituents of the cortico-basal ganglia-thalamo cortical network [18].

firing. By coordinated activation of both the direct and indirect pathways, movement can be „scaled“ and „focused“ appropriately [19]. These concepts provided an explanation of prominent BG motor disorders: over-activity of the excitatory direct pathway was assumed to result in overshoot of motor activity (as in Huntington's disease), while over-activity of the inhibitory indirect pathway was proposed to result in pathological motor inhibition (as in Parkinson's disease). The hyperkinetic movements in dystonia have been ascribed to excessive activity of both the direct and indirect pathways. This excess activity has been hypothesized to lead to the dis-coordinated contractions of muscle groups and the clinical phenomenon of dystonia [20]. As part of this process, an additional, shorter route of the indirect pathway (cortex → striatum → globus pallidus externus (GPe) → globus pallidus internus (GPi)) has been proposed as well as an additional hyperdirect pathway (cortex → subthalamic nucleus (STN) → globus pallidus internus). If all of these pathways can be identified to fulfill distinct functions, the complexity of BG anatomy might be understood as a necessity to guarantee BG functionality (Fig. 2.5) [21]. Selected diseases relevant to the thesis datasets are described in the following subchapters.

2.2.1 Dystonia

Dystonia is a movement disorder in which a person's muscles contract uncontrollably. The contraction causes the affected body part to twist involuntarily, resulting in repetitive movements or abnormal postures according to a relatively invariable pattern, and in many cases leads to severe invalidation of the patient [22]. Dystonia can affect one muscle, a muscle group, or the entire body. Dystonia affects about 1% of the population, and women are more

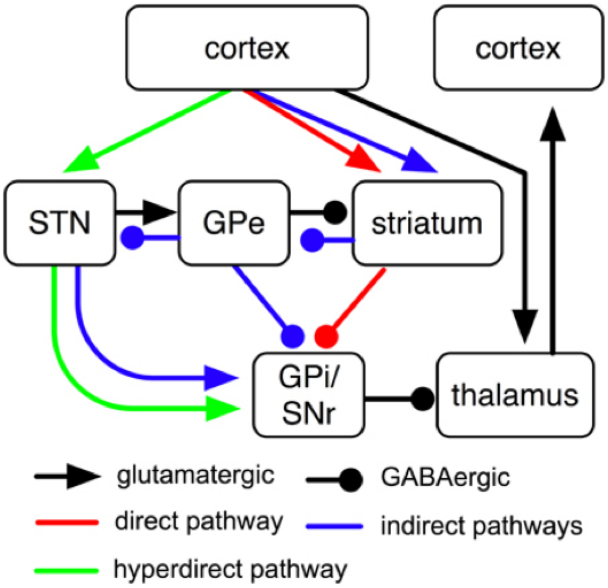

Figure 2.5: Sketch of cortico-BG-thalamic fiber tracts and their subdivision into direct, indirect and hyperdirect BG pathways. Of the "indirect pathway", two routes have been proposed, the short one of which passes from GPe directly to GPi, while the longer one additionally passes through STN [21].

prone to it than men [22]. In addition to oral treatment and local botulinum toxin treatment, severe dystonic syndromes are subjected to the deep brain stimulation therapy, which is mainly used in generalized and segmental dystonia. The age of onset is a factor in determining the phenotype of dystonia. The phenotype of childhood-onset dystonia is highly associated with the DYT1 mutation [23]. Whole exome sequencing is an efficient, sensitive and specific method for determining the genetic cause of dystonia [24].

2.2.2 Parkinson's Disease

Parkinson's disease (PD) is a commonly occurring neurodegenerative disease in 2 out of 100 people over 60 years of age. Its cause is directly related to the loss of dopamine-forming nerve cells in a part of the brain called substantia nigra, which is a part of the complex of basal ganglia [25]. Speech is an important indicator of motor functions and movement coordination, while being extremely sensitive to the central nervous system's involvement [26]. The key symptoms in PD as well as in less frequent neurodegenerative disorders (so called atypical parkinsonian syndromes (APS) are bradykinesia (delayed initiation, restricted speed and decreasing amplitude of movements), rigidity (muscle hypertonia), tremor at rest, and postural instability. APS refer to a heterogenous group of disorders, including progressive supranuclear palsy, multiple system atrophy, corticobasal degeneration and dementia with Lewy bodies that may be clinically indistinguishable from PD, especially in the early disease stages [27]. However, subtle differences in motor involvement

may help to discern between various causes of parkinsonian syndromes, since the early disease stages [28].

Timely detection and precise evaluation of motor dysfunction is thus a prerequisite for early diagnosis and prospective evaluation of neurodegenerative diseases, especially in the view of coming neuroprotective therapies. So far, clinical evaluation of movement disorders has mainly been done using semi-quantitative ordinary scales such as Unified Parkinson's Disease Rating Scale (UPDRS). However, the scores heavily depend on the examiner's experience and subjective judgment. Major movement symptoms of PD, such as tremor, stiffness, slowing, posture and gait disturbances, are only manifested when a significant portion of the brain cells are affected.

2.2.3 Deep Brain Stimulation

Major breakthroughs in the treatment of many neurological disorders have been made possible with miniature specialized electronic hardware devices that are implanted in the patient to compensate for impaired physiological functions [29]. In addition to pacemakers and cochlear implants, it is necessary to utilize electrodes used for deep brain stimulation (DBS), which is an effective alternative to the pharmacological treatment of Parkinson's disease or heterogeneous dystonia [30]. DBS is an internationally accepted form of treatment option. The process of DBS implantation is demanding in terms of time, expertise and finances. This invasive method is capable of significant symptom alleviation, which could dramatically improve the quality of life of patients with various movement disorders.

DBS is performed by an electrode that is stereotactically implanted into the target in the brain and connected to a programmable stimulator located in the subcutaneous tissue of the chest [31] (Fig. 2.6). Stimulation is provided by the application of monophasic or biphasic voltage pulses, to one or more electrode contacts. A number of pulse clinical settings can be controlled via an external programmer which communicates wirelessly with the stimulator. Hyperkinetic pathological communication in the subcortical neural networks that are responsible for motor functions is suppressed during the stimulation by a current. In particular, the inner segment of the globus pallidum (GPi) can be stimulated. GP interna et externa (GPi/GPe) and the subthalamic nucleus (STN) are the key nuclei of the basal ganglia involved in automatic motor control. Despite their small dimensions they have complex spatial organization with connections to motor and non-motor circuits. However, knowledge of particular neuronal populations in the GPe/GPi and their intrinsic connectivity is still very limited. The success of DBS depends not only on the precision of neurosurgical performance, but also on the optimal determination of the stimulation parameters in a suitable patient selection.

The main target of deep brain DBS for dystonia is the posteroventral part of the GPi. GPi-DBS is an effective treatment for pharmacoresistant dystonic syndromes, where pathophysiological mechanisms of action are not yet fully

understood [32]. In comparison to the effects seen in PD, the improvement in dystonic postures appear to differ in several ways—delay of clinical benefit, higher voltage requirements, and varied stimulator settings [33]. DBS of the subthalamic nucleus (STN-DBS) is a typical target treatment for PD patients.

Many DBS failures are, in fact, due to poor patient selection. Most of available models of illness are hybrid models; past knowledge is mishmashed with present knowledge. These hybrid models produce the illusion of a systematic understanding of a disease—but the understanding is, in fact, incomplete. Closer look at „exceptional responders“, might have some peculiar combination of factors—genes, behaviors, risk factors, environmental exposures—that had made them respond briskly and durably [34].

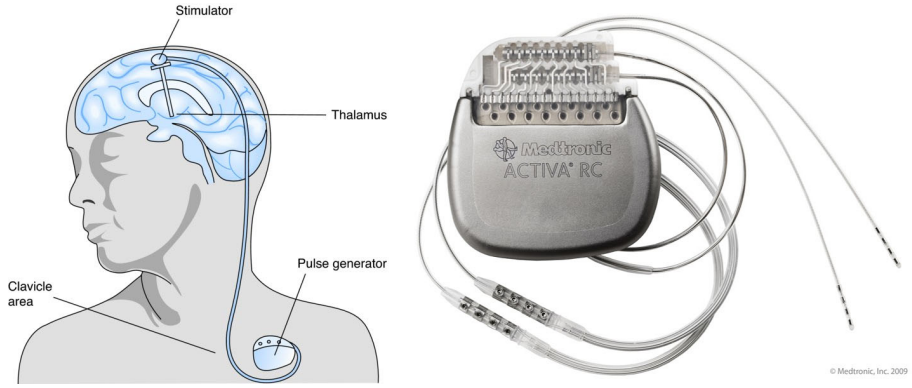

Figure 2.6: Deep Brain Stimulation (left) [35], Medtronic generator of the pulses (right) [36].

Noninvasive deep brain stimulation is an important goal in neuromodulation: a promising area of DBS in the future is the development of optogenetics. Chen et al. used specialized nanoparticles that can upconvert near-infrared light from outside the brain into the local emission of blue light. They have injected these nanoparticles into a mouse brain and activated channel expressed in dopaminergic neurons with near-infrared light generated outside the skull at a distance of several millimeters [37].

DBS is thought to regulate or control neurochemical release, but existing DBS devices depend on pre-programmed electrical stimulation amplitude and frequency in an open-loop configuration. To improve outcomes and reduce adverse effects, the goal of current research is an implantable closed-loop adaptive device that uses LFP or neurochemical feedback to drive stimulation parameters. Feedback control is based on neuronal activity from the basal ganglia (Fig. 2.7). [38, 39]

2.2.4 DBS Surgical Workflow

The various steps of performing DBS include taking a preoperative non-stereotactic magnetic resonance imaging (MRI), stereotactic frame fixation,

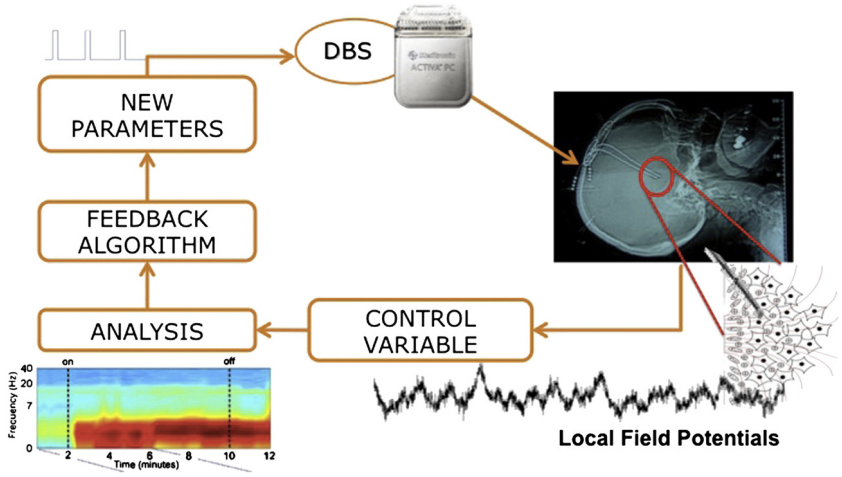

Figure 2.7: The concept of adaptive closed-loop deep brain stimulation [39].

fusion of MRI with stereotactic computed tomography (CT) scan images, planning of the target and trajectory, DBS lead placement at target through the planned trajectory, implantation of pulse generator/battery and programming of the implanted device. Utmost care and precision are required to execute the procedure, which decide the final outcome of the surgical procedure. DBS lead implantation are preferably done under local anaesthesia. This facilitates the intraoperative clinical evaluation of patients for obtaining the optimal response and for avoiding any procedural side effects. [40]

As described by Singh et al., the standard surgical treatment workflow can be divided into the following important phases [40]:

a) Preoperative non-stereotactic MRI.

   The field of view must encompass the entire region of interest including the anterior commissure/posterior commissure (AC/PC) structures and the target region.

b) Stereotactic frame fixation.

   The principle of using any stereotactic frame is to create a stereotactic space around the patient's head in order to deduce coordinates (based on the Cartesian system), which in turn are used during surgery to reach any target inside the cranium.

c) Stereotactic CT scan.

   Once the patient's head is aligned well with the frame system, a CT scan is acquired.

d) Planning.

   The stereotactic CT images are fused with the non-stereotactic MRI images on a split screen, and it is ensured that each sulcus and other intracranial landmarks on both the images are overlapping perfectly. The

usual X, Y, and Z coordinates of the subthalamic nucleus and globus pallidus internus are as follows:

- STN: 10 to 12 mm lateral and 2 mm posterior from the mid-commissural point and 4 mm ventral to the AC/PC line,
- GPi: 19 to 22 mm lateral and 2 mm anterior from the mid-commissural point and 4 mm ventral to the AC/PC line.

e) Lead implantation.

As the electrodes move deeper towards the target, microelectrode recording (MER) is continuously done to look for the target. Once the target is localised precisely with the help of MER recording, each electrode position is stimulated to look for the best motor response in the form of reduction of rigidity, ease of performing the motor activity and, for instance mainly in PD, the clarity of speech. Any side effect in the form of dystonia, hemiparesis, visual symptoms or dyskinesia are also noted. The final DBS lead target is decided based on the MER recording and the stimulation response.

f) The internal pulse generator (and its battery) placement.

This part of the surgery involves creation of an infraclavicular subcutaneous pouch for generator placement and tunneling for the extension wires. This procedure needs general anesthesia.

g) Programming.

The programming is usually done after 2-3 days to allow for subsidence of microlesioning effect of the electrodes at the target site.

2.3 Instrumental Biomarkers of the DBS Treatment

Several relevant substudies with the following findings have already been carried out at the Department of Neurology, 1st Faculty of Medicine. The first functional MRI study was conducted in patients with dystonia treated with pallidal DBS. In the study, 21 patients with dystonia of different aetiology were examined. Patients were examined by the fMRI resting-state method, during which 10-minutes BOLD (Blood Oxygen Level Dependent [41]) sequences were presented and monitoring the cross symbol in the middle of the screen was required.

The analysis of resting fluctuations of the BOLD signal was performed by a centrality degree mapping method (DC), where each brain voxel is mapped without a previous hypothesis in terms of functional connectivity with other brain voxels except artefact regions. It was found that in the ON state, compared to the OFF state, there was a significant increase in DC

in the thalamus bilaterally, in the right ncl. accumbens and subthalamus. Also the upper and the rear of the brain stem and the left hemisphere of the cerebellum were increased (Fig. 2.8).

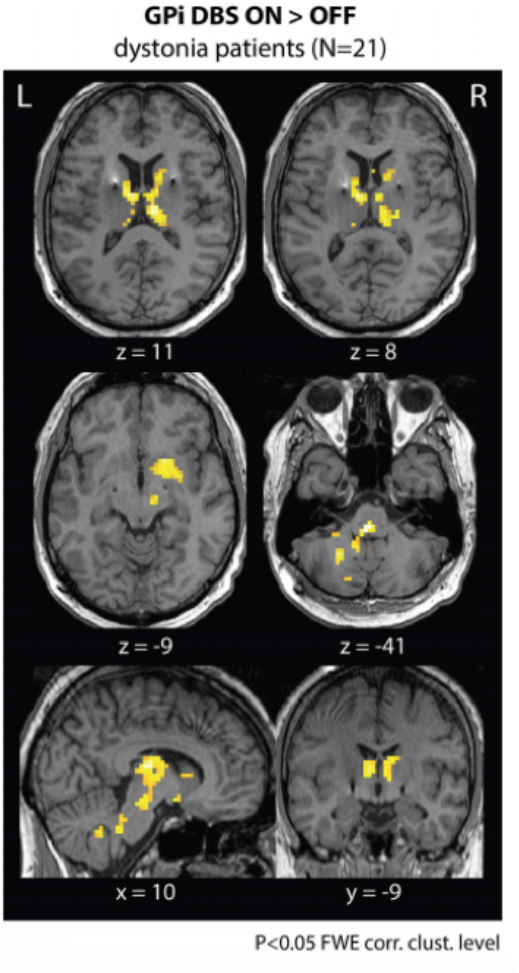

Figure 2.8: DCs of the resting-state fMRI: patients with dystonia ON vs. OFF DBS GPi [42]; DC = centrality degree mapping method.

Furthermore, a quantitative relationship between the degree of functional connectivity of the brain and the degree of clinical improvement was demonstrated. The change in functional connectivity expressed by the DC in each voxel was positively correlated with clinical improvement in the ventromedial prefrontal cortex, thalamus, middle and posterior cingulate, and also in the cerebellum. Patients who had a better long-term clinical benefit therefore had a more pronounced impact of DBS-GPi in the form of a higher increase in functional connectivity in a number of subcortical and cortical areas than patients who improved partially or did not improved (Fig. 2.9).

In order to find a correlation between the placement of the GPi electrode stimulation contact and the clinical effect of the GPi DBS, a cross-sectional study was conducted in which 23 patients with drug-resistant dystonia and a

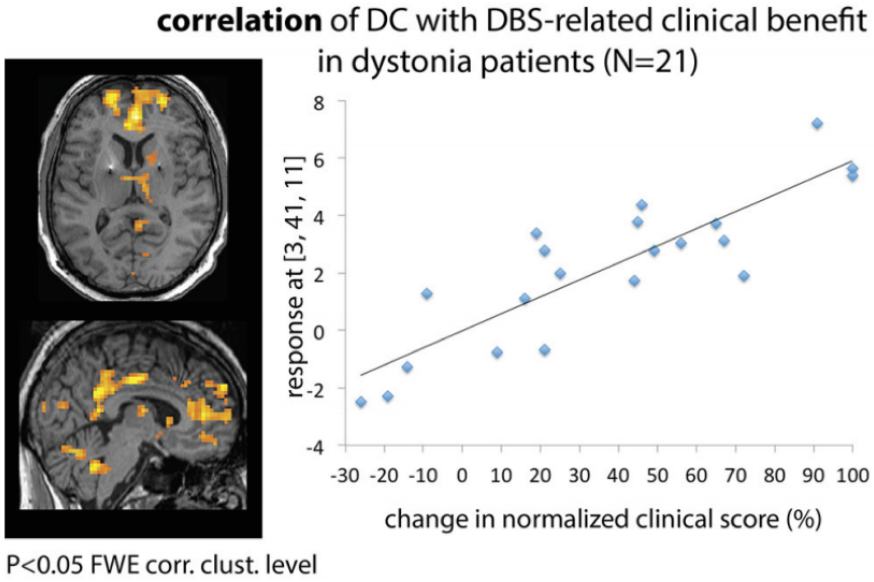

Figure 2.9: The correlation between the increase in functional connectivity (expressed by DC) and the improvement of the adjusted clinical score (postoperative clinical score when DBS GPi is switched ON compared to the preoperative clinical score) [42].

variety of aetiology were examined. All patients were treated by the long-term bilateral DBS with electrodes implanted in the posteroventro-lateral portion of GPi. The adjusted clinical effect (AKE) was expressed as a change in the dystonic score (Burke-Fahn-Marsden Dystonia - BFMDS scale in generalized dystonia, and the Toronto Western Spasmodic Torticollis Scale - TWSTRS scale in cervical dystonia) between the current postoperative state during the pallidal DBS vs. preoperative status.

Based on the correlation analysis, the x-coordinate of the electrode contact (left or right, depending on the fact which one was placed more medial) positively correlated with the antidystonic effect expressed by the AKE (rho = 0.73, $p < 0.01$) (Fig. 2.10).

It can be assumed that patients who have one of the electrodes placed too medially will benefit little or insufficiently. The position of the x-axis active contact should be the main predictor of the future success of the DBS GPi.

These phenomena were significant in spite of the large phenotypic and genotypic heterogeneity of dystonic syndromes, suggesting a common pathophysiological mechanism that DBS GPi induces. The predictor of success is only the localization of the more medial (left or right) electrode in the GPi. Functional connectivity is only a predictor of effect because its validity must be verified in prospective longitudinal studies. Findings are, however, undoubtedly significant as they will lead to a modification of the neurosurgical procedure, to improve the clinical effects of pallidal stimulation and possibly also to increase the proportion of responders.

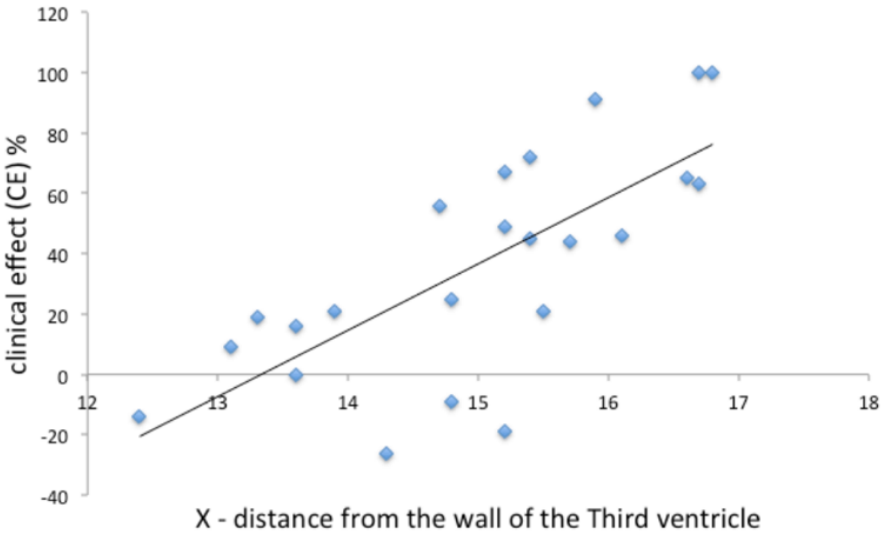

Figure 2.10: The correlation of the change in the adjusted clinical effect of the pallidal DBS and the distal contact distance of the medial electrode from the III. chamber wall [42].

Although GPi-DBS is an effective treatment for dystonia, it may cause important stimulation-induced side-effects such as hypokinetic dysarthria or stuttering (Fig. 2.11) [43]. Rusz et al. systematically evaluated speech in 19 dystonic patients with GPi-DBS. They revealed a significant increase of dysfluent words in the GPi-DBS ON when compared to OFF condition associated with the shorter distance of the active contact localization along the medio-lateral direction.

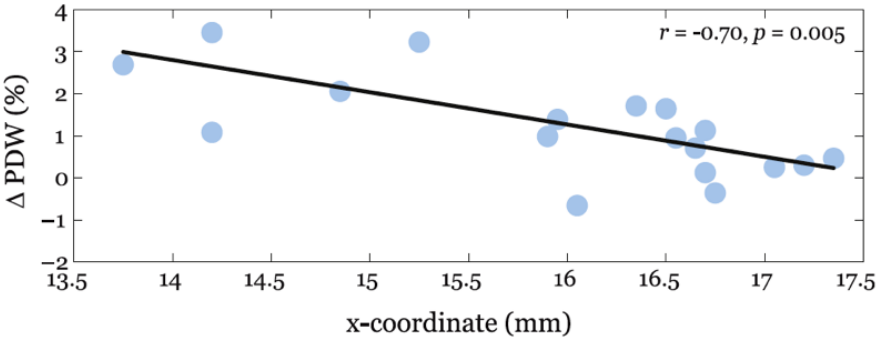

Figure 2.11: Correlation analysis between change in dysfluency level between GPi-DBS ON and GPi-DBS OFF condition (delta(PDW)) and the distance of the distal contact of the electrode from the wall of the third ventricle in the medio-lateral direction. The highest deterioration of fluency with the GPi DBS switched ON was found in patients with the active contacts placed more medially [43]. Captions: delta(PDW) percentage of dysfluent words.

2.4 Measuring of Single Unit Neuronal Activity

There are two basic types of microelectrode recordings: intracellular and extracellular. Intracellular recordings form a group of techniques used to measure with precision the voltage across, or electrical currents passing through, neuronal or other cellular membranes by inserting an electrode inside the neuron [44]. Intracellular electrodes are made of thin glass pipettes that are pulled to a very fine and sharp ending or tip. The typical time course of the intracellular action potential with its first positive peak can be modelled by the Hodgkin-Huxley theory [45] .

On the other hand, neuronal cell activity gives rise to transmembrane currents that can be measured in the extracellular medium. Although a major contributor of the extracellular signal is the synaptic transmembrane current, other sources—including Na+ and Ca2+ spikes, ionic fluxes, ligand-gated channels and intrinsic membrane oscillations—can substantially shape the extracellular field. Electric fields can be monitored by extracellularly placed electrodes with submillisecond time resolution and can be used to interpret many facets of neuronal communication [13]. The shape of the extracellular action potential depends on the location of the electrodes and the experimental conditions. This phenomenon was illustrated on the recorded spikes from a 5-layer pyramidal cell with thin saline layer covering chip (Fig. 2.12) [46].

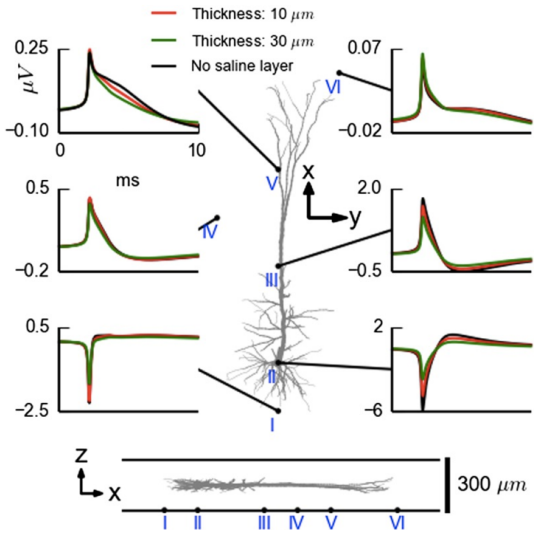

Figure 2.12: Illustration of effect of thin saline layer covering chip on recorded neural spike. Extracellular spike from a model layer-5 pyramidal cell, reprinted from [46], with quoting.

Recent advances in the development and application of nanoelectrodes enables simultaneous recording of intracellular and extracellular spontaneous spikes in mammalian neurons and cardiac cells [47]. A simultaneously recorded intracellular voltage gave the precise spike times of a local neuron, that can be used as the gold standard against which to compare the output of the

extracellular spike detectors [48].

Extracellular microelectrode recording is a basic technique for acquiring extracellular electric activity at the level of individual neurons (single-unit activity). Extracellular neuronal activity is routinely explored in patients, using monopolar and multipolar microelectrodes in several parallel trajectories, during the implantation procedure into the basal ganglia with the aim of finding an optimal site for the placement of a permanent stimulation electrode. Multi-unit recordings collected from multiple neurons are then called local field potentials. Presently, placement suitability is judged primarily by the neurologist, either visually or acoustically, based on a specific expression of neuronal action potentials (spikes). Due to their nature as all-or-none events, the occurrence of spikes over time is represented as a list of binary numbers (spike train), specifically zeroes for "no spike" or ones for a "spike". Neurons use spikes as their preferred medium of neural coding communication. Because the physiological spike duration amounts to approx. 1.5 ms, the signal should be sampled at units of kHz. The advent of high-density extracellular microelectrode arrays (MEAs) now allows recording from hundreds to thousands of channels that poses significant challenges.

2.4.1 Analysis of Extracellular Neural Activity

The reliable electrophysiological technique to determine accurate DBS electrode placement is with intraoperative extracellular microrecording (microEEG; MER) exploration. Despite advances in MRI technology and a better understanding of the relationship between an MRI and MER, MER evaluation remains the most widely used localization technique [49], [50]. The MER provides a high temporal resolution ($<$ 1ms) of the brain's neural activity in the close vicinity to the microelectrode [51].

Electrophysiological microrecordings are typically filtered in 500-5000 Hz. Bandpass filtering ensures the removal of slow shift and high frequency content while leaving the intermediate band (spiking) of frequencies intact. Spike sorting is considered the most important advanced processing step to accurately evaluate unit activity. Short-term microrecording-monitoring may be corrupted by a whole range of artifacts, which can disturb the visual and automatic signal evaluation. The modern methods of machine learning can help to detect and eliminate the artifacts from the MER.

Recent technical and machine learning advances in microrecording have created new opportunities to study biomarkers related to the various movement disorders, for instance, discovering electrophysiological "sweet spot" for DBS-STN in the PD [52]. Many studies of investigating of the neural activity have been performed in GPi as well as in STN. Such studies aim to describe the functionality of specific neurons, which is of paramount importance in neuromodulation research with possible therapeutic applications in medicine.

The behavior of basal ganglia nuclei generally differs, depending on the type and diagnosis. For example, GPi neuron discharges are faster than

GPe neurons [53]. Differences in GPi/GPe neuronal firing rates and patterns relating to different disease biology in children with dystonia were investigated in [54]. Moreover, neuronal firing rates and patterns in the GPi of patients with cervical dystonia differed from those with PD. The mean GPi neuronal firing rate recorded from dystonia was lower than that in PD. Furthermore, GPi neurons fired in a more irregular pattern compared with PD [55].

From the biomarkers point of view, it was observed that DBS-STN enhanced beta-band activity recorded in patients suffering from PD, correlated with disease severity [52, 56]. Neumann et al. [57] analysed recordings relating to dystonic symptom severity which significantly correlated with GPi theta oscillatory amplitudes.

2.4.2 Spike Detection and Sorting

Data analysis for neuron recordings still requires two main problems to be solved—the reliable detection of spikes and the sorting of these spikes by their originating neurons. Finding the number of neurons is usually done manually during spike sorting—it is an unsupervised clustering problem where the number of the clusters is unknown. Approaches and solutions for both problems are difficult to evaluate quantitatively, due to a lack of knowledge about the truth behind the experimental data [58].

Spike sorting is one of the key techniques to understand brain activity. The process pipeline starts with a simple/adaptive threshold detection and ends with unsupervised sorting according to multidimensional feature extraction [59, 60] (Fig. 2.13). Machine learning techniques including deep learning, clustering, fuzzy, the Bayes approach and many more are successfully applied during spike sorting [61, 62].

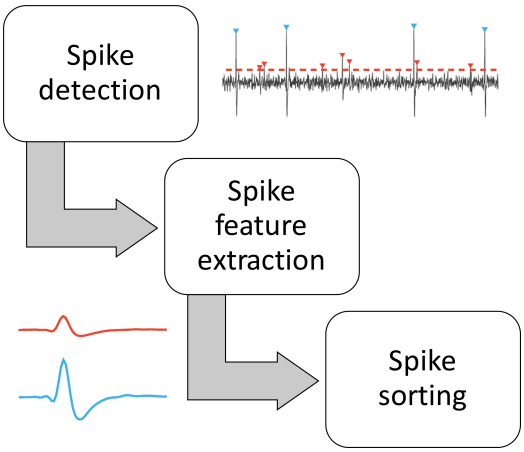

Figure 2.13: Three principal stages of unsupervised spike sorting algorithms.

Amplitude thresholding methods are the simplest: A spike is detected if the band pass filtered raw signals crosses a predefined threshold such as a

multiple of the standard deviation of the underlying signal. A threshold that is frequently used is [63]:

$$Thr = n\sigma_n, \sigma_n = median\left\{\frac{|x|}{0.6745}\right\}, \tag{2.1}$$

where n is a constant (typically $n = 4$) and the second term is an estimate of the standard deviation of the noise in the voltage x. Signal to Noise Ratio (SNR) is an important parameter that affects spike detection. The distance is often given in dB, when the ratio is converted to ten times the decimal logarithm from the SNR.

Usually, spike sorting analyzes are performed manually or with some semi-automatic tools, so it is a laborious and time-consuming task. Its objective automation is complicated. The purpose of various algorithms is to reduce the complexity and increase the accuracy of the entire process. Close neurons are first detected using an amplitude threshold. Peaks exceeding the threshold form a set of candidate spikes, which can then be clustered based on their amplitude and shape [60].

WaveClus algorithm by Quiroga has become a research milestone for the convenience and accuracy of sorting. Detected spikes can be described by many features: e.g. amplitudes, gradients in curves, WaveClus features, wavelets coefficients [64]. The best wavelet coefficients can be selected as those with the least Gaussian distribution, using a Kolmogorov-Smirnov test of normality.

The reduction of dimensionality, including the Principal Component Analysis (PCA) or Independent Component Analysis (ICA) [65], is a task employed prior to clustering. In a recent article, Dimitriadis et al., introduced the stochastic neighboring embedding (t-sne) dimensionality reduction method as a visualization tool in the spike sorting process. T-sne embeds the n-dimensional extracellular spikes (n = number of features by which each spike is decomposed) into a low (usually 2D/3D) dimensional space. They show that such embeddings, even starting from different feature spaces, form obvious clusters of spikes that can easily be visualized and delineated with a high degree of precision [66].

An effective clustering algorithm relating to the WaveClus is superparamagnetic clustering. For instance, selected wavelet coefficients serve as the input for the unsupervised classification expectation maximization algorithm [67]. However, the use of various unsupervised approaches is available: K-means, Gaussian Mixture Models, DBSCAN etc. Links and comprehensive descriptions of publicly available code for spike sorting can be found in [68]. Examples of software packages and their mode of operation that have been used for human recordings are as follows:

- MClust — manual [69],

- KlustaKwik — semi-automatic with manual refinement [70],
- OSort — automatic online sorting, manual cluster selection [71],
- WaveClus — automatic offline sorting, manual cluster selection [72].

2.4.3 Spike Train Analysis

Mathematically, spike train analysis is essentially an analysis of event-to-event data. Typically, the first step in spike data analysis involves visualizing and using simple descriptive statistics to characterize pertinent features of the data [73]. Various spike train metrics have been proposed to decode information content from biological spike trains [74]. Multineuron spike trains are called "parallel spike trains". In the case of a single spike train, the main idea is to convert a spike train into a set of features that can be visualized and/or compared across different conditions, for instance:

- mean firing rate (MFR),
- instantaneous firing rate,
- variability,
- Fano factor,
- power spectra (and power in specific bands),
- inter-spikes interval (ISI),
- ISI histogram,
- coefficient of variation (CV) of ISI,
- autocorrelation,
- entropy,
- burst-based metrics: burst rate, number of spikes in a burst, inter-burst intervals, burst index,
- serial correlation,
- generalized linear model.

As a summarizing example of spike train analysis, spikes were extracted from a prototypical brain measurement with spontaneous spiking activity and then clustered using WaveClus [72] (Fig. 2.14). The recording time was 5 min at a sampling rate of 20 kHz.

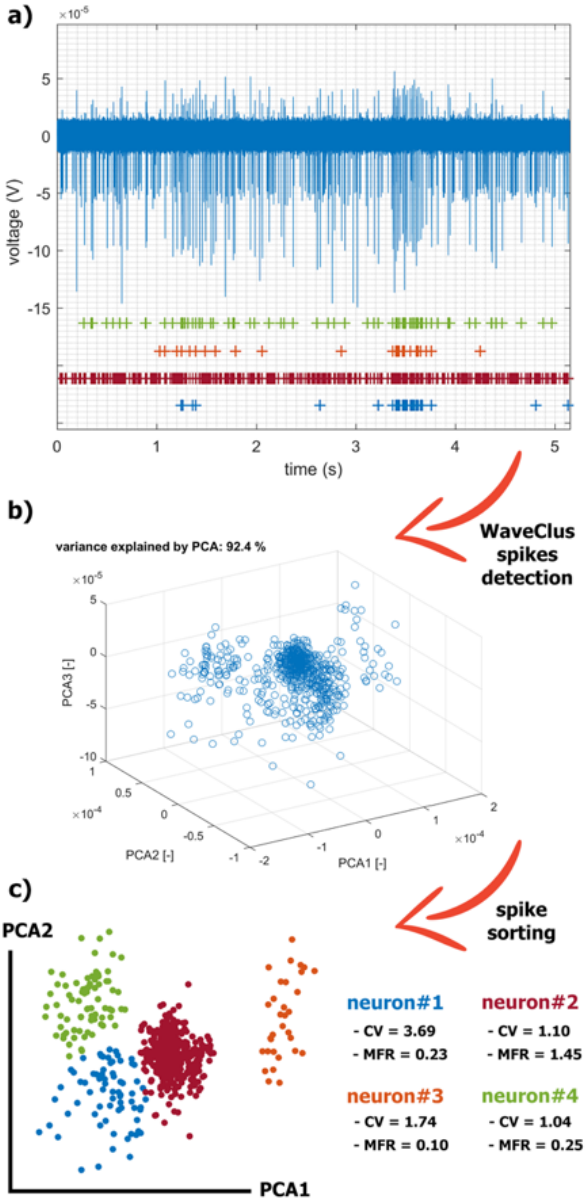

Figure 2.14: The application of the selected methods for real MER processing. The recorded series is a summary activity of a large number of neurons further away from the electrode (background activity) and the activity of neurons in close vicinity of the electrode tip (single-unit activity). The signal can be decomposed in an estimation process called spike-sorting: a) A filtered raw signal and visualization of individual spike trains hidden in it. b) We used PCA to reduce multidimensional space after WaveClus detection. c) The spikes were sorted by the 4-means method and characteristic statistics on extracted neurons are listed.

2.5 Measuring of Cortical Neuronal Activity

Current technical capabilities to investigate functional imaging at the macroscopic level rely mostly on functional magnetic resonance imaging (fMRI) or positron emission tomography (PET) studies. Using these advanced imaging systems, novel macroscopic insights of both cortical and subcortical pathways are mapped. However, such studies are not feasible during gait.

Functional Near-Infrared-Spectroscopy (fNIRS) equipment has become commercially available and widely used in clinical practice such as diagnosis in psychiatry, neurosurgery or pediatrics [75]. The continuous-wave near-infrared spectroscopy has made it possible to measure hemodynamic change in the living tissue, or more precisely the product of change in hemoglobin concentration in living tissue and the mean optical pathlength. This equipment helps physicians obtain physiologically useful information in the human body with a noninvasive approach, e.g. monitoring oxygen metabolism in the muscles [76]. NIRS is also a portable neuroimaging method that uses low-energy optical radiation to measure extinction properties in subsurface tissue caused by concentration changes of hemoglobin which correlates with cortical activity (Fig. 2.15) [77].

Red and near-infrared light in the wavelength range from 650 nm to 900 nm propagates more deeply into living tissue than visible light of wavelengths shorter than 650 nm, thus hemodynamics in the living body can be non-invasively monitored by using light of this wavelength range where the absorption characteristics of oxyHb and deoxyHb in the blood are different [78].

The NIRS method is based on measuring the extinction of hemoglobin for two wavelengths: oxyhemoglobin (HbO, oxyHb) and deoxyHb using optoelectrodes, which are placed into the grid as EEG electrodes [79]. The hemodynamic response (HR) is similar to the fMRI [80]. The HR starts with a latency of 1-2 seconds after the beginning of the event and reaches a maximum after 7 seconds. A frequency band associated with the event corresponds approximately to the range of the HR recorded using a blood-oxygen-level-dependent (BOLD) fMRI in the range of 0.01 Hz to 0.1 Hz [81]. Like fMRI, it is based on the theory of the BOLD effect. Motor activity in a fMRI is typically around the frequency of 0.04 Hz, which agrees with the measured frequency of the NIRS signal during a simple motor task (dominance at 0.035 Hz). In comparison to a fMRI, NIRS provides lower spatial resolution, but has a better time resolution. A high-density NIRS device could significantly improve even the spatial resolution and eventually can be easily integrated with nearly any EEG electrode for concurrent NIRS/EEG measurements. It has been shown that there is a significant correlation in a time series NIRS and fMRI [82]. The depth of penetration in the head of an adult is in the range of 15-25 mm. The NIRS system is safe, versatile, portable and can measure from anywhere on the head.

An important clinical opportunity is the possibility to examine NIRS under a set of interesting DBS conditions, which is sometimes a problematic criterion

when deciding on enrollment of patients into fMRI studies. However, there are already medical reports of DBS studies performed under magnetic field (prof. Jech; co-supervisor of this thesis).

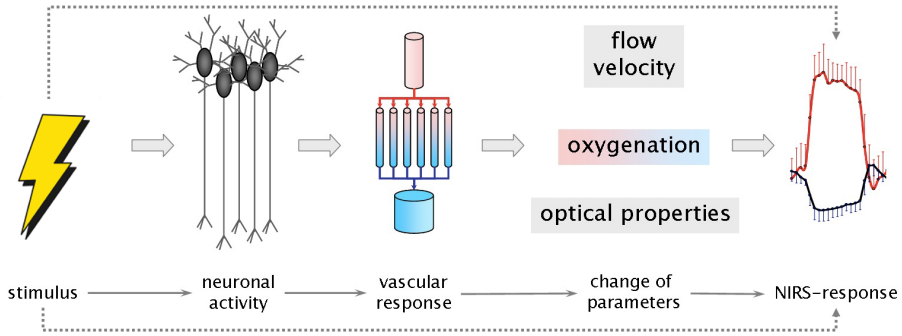

Figure 2.15: Neuronal activity leads to changes in the tissue's biophotonics, modified from [83].

In this chapter, I have presented a summary of the relevant medical and technical topics which will be needed to understand the rest of this thesis, i.e. methodological and clinical results.

Chapter 3

Aims of the Thesis

This thesis tries to investigate several aspects of the brain recordings associated with the deep brain stimulation therapy applied to the human basal ganglia. As found in the State-of-the-art, the analysis of extracellular recordings is a computationally and conceptually complex task with multiple sources of error and bias that can affect subsequent data interpretation. Additionally, current analysis workflows lack standardisation. Moreover, the currently used semi-quantitative clinical scales lack the sensitivity and specificity to accurately evaluate patients suffering from extrapyramidal disorders. More objective methods of neurological assessment are wanted in both clinical practice and research. Most likely new imaging modalities, sensors, data acquisition and analysis methods are needed to better reverse engineer the disease mechanism.

The goal of this thesis is to introduce such methods and apply them to the evaluation of patients suffering from PD and dystonia.

Overall thesis aim. **To define, implement, and validate computational algorithms for a complex evaluation of the neuronal recordings in the field of neuromodulation.**

- To specify software requirements, develop software for automatic spike detection and sorting and test the tools on the large set of real neuronal spiking data (Chapter 4 and 5, Appendix A).
- To define and develop a comprehensive pipeline for processing and computation of the descriptive parameters from the neuronal microrecordings.
- To find clinically relevant microrecording parameters in patients with DBS-GPi (Chapter 7).
- To evaluate the near-infrared spectroscopy neuronal recordings in patients with microelectrode recording-guided targeting of the STN (Chapter 8).
- For each computational approach, introduce clinical procedures, data and subjects enrolled.

Aim. **a) Analysis of artifacts and their removal from the microrecordings (Chapter 6).**

- To define computational tools to automatically evaluate the classes and time scale properties of microrecordings artifacts.
- Application, comparison and selection of optimal features for artificial neural networks for detection, classification and visualisation of microelectrode recordings elements.

Aim. **b) Based on the proposed pipeline, identify parameters that can predict dystonia patients responding to the DBS (Chapter 7).**

- Usage of multivariate statistical and machine learning methods for automatic features selection.
- To find potential metrics allowing to distinguish between responders vs. non-responder.

Aim. **c) Carry out complex analysis of near-infrared spectroscopy recordings and compare with different modalities and clinical examination (Chapter 8).**

- To analyze changes in motor activation patterns in PD patients, in relation to DBS based upon guidance with microelectrode recordings.
- To detect functional changes in the motor cortex activation patterns using NIRS.
- NIRS brain mapping algorithm implementation and testing.
- To reveal the activation patterns in the somatosensory, motor, supplementary motor and premotor cortex in relation to the performance of upper limb motor tasks.
- Correlations of movement analysis and NIRS results with clinical examination scores.

Part II

Methodological Results

Chapter 4

Pipelines for Spike Detection and Sorting

New developments in single-cell (SC) technologies have become important analytical tools, that allow detailed assessment of the fundamental biological units—the cells and its subpopulations. Looking at cells on an individual level is technically feasible in many different ways that can be integrated together to increase the depth of data description [84]. The most recent genomics methods for studying SC are used to diagnose neurological [85] or autoimmune diseases [86], e.g. to determine RNA gene expression of different tissues, including the brain [87] or to reveal dynamics of rare adult newborn neurons [88]. Other subareas of single cell analysis then focus on morphology (neuromorpho.org), even the functional properties, projected by the electrophysiology of excitable tissues in terms of spatio-temporal spiking [89]. Typical tasks in processing SC data of different types are identification of individual (sub)populations and their sorting.

Normally, needle electrodes would be used to monitor the electrical activity of a neuron, but it is less demanding and less invasive to apply an electrode array and measure the potentials between individual electrodes. However, nature of the signal is the same as for MERs. In this chapter I will define a methodology and two algorithms for neuron recognition based on unsupervised learning.

4.1 Introduction

Microelectrode arrays (MEA) biosensors are extensively used for recording and stimulating neural activity in vitro and in vivo. They serve as a valuable tool for neurotoxicology screening of various neuroactive compounds and in pharmacological studies [90–93]. MEA technology can be applied to any electrogenic tissue (i.e. central and peripheral neurons, heart cells, and muscle cells).

The MEA/MER signal processing procedure requires finding and distinguishing individual neuron spikes in the recordings as well as in any other MER signal. The specific number of visible neurons around the microelectrode

is from a practical point of view only putative, estimated based on action potential characteristics (accurate positioning and neural growth measuring is possible via optical methods). Valuable information can be obtained by clustering spikes according their features. Spike sorting follows a sequence of several steps which enables the extraction of action potentials (spikes) from raw data, ideally divided into groups (clusters) according to their neuron of origin (see Fig. 4.1) [61, 94]. For example, Rossant et al. reported a novel complex approach, especially suitable for large dense MEA, for detecting overlapping spikes in more than one electrode [95]. However, spike identification is usually done manually which is inaccurate and inappropriate for complex datasets.

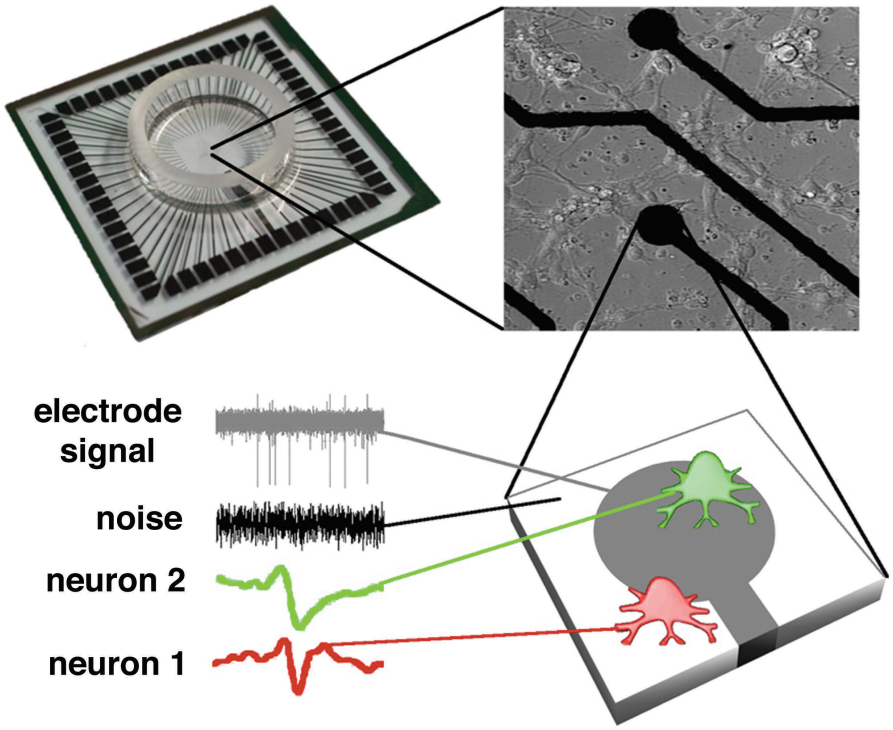

Figure 4.1: MEA signals contain spikes generated by different neurons [61].

The processing of extracellular signals is a computationally and conceptually complex task with multiple sources of errors, which can affect downstream data interpretation. It is challenging to solve the problem of automatic detection of action potentials satisfactorily for the following reasons:

- Spike shapes and background noise are different for a neuron.
- Attenuated action potentials from distant neurons can also penetrate into the recorded signal, it is difficult to clearly determine what we consider to be a relevant spike and what is noise. Indeed, often even two experts disagree on the makeup of a single recording.
- Signal to noise ratio may be very low in some signals [96].

4.2 Data Acquisition and Storing

Forty-five randomly selected extracellular signals from 26 unique measurements of an embryonic hippocampal rat neurons (daily recording, 6 min) were recorded on a commercial 60 titanium nitride (TiN) channels MEA (USB-ME64-System by Multi Channel Systems MCS GmbH). The electrodes are aligned in an 8 x 8 grid. Measured data was recorded using MC_Rack in a compressed .mcd format. One file contains 60 records from individual measuring electrodes. Raw signals in the MEA .mcd file format is loaded or converted (to csv or plain text) by developed batches of MATLAB scripts. All data files are stored on a shared e-infrastructure repository. One file takes about 700 MB of memory.

Typically, signal sources are within a radius of 30 μm around the electrode center. The peak amplitude values of spikes are in the range of tens to hundreds of microvolts. The total duration of one spike is about 1.6 ms, which corresponds to the dominant frequency of 625 Hz. Data was recorded at a sampling frequency of 20 kHz.

However, since the signal is recorded extracellularly, directly from a cultivation medium, there is a significant amount of background noise, arising from three main sources: biological noise (mainly other cells in the electrode vicinity), electrode-electrolyte noise (liquid-metal interface) and device noise (especially the amplifier) [97].

4.3 Neurons Recognition and Sorting Procedures

Signals were band-pass filtered (Butterworth 2nd) in the 300–3000 Hz band (BPF). Since the detection tradeoff is related to the signal to noise ratio of the recording, an amplitude detector was used for spike detection. The value of the threshold (automatic or adaptive) is typically given by a multiplication of the standard deviation of the signal noise by a factor from 3–5 [98]. The number of samples corresponding to the minimum refractory period was considered as 36 (i.e. 1.8 ms). The threshold for extracellular detection was automatically set to 4 [64].

Each detected spike was modulated by a cubic spline curve and 64 equidistant shape-based features were computed with the WaveClus MATLAB toolbox [72]. The three largest Principle Component Analysis (PCA) components from total, previously computed, 64 shape-based features were extracted for every spike and mainly 2D PCA were used in successive steps. Unsupervised cluster analyses K-means + gap criterion (alg. 1) and the Gaussian Mixture Model (GMM) + Bayesian Information Criterion (BIC) (alg. 2) for an automatic estimation of the number of clusters in reduced 2D PCA spikes data were investigated (Fig. 4.2) and statistically compared. All three principal components served solely for exploratory data analysis in a 3D space and detailed expertise rating.

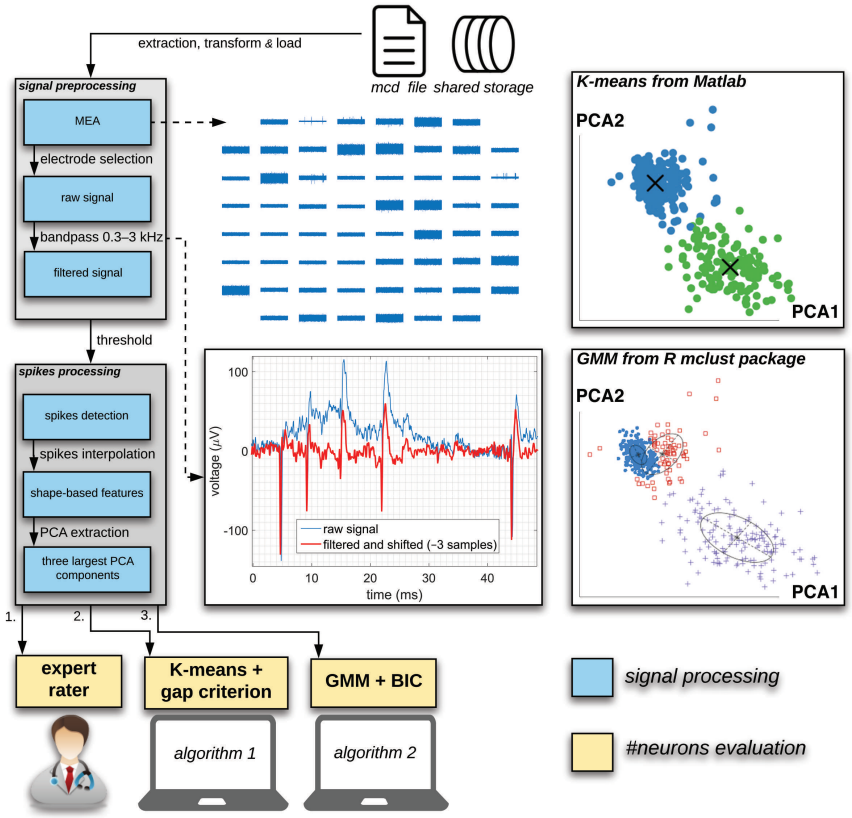

Figure 4.2: The methodology of the designed spike sorting processing experiment. The pipeline schematically lists all the steps for working with the MEA signals. The bandpass filter is used to remove the slow shift, which can significantly influence spike detection. The graphs on the right side indicate that the GMM estimated different numbers of neurons compared to the K-means on the same example 2D PCA data.

In the case of the proposed alg. 1, we used the K-means algorithm with Euclidean distance from MATLAB, in combination with gap criterion (GC), which is not restricted to a certain type of metric distances. The GC is defined even for clustering solutions that contain only one cluster. The GC utilizes estimating the most dramatic decrease in error measurement during several proposed numbers of clusters with the largest gap value. The formula and implementation details can be found in [99].

Neuron recognition with the proposed alg. 2 was performed in R Shiny's NeuroEDA web application for BioData assesment (Appendix A). The mclust R package provides models and methods to estimate the number of clusters in the multivariate dataset. The algorithm uses 10 models to calculate the default from 1 to 10 GMM components (clusters) and choose the minimal value of BIC to select the final number of clusters. BIC uses the optimal loglikelihood function value and penalizes for more complex models, i.e., models with additional parameters. The penalty of BIC is a function of the

sample size:

$$BIC = -2log(L) + numParam * log(numObs).$$

As the real number of neurons in the vicinity of each microelectrode is not known during data analysis, we can only consider the similarity among the scores. The optimal number of clusters (neurons) were then further evaluated by an expert rater. Inter-rater reliability analysis of the detected neuron numbers was conducted. Additionally, F-test and confidence interval were computed. Statistical analyses were performed using R Statistical Software and irr library. P-values of 0.05 or lower were considered statistically significant.

4.4 Results

The results are shown in Table 4.1. The total Intra Class Correlation (ICC) showed a significant inter-rater agreement for all 3 rater procedures (ICC = 0.69, $p < 0.001$), when post-hoc weighted Cohen's Kappas for 2 raters were ICC = 0.85 (expert vs. alg. 1; $p < 0.001$; relative agreement = 0.71) and ICC = 0.62 (expert vs. alg. 2; $p < 0.001$; relative agreement = 0.60). The largest 3 PCA components could explain the 80.2 % ($\pm$13.6 (std)) variability of unreduced data.

A final fully automated procedure for MEA recordings based on alg. 1 has been proposed and developed using the three largest PCA components (Fig. 4.3) for offline processing in MATLAB R2015a (Mathworks, USA).

4.5 Discussion of the Proposed Method

Evaluation of the recorded data remains a major challenge due to the large amount of generated data and the presence of complex patterns in the behavior of neural cells. Neuroscientists have argued that a generally functioning spike sorting approach is not yet feasible, but the design of this study may be the next step towards this goal.

There were many general observations. Alg. 2 often estimated more neurons in 2D PCA space than both the expert rater and alg. 1, preferring Gaussian shapes. An expert could also (under)overestimate and should not be considered as an etalon. Generally, overall consistency is important. Despite the small range of potential neuron counts estimated by individual approaches (alg. 1 vs. alg. 2 vs. expert), we used a quadratic weighting criterion to include penalties for consistency evaluation (Cohen's Kappa for 2 Raters with squared weights). Relative and absolute exact matches are also given. We did not consider any outliers. The analyses presented herein were based on all available data. The outliers detection may yield more accurate results in the

Single Score Intraclass Correlation

Subjects = 45 Raters = 3 ICC = 0.69
F-Test H0: r0 = 0 ; H1: r0 > 0 F(44,49.1) = 9.02, p-val = 1.5e-12 **95%-CI:** 0.53 < ICC < 0.81

Squared Cohen's Kappa (expert vs. alg. 1)

Subjects = 45 Raters = 2 ICC Kappa = 0.85
absolute agreement = 32/45 z = 5.85 p-val = 5.07e-09

Squared Cohen's Kappa (expert vs. alg. 2)

Subjects = 45 Raters = 2 ICC Kappa = 0.62
absolute agreement = 27/45 z = 4.64 p-val = 3.55e-06

Table 4.1: Coefficients of inter-rater reliability and agreement.

future. In a relevant publication, Novak et al. suggests a precise methodology for estimating the number of neurons in extracellular recording based on GMM with more parameters than in our study [100]. But in our case, we show a comparison of GMM + BIC with K-means + GC.

We proposed two unsupervised spike sorting algorithms. Both algorithms can detect the optimal number of clusters (neurons) in neural recording. A substantial agreement of algorithms and expertise in detecting the number of neurons has been achieved.

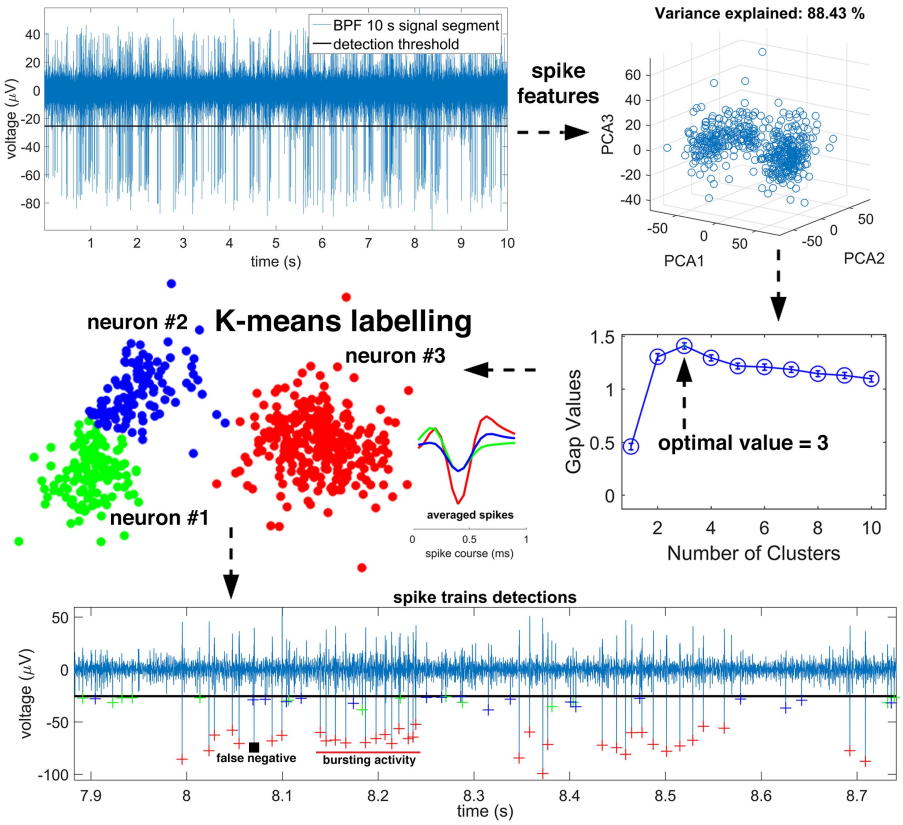

Figure 4.3: An example of the fully automated procedure based on alg. 1 applied to a 10 second signal segment. Implementation was provided in Matlab. Objectivization of processing MEA data led to finding 3 neurons. As a result, bursting activity is evident. The black square refers to a false negative detection due to the refractory period.

Chapter 5

Application of Spike Sorting Algorithm to Neuronal Signals Originated from Boron Doped Diamond MEAs

In this self-contained chapter I report on the implementation of methods for data processing of MEA signals and application of these methods on signals originated from two types of MEAs to detect putative neurons and sorted them into subpopulations. In the previous chapter, I have shown that these methods have the capacity to detect neurons using commercially-available TiN-MEAs.

5.1 Introduction

Prototyping and employing a certain type of custom-made MEA to record and analyse electrical signals from a cultivated population can be a valuable alternative to well-known commercial devices in specific cases, e.g. mapping of rat auditory cortex [101]. The electrode material is considered to be a key element for successful recording. The optimal material for electrodes should be mechanically stable, biocompatible, enable low-noise recording and allow easy surface chemical functionalization [97]. Diamond is generally considered as a biocompatible material, i.e. it is chemically non-cytotoxic when in contact with biological cells. The motivation for using diamond is the promise of improved durability and longevity sufficient for long term measurement. Another critical property of any electrode is its physical robustness with respect to mechanical damage.

Boron-doped diamond (BDD), which can be conveniently synthetized in the form of nanocrystalline films, exhibits exceptional properties that could make it a preferable material for neurolectrodes. Many functionalization routes are possible for the attachment of various molecules that can promote growth of neurons. An attractive feature of diamond is that it is insulating in its intrinsic form, but addition of boron atoms leads to material which exhibits semiconducting or even metallic form of conductivity and can be used for stimulation or detection of electrical signals from excitable cells.

However, bare BDD does not promote neural cell adhesion. Nevertheless, simple functionalization strategies make BDD a good substrate for adhesion and growth of primary neuronal cultures. This objective aims to optimize surface treatment of nanostructured BDD electrode which 1) allows long term cultivation of neurons, 2) does not interfere with electrochemical measurements and 3) reduces electrode fouling during detection.

Various studies have shown that BDD materials with suitable mechanical, electrical and biocompatibility properties have a large potential in novel therapies for treatments of neural pathologies, such as deep brain stimulation in Parkinson's disease, which is linked to abnormal extracellular neurochemical concentrations [38, 102–104]. Apart from excellent electrochemical properties and biocompatibility, BDD is a perspective material in terms of recording. Clinical DBS usually relies on pre-determined stimulation parameters in an open-loop configuration. Results by [38] suggest that BDD electrodes may be the solution for chronic DBS implantation, which could support long-term investigation of neurochemical responses in humans. This could potentially lead to close-loop in DBS and utilize neurochemical feedback to dynamically adjust stimulation parameters.

Furthermore, previous studies already demonstrated that BDD doping significantly improves the characteristics of sensing electrical signals [105, 106]. Demonstrated application of BDD-MEAs in the biomedical field include all diamond MEAs for recording of electrogenic cells [107] and nanostructured BDD for MEA neural interfacing [108]. However, these efforts have focused on the fabrication route challenges rather than on actual application of MEAs for recording from biological samples.

5.2 Development of BDD-MEA and Signal Acquisition

The whole microelectrode recording pipeline includes multiple steps ranging from initial sample preparation to analysis and interpretation. Extracellular neural activity was acquired by two MEA devices independently. For experiments, we used a commercial 60 channel TiN MEA (USB-ME64-System by Multi Channel Systems MCS GmbH, Reutlingen, Germany) as a reference platform (210 x 210 x 35 mm). 60 TiN electrodes are arranged in 8 x 8 grid, with a sampling rate of up to 50 kHz (Fig. 5.1C). The layout of the fabricated BDD-MEA is comparable to the commercial MEA (Fig. 5.1A), but due to technical reasons, the number of electrodes was reduced to 20 (Fig. 5.1D). Figure 5.1B corresponds to the distribution of contacts in Figure 5.1D with 20 electrodes. The visible imperfections, but still satisfying electrode alignment (Fig. 5.1B), is related to the ink-jet printing technology used to produce localized nano-diamond seeding prior to BDD growth, which still requires optimisation. A total of 4 BDD chambers have been prepared with this technology.

Deposition of BDD is realized using a linear antenna microwave plasma enhanced chemical vapour deposition system using conditions described in [109] to produce conductive diamond. Chip preparation included the fixation of a glass ring using Sylgard elastomer and sterilization. To control and optimize the electrode-neuron interface, chemical treatment of neuroelectrodes is usually performed by treating material with selected cationic polymer (most commonly polyethylenimin or polylysine). Chemical treatment of neuroelectrodes was performed by treating material with selected cationic polymer (poly-L-lysine). The role of this polymer is to enhance cell adherence to the surface and increase attachment of cells. This method builds upon previous results of molecular functionalization of planar nanocrystalline and porous nanostructured diamond to form an interface with new-born and adult neurons, which has been described in [109, 110].

Adult hippocampal neurons of male rats of the Wistar strain were used in this experiment and were handled in accordance with law no. 246/1992 of the Czech Republic and the current Guidelines for the Treatment of Laboratory Animals (EU Guidelines 86/609/EEC).

The reference TiN-MEA dataset contains 6 continuous measurements of spontaneous activity of 60 channels. Signal time series included quiet spots, bursting and isolated spikes (Fig. 5.1E). In the case of BDD-MEA, the dataset contains 9 continuous measurements of spontaneous activity of 20 channels. Each electrode corresponds to an input time series channel and the recorded files had a length of approximately 6 minutes with a sampling rate of 20 kHz. Initial measurements were started immediately after the preparation of neural cultures with spiking activity becoming apparent after 1 week. Spikes were recorded for 14 days under the same conditions. A raw BDD-MEA electrophysiological picture of the neurons is presented in Figure 5.1F.

5.3 Signal Processing

In order to obtain individual spikes from microelectrode recordings, I implemented the automated analytical pipeline (previous chapter): containing signal band-pass filtering (Butterworth 2nd in the 500–5000 Hz band), spike detection, spike sorting and individual spike train features computation. The proposed pipeline in Matlab was applied to automate the extraction of neuron signals from both types of MEAs.

Signals were band-pass filtered (Butterworth 2nd) over the 300–3000 Hz range. The number and time location of spikes were detected by the spike detection process. Since the detection trade-off is related to the signal to noise ratio of the recording, an amplitude WaveClus detector was used for spike detection (Table 5.1).

To capture the time courses (20 shape-based features) of truly positive spikes, we used a threshold cut-off (Thr) of 5 times the standard deviation of

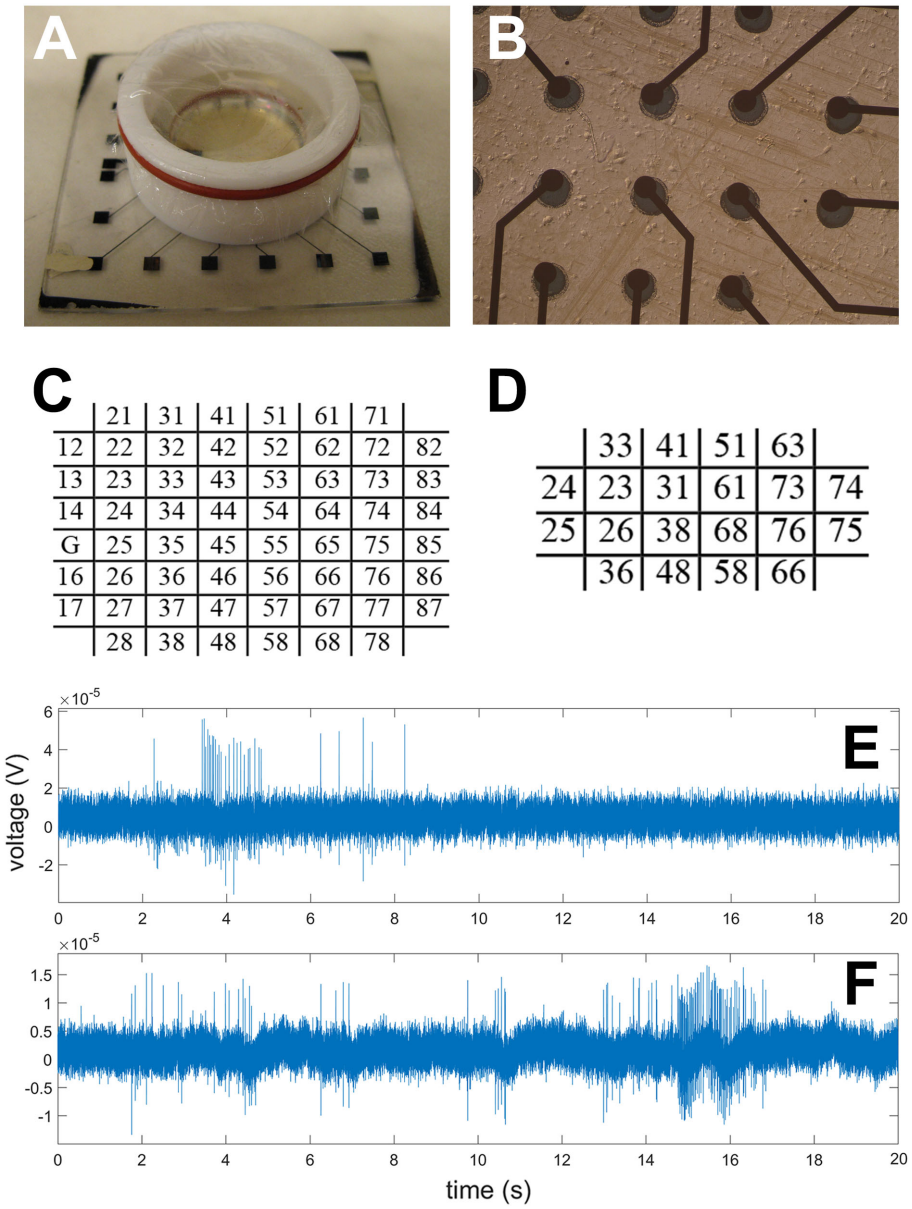

Figure 5.1: Signal acquisition of neuronal activity on MEAs. A) BDD-MEA with glass ring and gas permeable membrane lid. B) BDD-MEA with visible hippocampal neurites and neurons growth across electrodes. C) Reference TiN-MEA electrode distribution. (G = ground). D) BDD TiN-MEA electrode distribution. E) Raw recording of spontaneous hippocampal neuronal activity recorded in vitro from TiN-MEA. F) Raw recording of spontaneous hippocampal neuronal activity recorded in vitro from BDD-MEA. Peaks represent a spike, bursting activity is also evident. The noise level is around ± 5 μV while signal amplitudes are from ± 15 μV.

the input signal noise. Each detected spike bounded by a range of the pre- and post-event data points was modulated by a cubic spline curve and 20

hyperparameter	value
minimum refractory period (data points)	36
number of pre-event data points stored	10
number of post-event data points stored	10
spike waveform interpolation	cubic spline
maximum detection threshold	$30\sigma_{signal}$

Table 5.1: Waveclus detector: an overview of the set hyperparameters.

equidistant shape-based features were computed (Table 5.1). Numerically, each row (i.e. spike waveform shape) in the dataset is represented by a vector of 20 numbers determining the neural morphologies and the distances and orientations relative to the recording electrode. The main output of the detection function from the whole duration and all channels contains indexes of detected peak positions, threshold amplitudes and associated waveforms. For downstream analysis, we included only active channels. The channel must detect at least 20 spikes in order for the channel to be considered active.

5.4 Data Evaluation

For data exploration, we investigated transformations of individual spike waveforms through embedding into a lower dimension. We anticipated extending Principal Component Analysis (PCA) with UMAP (Uniform Manifold Approximation and Projection) and replacing the subsequent clustering K-means algorithm with Louvain method. Namely, the current pipeline contains clustering and identification of waveforms types on the principle of Scanpy package in Python [111], which stands out in its ability to identify subpopulations in single cell data. We reduced the dimensionality of the data by running PCA, which reveals the main axes of variation and denoises the waveforms data. Then we computed the neighbourhood graph matrix using the 5 PCAs representation of the data matrix based on similarity of waveforms. We embedded the neighbourhood graph (n = 10) in 2 dimensions using UMAP with ScanPy default settings. Finally, the unsupervised Louvain graph-clustering method directly clusters the neighbourhood graph of waveforms to sort them automatically into subpopulations.

The level of spike-to-spike variability was further evaluated for the sorted spikes. We implemented the method published by [112]. Spike variability was calculated so that a variability of 0 indicated that every spike waveform from a given neuron was exactly the same (i.e. no variability) and that variability approached 1 as noise began to dominate the waveforms (i.e. spike shapes became random). Each spike in a unique putative neuron was then compared to the mean spike for that neuron using the dot product (cosine distance). The mean of the distribution of dot product values for all spikes provided a measure of the variability from spike to spike, independent of any amplitude changes (since the spike vectors were normalised). [112]

We continued by checking for consistency between spike-to-spike variability and a second alternative variability estimation approach. For each putative neuron, the median from absolute values of individual coefficients of variation (CV) across individual 20 shape-based features was calculated. Distributions with a CV found to be less than 1 were considered to be low-variance, whereas those with a CV higher than 1 were considered to be high variance.

As voltages and spike-to-spike parameters were not found to be normally distributed by the one-sample Shapiro-Wilk test, statistical comparisons were performed using a non-parametric Mann-Whitney test. The correlation was assessed using the Spearman correlation coefficient, which measures monotonic relationship. The statistical significance was determined as $p = 0.05$.

5.5 Results

Detected waveforms across all the measurements (>20 spikes on recording) were projected into a reduced UMAP space, as can be seen in Fig. 5.2E. Evaluation of voltage waveforms collected from BDD-MEA ($n = 10403$) vs. commercially available TiN-MEA ($n = 11346$) reveals that they differ mostly in amplitude values ($p < 0.05$). Significantly smaller amplitudes were observed in BDD-MEA. The differences in amplitudes could be caused by HW and may not reflect a difference in physiology. Furthermore, we determined clusters using the unsupervised Louvain method, which found 14 waveform subpopulations (Fig. 5.2C). By assigning waveforms to subpopulations, in total 35 putative neurons in TiN-MEA and 31 putative neurons in BDD-MEA were found. Examples of variability in neuronal shapes for both types of MEAs are illustrated in Figure 5.2B.

Statistical testing did not show any significant difference ($p = 0.27$) in the spike-to-spike variability in BDD-MEA ($n = 31$) vs. TiN-MEA ($n = 35$), which supports the hypothesis that we detect real neurons rather than noise in the BDD signals. With the same Thr = 5, BDD-MEA has a slightly higher level of variability ($0.09 \pm$ (SD) 0.07) against ($0.09 \pm$ (SD) 0.05) for TiN-MEA (Fig. 5.2D). Scatter plot demonstrated significant consistency (rho = 0.43; $p < 0.001$) of both methods for variability estimation (Fig. 5.2A). Given the CV variability could be sensitive to outliers, the value of correlation coefficient is not representing a completely tight relationship. Overall, the detection method proves to be feasible for detection from various biological samples.

5.6 Discussion of the Proposed Method

Apart from the clear BDD spike activity, we have noticed some other activities on some of the electrodes whose origin we do not understand. Either they are minor events covered in noise, but by shape they could be normal activity, only recorded from a greater distance, or with a worse contact. We even saw

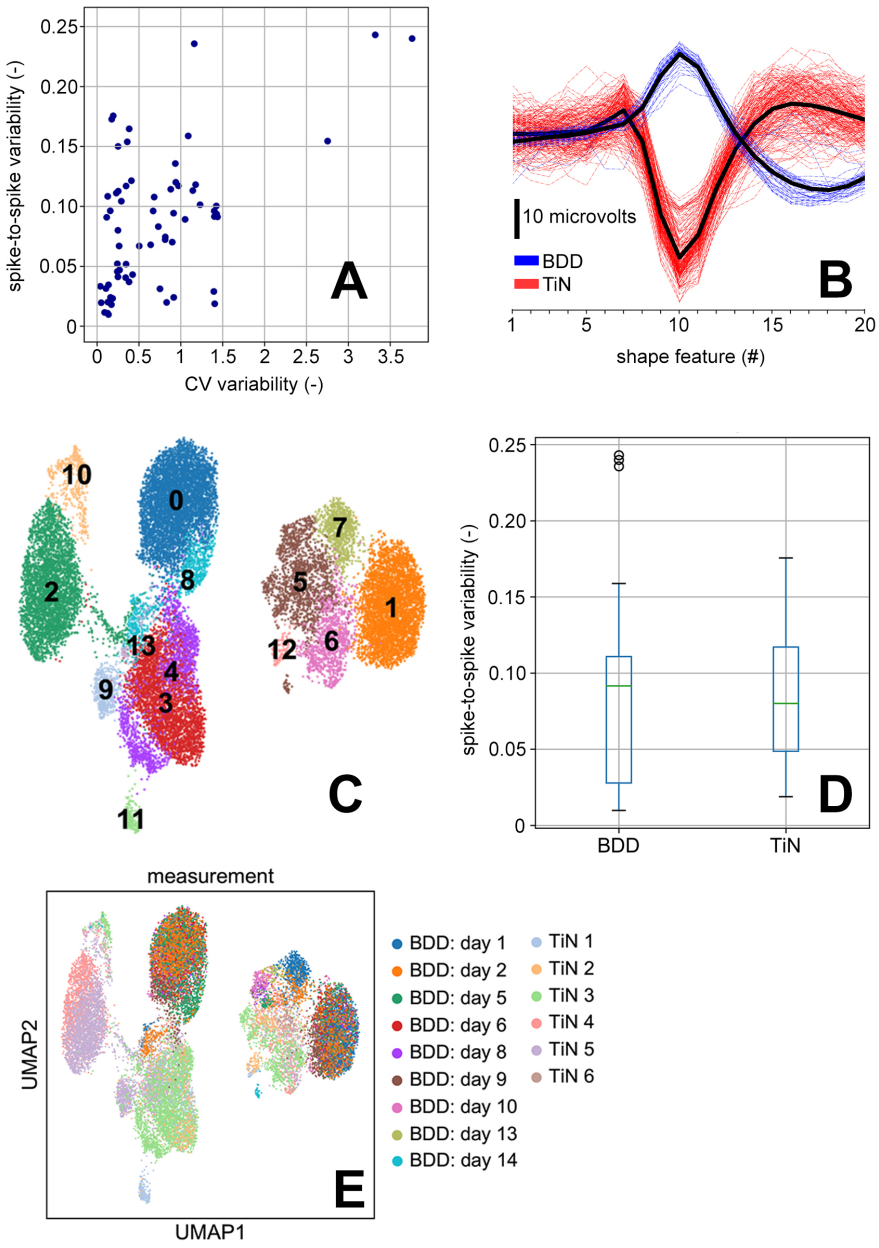

Figure 5.2: A) Scatter plot representing relationship between both variability estimations. B) Example spikes from both types of MEAs. The mean spikes (black) and the spikes of those means. C) UMAP plot visualizing cluster assignments of waveforms which are defined by Louvain clustering and denoted as distinct colours. D) Distribution of spike-to-spike variability via boxplots. E) Colouring by individual measurements.

events of a completely different shape, whose origin is unknown. Sometimes rectangular events were recorded, which look like neural channel openings. However, their length was several times the length of the normal spike and

were suppressed by filtering.

Comparing the performance of UMAP with five other tools, UMAP should provide the fastest run times, highest reproducibility and the most meaningful organization of cell clusters [113]. The most notable is that UMAP, like t-distributed Stochastic Neighbor Embedding, does not completely preserve density and can also create clusters that are not actually present, resulting in a finer clustering than is necessarily present in the data. On the other hand, the UMAP visualisations with apparent separation of data could facilitate discovery of rare spikes population, which would not be possible without upgrading our pipeline.

Finding action potentials in a signal based on their shape, in other words, template matching, is another method of spike detection. It uses a manually created database of spike shapes, with which parts of the signal are continuously compared. With this method, it is possible to achieve much better results than simply thresholding the signal [114]. However, as each neuron or group of neurons has a different characteristic spike shape, use of this method requires manual creation of a database of spike shapes for each analysed signal. Therefore, this method is unsuitable for automatic spike detection.

The BDD-MEA density of the electrodes is lower compared to the TiN-MEA, which leads to a lower resolution of the electrophysiological picture of the neuronal network and therefore to a lower statistical significance with regard to the interpretation of the network functionality. To record all 20 channels at 20 kHz generates a huge amount of data. A six-minute recording creates a file, which is 1 GB in size. In order to analyse this data, high demands must be placed on hardware and software. [115]

We ultimately aim at the development of BDD MEA for dual recording, which will employ BDD based micro-probes positioned within close proximity of a firing neuron on an MEA electrode for simultaneous recording of electrical and chemical activity. As a first step towards this goal, we have measured cyclic voltammograms (Fig. 5.3) recorded on BDD micro-probe demonstrating dopamine detection under simulation conditions, i.e. controlled release into cell culture dishes to characterize micro-probe sensitivity [116, 117].

Sensors and methods for electrical and chemical detection have importance for both scientific reasons and treatments of neurological diseases. For example in PD, the concentration of dopamine is lower than the physiological level. This neurochemical disorder causes a high frequency spike burst of the neurons, which induces muscle tremor. Obtaining simultaneously neuroelectrical and neurochemical information would help elucidate cause–effect relationships between the two modes.

In conclusion, we have presented extracellular recordings, from cultures of hippocampal neurons on BDD-MEAs over a period of weeks allowing analysis of network development. Previous research showed only signals without closer analysis of BDD-MEA spikes [108]. Depositing nanostructured BDD onto the neuroelectrodes makes it possible to obtain dual mode low-noise neuroelectrical and neurochemical information simultaneously [118]. The device

used for neurochemical detection is important for the research and treatment of neurological diseases. Monitoring of neurochemical activity (neurotransmitters or metabolites) can bring new insights in describing dopaminergic neurons, e.g. in Substantia Nigra in PD [38].

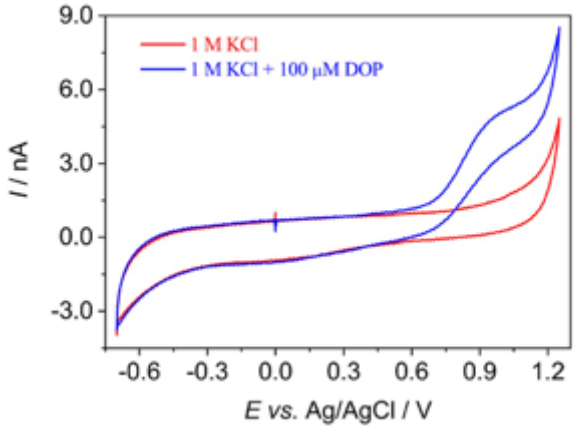

Figure 5.3: Cyclic voltammograms recorded on BDD micro-probe demonstrating dopamine (DOP) detection.

Chapter 6

A Novel Deep Learning Approach for Signal Preprocessing and Identification of Microrecording Artifacts

Intraoperative microelectrode recordings are prone to several artifacts (up to 25%). Essentially, the three most common classes of artifacts that can be identified [119]:

- A mechanical movement artifact, manifested by short-time, high-power signal peaks, usually spread across the whole frequency spectrum.
- Low-frequency interference below the mains frequency (50 Hz), causing visible variation in the signal offset or in the baseline.
- Electromagnetic interference at one or multiple stable frequencies, well localized in a narrow band(s) in the frequency spectrum and stable over time. The frequency of the observed long-term interference often differs from the expected odd harmonics of the mains frequency (50 Hz, 150 Hz, 250 Hz etc.).

Detection of these artifacts is not straightforward, potential artifacts emerge from several sources and may not be present in all signals. Detection of artifacts is an essential phase of MER processing and can have a significant influence on spike sorting [119], and subsequently the determination of clinically interesting biomarkers. Therefore, prior to spike detection, artifacts should automatically be removed from the signal in order to prevent spike-dependent statistics (i.e. compound firing rate) and spectral measures from being biased [120]. In clinical practice, sensors containing the artifacts are typically manually curated and artifacts are removed after visual inspection.

Artifact detection in MER signals is an area with few objectively validated methods [119,121–124] acting as change-point detection or detectors of significant changes compared to the clean signal spectrum. Many researchers use their own (semi)automatic methods, ranging from simple amplitude thresholding [125] through statistical testing of the amplitude distribution in short signal windows [126].

A distinction has to be made between the externally induced artifacts (i.e. the scope of this chapter) and "background noise" in MER, which commonly refers to the recorded activity of neurons further away from the electrode in single/multiunit activity processing [127].

The potential of the development of beneficial medical diagnostic computer programs is enhanced by machine learning methods. In general, the application of deep learning in recent years is increasing and has been shown to be a more accurate and progressive technique in various fields of medical applications, e.g. in computer vision, natural language processing, electronic health record data or bioinformatics [128], [129].

The demand for computer vision applications is higher than ever before. Computer vision is a subfield of artificial intelligence that is focused on enabling computers to interpret and understand the visual world. Every industry from finance to healthcare has lots of repetitive tasks that can easily be automated using modern computer vision techniques:

- image segmentation,
- object detection,
- image classification,
- object tracking,
- image generation,
- face detection,
- optical character recognition.

In particular, many studies that deal with the analysis of biomedical signals can be documented. Bursa et al. applied a continuous wavelet transform (CWT) to a fetal heart rate signal processing with different levels of time/frequency detail parameters and in two different resolutions. The output 2D structures are fed to a convolutional neural network (CNN) [130]. A CNN is one of the main design representatives of deep learning, which is inspired by the organization of the animal visual cortex. Many challenges for object classification, detection or semantic segmentation have been solved in the field of neuroscience [131]. The findings described in a paper titled CNN to Model Articulation Impairments in Patients with PD, presented new results in speech impairments using deep learning algorithms, the Fourier transform and a CWT deployed on a voiced and unvoiced segment for the classification of PD vs. healthy speakers [132]. Another clinical study demonstrated the feasibility of using deep learning as part of an electromyographic hand gesture signal classification system [133]. Furthermore, Acharya et al., designed and predicted normal, preictal, and seizure EEG signals, based on a 13-layer CNN [134].

Up-to-date research has uncovered findings on the many applications of deep learning in biosignal event detection, specifically in the field of cardiology [135]. For example, Yildirim et al. proposed an algorithm for arrhythmia detection [136]. Researchers found that the AI algorithm successfully predicted distinct diagnostic classes encompassing a normal sinus rhythm, pacemaker rhythm and other rhythm disorders effectively from an analysis of 10-s ECG signal fragments. In addition to the CNN, a recurrent long-short term memory network is suitable for an ECG classification [137]. However, there haven't been any studies to address the potential benefits of MER-DBS processing via deep learning.

Currently, there are a wide variety of powerful deep learning frameworks including e.g. MATLAB for Deep Learning, TensorFlow with Keras, PyTorch and Caffe2. Most of them support interoperability with open source deep learning frameworks using ONNX import and export capabilities.

The main goal of this chapter is to develop an algorithm capable of detecting individual classes of artifacts, corresponding artifacts onset times and localization of the area in the MER in which artifacts originate. We present a novel CNN approach to microelectrode activity artifact detection by means of neural networks in biomeasurement. Fig. 6.1 schematically shows the network architecture and the main task presented herein. Standard example for machine learning is we got some data, we feed it to a model and then it gives us prediction and error. Here, explainable deep learning is about looking at that data and saying why does this data conclude this prediction.

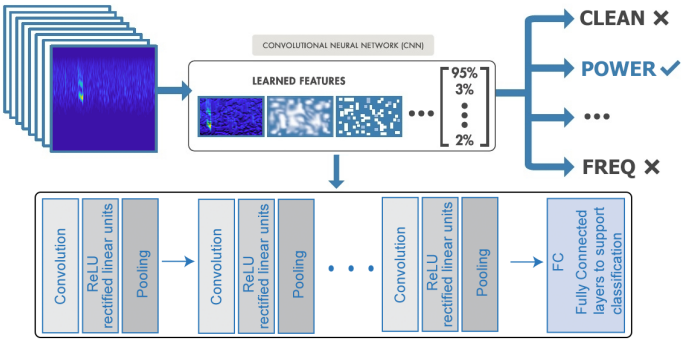

Figure 6.1: A deep learning workflow. For example, images are passed to the CNN, which automatically learns features and classifies MER segments. Conceptual illustration adapted with quoting [138].

6.1 Subjects and Methods

6.1.1 Patients

We evaluated all the proposed methods on a manually annotated database [119] of thousands of ten-second MER signals from 58 PD patients. The ma-

jority of them didn't contain any contamination (about 75%). The study was conducted in compliance with the Declaration of Helsinki and was approved by the Ethics Committee of the Department of Neurology, 1st Faculty of Medicine and General University Hospital in Prague. DBS electrodes were bilaterally implanted using standard stereotactic methods and incorporating intraoperative microelectrode recordings from the humal basal ganglia. Every participant signed an informed consent before enrolment in the study.

The sampling rate was 12 kHz and the signals were recorded with a Medtronic LeadPoint System (Medtronic, Minn., MN, USA). Internally, the signals were upsampled by a factor of 2. Digitized data was retrieved via the Leadpoint Export Utility (Medtronic, Minn., MN, USA). Band-pass filtering was applied (Butterworth 2nd order) in the 0.5–5 kHz band prior to artifact detection. The implantation procedure and domain-specific methodological details can be found in Chapter 7. The preprocessed dataset consisted of approximately 100000 one-second signal segments.

Our data collection process was administered by a group of trained specialists (manual). Overall, there was quite a bit of noise in the annotations (the raters didn't match, there weren't exact beginnings and endings of the artifacts). If an artifact emerged within 1 second, considering a fixed segmentation of the signal, the segment was marked as an artifact (+ its putative class) and each segment was ranked from one up to five raters. With more than two judges, the majority opinion was chosen (consensus). This methodology has already been described in [119].

6.1.2 Time-Frequency Representation

Feature extraction from the data could help improve the training and testing accuracies of the classifier. We considered a time-frequency representation that extracts information from the 1D MER segment (Fig. 6.2). Namely, using the continuous wavelet transform. A scalogram is then the absolute value of the CWT coefficients of a signal. Our requirements for the 2D representation were met by the Matlab implementation, which sets the default analytical Morse (3, 60) wavelet, where the symmetry is 3 and the time-bandwidth product is 60. The Morlet wavelet analysis has already shown appropriate properties for intracranial EEG [139], [140]. Each color JPEG image was saved to the size of 227-by-227-by-3 pixels.

6.1.3 CNN Architecture and Settings

We employed deep transfer learning with a convolutional neural network based on AlexNet [141]. AlexNet is a CNN that is trained on more than a million images from the ImageNet database (image-net.org). We reused the network architecture of the CNN to classify microelectrode signal segments based on images from the CWT of the time series data. Currently the best performing neural networks were originally designed to classify images into

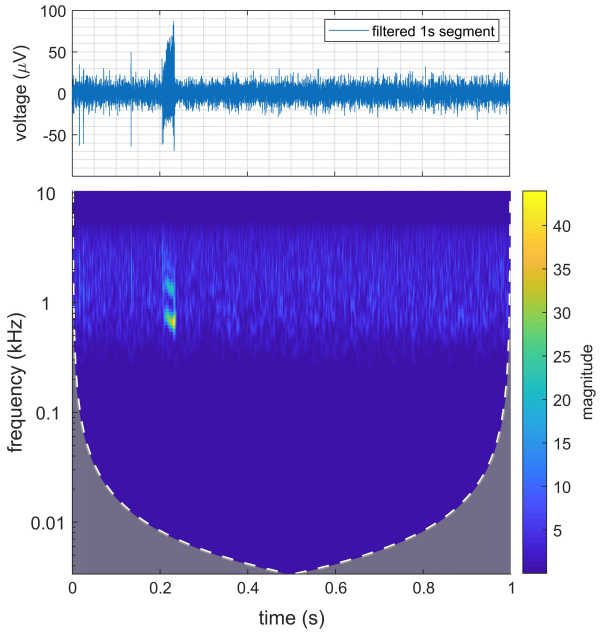

Figure 6.2: A one-second filtered signal segment and its corresponding 2D representation with an obvious short-living power artifact. Artifact activity is often accompanied by an increase of signal energy in particular frequency bands.

1000 categories. This creates major advantages for medical imaging. We were able to train the networks on smaller datasets because we were able to use pretrained models. Then, only a small weight update was needed for our specific task.

Training a deep CNN from scratch is computationally expensive and requires a large amount of training data. In various applications, a sufficient amount of training data is not available, and synthesizing new realistic training examples is not feasible. In these cases, leveraging existing neural networks that have been trained on large data sets for conceptually similar tasks is desirable. This leveraging of existing neural networks is called transfer learning. The assumption that you can train an initial model on large relevant data and transfer the hidden layers of that model to a new one, which will be developed with less focused data is valid as we suppose that low level features are the same for all types of images. Thus, the CNN design consisted of the following steps:

- Create (taken from AlexNet) and add a new twenty-third layer including weight initialization and activation.
- Compile models including loss function (1), optimization method (2) and metrics (3), (4).
- Fit models to include learning rate, epochs and batch size.

Essentially, the widely used optimization stochastic gradient descent algorithm might oscillate along the path of steepest descent towards the optimum. Adding a momentum term to the parameter update is a way to reduce this oscillation [142]. The stochastic gradient descent with a momentum update algorithm is employed to optimize the loss function (1):

$$\theta_{l+1} = \theta_l - \alpha \nabla L(\theta_l) + \gamma(\theta_l - \theta_{l-1}) \tag{6.1}$$

where l stands for the iteration number, $\alpha > 0$ is the learning rate, θ is the parameter vector, $L(\theta_l)$ is the loss function, and γ determines the contribution of the previous gradient step to the current iteration.

The optimization algorithm finds weights and bias values that minimize the loss function (2):

$$L = -\sum_{j=1}^{C} y_j log(p_j) \tag{6.2}$$

where C is the number of target classes, y_j indicates that example i has label c, and p_j indicates predicted probability of class c for image x. We used the supervised method, thus we had to divide the dataset into a training, validation and test subset, where the validation set is also used for over-fitting evaluation.

Networks were implemented in Deep Learning Toolbox environment of the Matlab 2018b. We accelerated the training processes by setting the option to run on the GPU (NVIDIA GeForce GTX 1060 6GB).

6.1.4 Baseline

For CNN performance benchmarking, we annotated an available in-house database with two state-of-the-art methods proposed by Bakstein et al., including a default thresholds and settings [119]. Two methods, COV (autocorrelation-based approach) and MaxDiffPSD (maximum spectral difference method), were specifically reimplemented and optimized for the automatic detection of artifacts in microelectrode recordings [119], [124].

COV is a stationary segmentation method based on the variance of the signal autocorrelation function. The signal was first divided into short fixed-length segments. Subsequently, the variance ratio of the statistics of neighboring signal segments was computed. The method computes the distance matrix between all possible segment pairs and searches for the largest available component, connected by a sub-threshold path. Assuming higher stationarity in the clean signal segments, rather than in the artifact segments, the largest component is then marked as a clean signal, while the remaining signal

sections are marked as artifacts. In terms of implementation, the COV classification was calculated for the entire ten-second signal and then divided into one-second segments.

MaxDiffPSD is a simpler detection method, based on the power spectral density of MER signals. The basic assumption is that the power spectral density (PSD) of a clean band-pass filtered MER signal is smooth, unlike most signals with artifacts, which commonly contain high peaks and other disturbances. In terms of implementation, MaxDiffPSD works natively with a single one-second window without the context of the entire signal.

6.1.5 Evaluation Metrics and Statistical Methods

The performance of the detector was determined by a parameter that is based on the comparison of the judgment of an expert (manual) and the artifact detection results. Although expert assessment is considered as a reference gold standard, infallibility in artifact labeling cannot be expected and evaluations are strongly subjective and influenced by many factors, e.g. due to the general description of multi-trajectories of recordings, difficult differentiation of clean and neural activity with artifacts, subjective criteria of the evaluator and many more. One would expect the possibility of an expert ignoring clear artifacts or even labelling an activity that does not fully meet the criteria for the artifact. Therefore, consistent results cannot be expected, but the detectors performance should approximate the reference and also bring novelty value [143], [144].

Receiver operating characteristic (ROC) curve analysis was performed to assess diagnostic accuracy. We incorporated the R statistical software environment and pROC package [145], that is a set of tools to visualize, smooth and compare receiver operating characteristic (ROC curves). Areas under the curve (AUC) can be compared between individual machine learning models with statistical tests based on U-statistics (DeLong's test for two correlated ROC curves) or bootstrap. Statistical tests of the hypotheses were considered significant at $\alpha = 0.05$.

The overall accuracy of the binary models was determined from the confusion matrix using the following formula (3):

$$accuracy = \frac{TP + FN}{TP + FP + TN + FN} \tag{6.3}$$

This formula represents the ratio of correctly classified segments to all the segments in the dataset (TP: True Positive, FN: False Negative, TN: True Negative, FP: False Positive). In extending a binary metric to a multiclass problem, the data was treated as a collection of binary problems, one for each class. There are several ways to average binary metric calculations across the set of classes, each of which may be useful in some scenarios. We simply

calculated the macro mean of the binary metrics, giving equal weight to each class.

The proportion of correct predictions may not be useful when the two classes are of very different sizes. In addition to the accuracy and AUC-ROC and due to the fact that the previous methods were optimized on real imbalanced data [119] we employed the Matthews Correlation Coefficient (MCC) metrics. MCC serves as a description of the optimal classifier for imbalanced data. The MCC returns value in the interval $[-1, 1]$, with 1 showing a complete agreement, -1 with a complete disagreement, and 0 showing that the prediction was uncorrelated with the ground truth [146]. MCC scores (4) were calculated via the R mccr package:

$$MCC = \frac{TP \times TN - FP \times FN}{\sqrt{(TP + FP)(TP + FN)(TN + FP)(TN + FN)}} \tag{6.4}$$

We have also further assessed the Precision-Recall (PR) curves. PR is a useful way to measure the success of the prediction when the classes are very imbalanced. These quantities are related to the F1 score, which is defined as the harmonic mean of precision and recall.

6.1.6 CNN MER Validation Methodology

In this study, we implemented two CNNs with the corresponding learning split-validation strategies:

- *The imbalanced case for comparison among different algorithms.* This model assumes that we classified only 2 distinct categories (clean – 0 vs. contaminated segment – 1). 5340 images were used for the training and 4930 for neural network testing, therefore 3560 images were reserved for validation and hyperparameter settings.
- *The multiclass balanced case for detection of different artifacts classes* (a finite set of species such as “power”, “freq” and “baseline”). We had to redefine the last AlexNet CNN layer for 3 output classes. 567 of images were used for training and 227 for neural network testing, therefore 340 images were reserved for validation and hyperparameter settings. 378 images were available for each class representative.

In both cases, the hyperparameters finally used for offering the best results were set to 0.001 for learning rate, 0.9 for momentum, 50 training epochs and batch size of 50 samples. To finally determine what the actual classes are, the AlexNet layer has the categories of classification. Soft-labels were converted for each input as the maximum probability value. Because of computer memory limitations, we used a subsampling of our in-house database using random selection (uniformly distributed to avoid a bias) and we covered

representatives across the database for all the specific requirements for two split-validation strategies. The training phases ended after a significant decrease in validation accuracy.

6.2 Results

In order to illustrate the performance of the deep learning framework on MER data, a series of experiments were carried out.

6.2.1 CNN is Successful in Detecting Artifacts

First, we tested imbalanced benchmarking—optimized for real MERs with many clean segments. By running some benchmarking on existing models with binary predictions to see how feasible our CNN approach is (AUC-ROC = 0.75; MCC = 0.59; F1 = 0.64) we obtained a substantial performance increase (DeLong's test for two correlated ROC curves) against the results of the COV (AUC-ROC = 0.58; MCC = 0.2; F1 = 0.31) method ($p < 0.001$) and then we revealed a statistically significant improvement in comparison with MaxDiffPSD (AUC-ROC = 0.73; MCC = 0.54; F1 = 0.60; $p = 0.0497$). In all the benchmarks, CNN reported performances that were comparable and even superior to other state-of-the-art methods. The MCC metrics reflect a strong positive relationship with ground truth (+.40 to +.69) and a weak positive relationship (+.20 to +.29), respectively.

Fig. 6.3 shows an example of the evolution of the accuracy achieved during the training phase of the AlexNet network using the validation images of our dataset.

The results from the testing datasets are shown as a confusion matrix for all the artifact detectors (Fig. 6.4). The CNN based approach was shown to have an accuracy of 88.1%.

Figures of ROC and PR curves and their areas including probabilistic CNN soft-labels are presented in Fig. 6.5 and Fig. 6.6.

Although a high computational cost is typical for deep learning architectures during training, the evaluation phase is very quick and efficient. Processing of 1-s MER segment took on average 0.885 (std. 0.039) seconds for the CWT computation and 0.005 (std. 0.0004) seconds for the CNN evaluation on a standard i5 2.8 GHz PC with 8 GB RAM (Table 6.1).

6.2.2 CNN Can Distinguish Among Classes of Artifacts

As a second result, we determined balanced-data multiclass CNN results with a prediction accuracy of 75.3%, which is a noticeably good level and clearly reveals the effectiveness of the proposed method as presented in Fig. 6.7. It was observed that both power and baseline groups had comparable accuracy

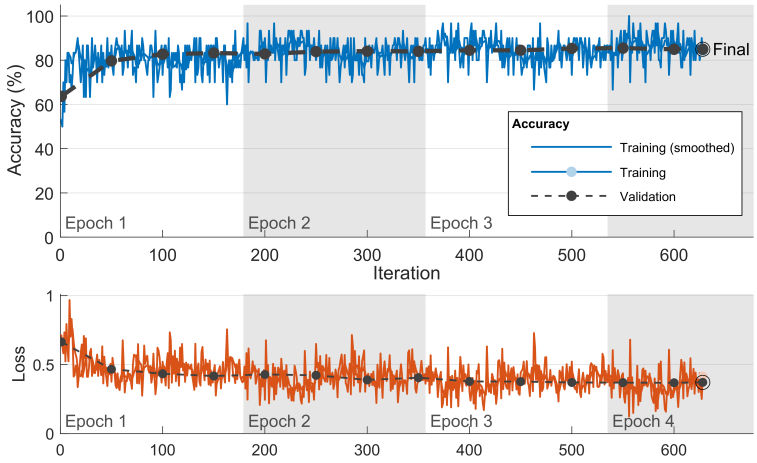

Figure 6.3: Preview the learning process. Plot of model accuracy on training and validation dataset. From the plots of accuracy and loss is evident that the model has a comparable performance on both training and validation datasets. The final total learning time of the network was very fast (in minutes). Herein it was manually stopped.

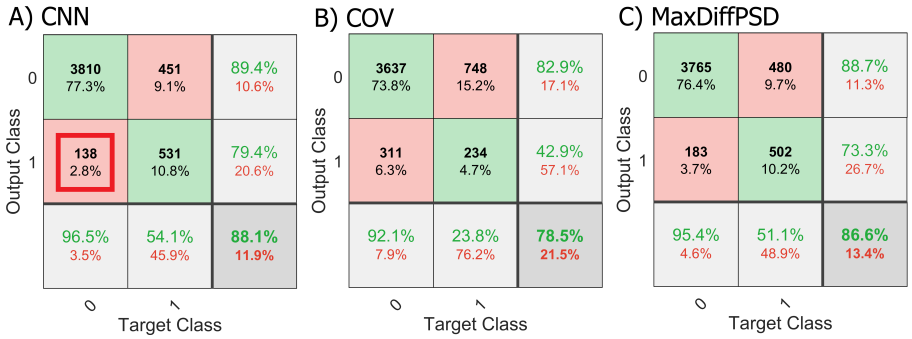

Figure 6.4: Confusion matrices for imbalanced cases show the distribution of the test segments into false/true positives/negatives. A summary of the statistics is given in the last rows/columns. A: CNN. The neural network can identify candidates for artifacts which could have been missed (red box). B: COV. C: MaxDiffPSD.

values. The biggest difference was given for the frequency label. Frequency and baseline artifacts were incorrectly labelled as a power contamination several times. By accessing "soft-labels", the user can adjust the sensitivity for each type of artifact, so that there is a higher sensitivity for the types that are more troublesome.

6.2.3 Detailed Focus on Artifacts

Each layer of a CNN produces a response, or activation, to an input image. However, there are only a few layers within the CNN that are suitable for image feature extraction. The layers at the beginning of the network

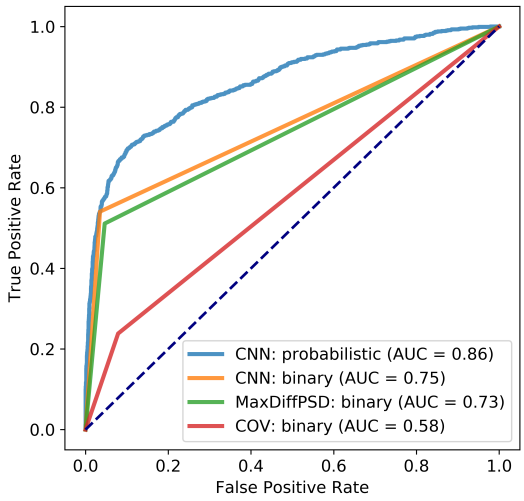

Figure 6.5: ROC curves for individual models to evaluate output quality. Binary inputs give one point on the ROC curve while the probabilistic CNN returns a smooth curve where an optimal point could be found.

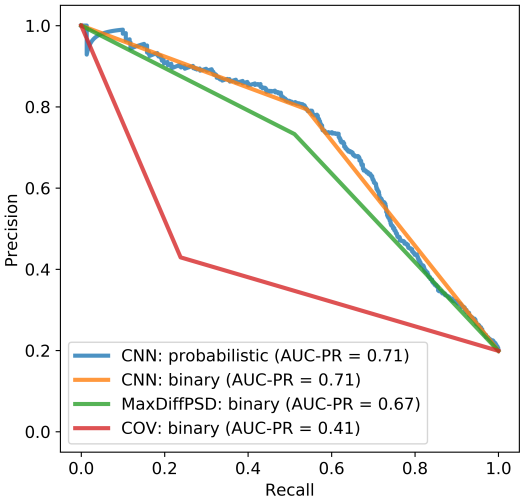

Figure 6.6: Precision-Recall curves. Unlike the ROC curve, PR curves are very sensitive to imbalance. A classifier optimized for good AUC-ROC on an unbalanced data is likely to obtain poor PR results.

capture basic image features, such as edges and blobs. We examined the activations and discovered which features AlexNet learned by comparing areas of activation with the original image. Our method detected artifacts and focused on the most activated areas (Fig. 6.8).

Statistic	CWT	CNN	CWT+CNN
mean	0.8850	0.0048	0.8897
standard deviation	0.0385	0.0004	0.0385
min	0.7978	0.0045	0.8025
50% percentile	0.8863	0.0047	0.8910
max	2.3352	0.0126	2.3399

Table 6.1: Descriptive statistics that summarize the speed of computation in seconds (4930 images).

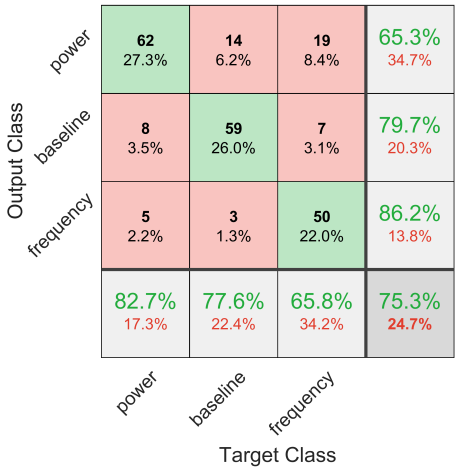

Figure 6.7: Multiclass classification using a CNN detector on the testing set.

6.3 Discussion

This chapter applies deep learning strategy to classifying artifacts in Parkinson's disease microelectrode recordings. This method could be of potential interest not only for invasive recordings but also in noninvasive ones (e.g. electroencephalography). The data was first preprocessed via wavelet transformation and then analyzed using convolutional neural network. Evaluation criteria showed that the proposed algorithms obtained the following knowledge:

- CNN results are at least comparable to the previous simple methods (Fig. 6.4, Fig. 6.5, Fig. 6.6).
- Individual classes of artifacts are recognizable (Fig. 6.7).
- Our method implemented the active layer highlighting as feedback so that an expert can make better decision (Fig. 6.8).

Our novel approach is bench-marked on a gold-standard dataset and is supported by experimental validation. The performance of the CNN algorithm was compared with existing methods (MaxDiffPSD, COV) and relevant

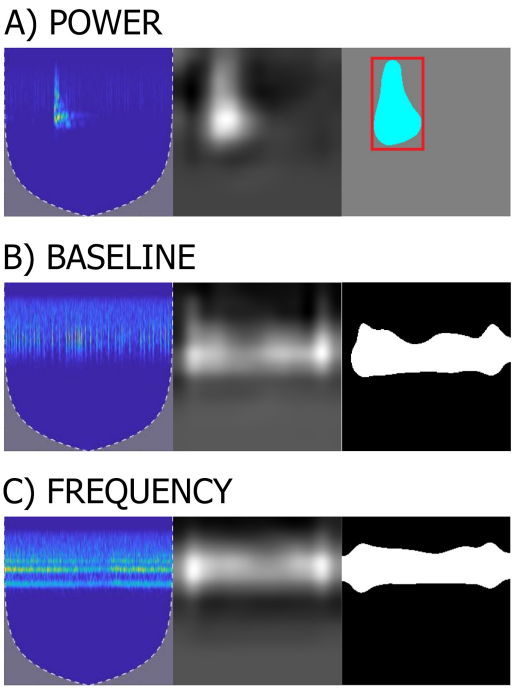

Figure 6.8: Our methodology was able to find the strongest channel for a particular MER segment class (A, B, C) and mark the exact artifact onset time. Herein, we compared the strongest channel with the original image (first columns of A, B, C). Information retrieval was performed on the strongest channel in the 5th Convolutional Layer (second columns of A, B, C). Using the automatic Otsu's global threshold segmentation (third columns of A, B, C), image parameters are extracted (red box) from the artifact (Table 6.2).

statistics are given (e.g. AUC-ROC, AUC-PR, accuracy, MCC). The results indicated that all metrics were highest for CNN. Indeed, the simplest method MaxDiffPSD achieved almost the same performance as the deep learning (CNN) method. But, in addition to the ability to successfully classify, our network can also decide which class of artifact is present (multiclass problem). This is a respectable result if one considers that the task was quite complex. In this regard, only artifact classes of interest can be selected/classified, which is a real new feature and advantage over the state-of-the art methods and the article [119].

Subsequently, we confirmed our hypothesis of its capacity to report the most activated layer and to localize the area of the MER in which artifacts originate. The authors of the AlexNet stated in their original paper that their model is capable of identifying the region of interest on the image [147]. Therefore, we have adapted this proven model for our problem. Our approach uniquely allows for targeting the time location of the artifact in a one-second segment, which has not been previously designed and implemented. To accurately evaluate the onset/offset of each identified artifact, we do not have labeled data for objective validation nor a means to aggregate the 2D binary matrix into one dimension. So, this feature cannot be compared with

Feature	Value (mostly pixel-based)
Centroid	[71.94 83.45]
BoundingBox	[43.50 16.50 64 115]
MajorAxisLength	115.59
MinorAxisLength	57.14
Area	4622
Eccentricity	0.87
Orientation	-85.03
ConvexArea	5055
Perimeter	285.60

Table 6.2: Example measurements for the set of properties for each recognized artifact object in the binary image.

identification based on state-of-art methods (e.g. MaxDiffPSD). Moreover, this is even beyond the capacity of state-of-art methods.

The one type of existing state-of-the-art methods for artifact detection in single-channel MER that has been rigorously tested is unsupervised change-point detection [119, 121–123]. The authors presented the extremely high detection accuracies of change-point detection, which were almost 100% on simulated data. We show that real-world validation performance may not be as robust when the problem is evaluated as supervised (COV accuracy = 78.5%). Among others, the COV method typically labels a segment as an artifact when an artifact was not present (a common case for a large sudden spike). Such problems can be overcome by a CNN.

Offline analysis is of no use to neurosurgeons. A quick (within 0.5-1.0 second) result of the calculation is desirable during the MER recording in the surgery room. Our solution meets these requirements with processing speeds below 0.9 seconds (Table 6.1). A time analysis was performed on all test data (4930 images) and classification by the saved model for the new image was very fast. As shown, it takes nearly 1 second to calculate the CWT and resize the image. The proposed techniques could be implemented during surgery for near real-time applications of detecting artifact classes or potential biomarkers. CWT + CNN seems to be an effective way to extract hidden information from a MER in DBS.

Research in the field of DBS-MER processing has historically been limited due to low volumes of annotated data. Despite this fact, we have a large and comprehensive dataset, gathered from electrodes implanted in the brain, offering a lot of randomly selected trajectories of ten-second long brain activity recordings. In the presented problem, we have thousands of training samples and there were no obvious effects of overfitting. This method appears to be transferable to other datasets and we plan to apply it in dystonia (Chapter 7).

This chapter presents several evident advances but also contains limitations. We have evaluated several combinations of the hyperparameters of the CNN to be tuned, but we have not systematically performed the hyperparameter

optimization. In this regard, we have only retrained AlexNet for 2 resp. 3 output classes in the last layer. This has allowed for a small subset of weights to be changed, while the majority of the initially optimized core AlexNet weights were retained, so we leveraged the AlexNet optimization process. We would rather refer to how the hyperparameters were systematically optimized in the original architecture [147]. Nevertheless, a deeper analysis of the hyperparameters can lead to even better results [148]. It is apparent that the loss functions decreased during training and we captured the artifact patterns successfully.

AlexNet is already dated architecture. For further research, we would consider novel deep learning architectures such as Inception [149], residual networks [150], or dense-net [151] to improve the results. It has been shown that other architecture and resizing of the input image may have a significant effect on the accuracy of the classification and the current satisfactory accuracy could increase by more than 10% [152].

In the future, we offer a semi-supervised principle—namely, submitting vague images for re-evaluation by the rater. We identified the active learning approach as a viable route for further research.

6.4 Conclusion

Currently, there is a variety of software methods that can enable detection of DBS biomarkers. Such software will enable spike sorting, spike clustering and network synchronization analysis. Therefore, the concept of microrecording seems very attractive and promising in the tailoring of individual patient therapy. This chapter illustrates an innovative approach for microelectrode recordings processing. The main result is the implementation of an artifact detector based on the convolutional neural network. To our knowledge, deep learning in the field of DBS has not been studied yet. This automatic approach can lead to improved DBS diagnostic procedures and can improve DBS effectiveness. The results suggest that the presented methodology is promising for DBS signal processing evaluation and is able to capture more hidden patterns in MER data, specifically not only artifacts, but also, for example, some other characteristic features (neuronal firing or even identifying potential candidates for biomarkers). It can be applied to any movement disorders in deep brain stimulation procedure implantation.

Part III

Application Results in Clinical Neurophysiology

Chapter 7

Microelectrode Neuronal Activity of the Internal Globus Pallidus in Dystonia Correlates with Postoperative Neuromodulation Effects and Placement of the Stimulation Electrode

- Unambiguous criteria for DBS implantation performance in dystonia are not yet known.
- The methodology for processing microrecording signals has been implemented.
- Microelectrode recordings were evaluated in 13 dystonic patients with GPi-DBS.
- The electrophysiological biomarker is correlated with the long-term neuromodulation effect.
- Contact localization along the medio-lateral direction may affect postoperative DBS effect.

In the following text, I present a comprehensive methodology for analyzing electrophysiological recordings of patient neuronal activity. This chapter is a part of research in the field of deep brain stimulation and accurate targeting of stimulation electrodes into the Globus Pallidus internus. DBS is a neurosurgical symptomatic treatment proposed mainly for PD, essential tremor and OCD, but also for dystonia. In this case, as well as for treating axial symptoms of PD, the target deep brain structure is the GPi. Even now, the success of this complex surgery remains highly correlated to the experience of the surgeon and/or of the neurologist in the surgical team, since no perfect method exists for optimal placement of stimulation electrodes. The method described in this chapter aims at proposing a signal processing- and machine learning-based approach to the optimal placement of electrodes in

GPi. I describe the method in detail and present results obtained in the group of 13 patients chronically treated with double-sided deep brain stimulation.

Microelectrode recordings are used to diagnose the correct location of the DBS electrode. Technologically, the set that passes through the brain and records the action potentials of several of the surrounding neurons (typically max. 5). Achieving the optimal DBS position is a key element in producing a positive therapeutic effect. Presently, the placement suitability is judged primarily by a neurologist, either visually or acoustically, based on a specific expression of neuronal action potentials.

7.1 Methods

7.1.1 Patients and Clinical Data

This study includes data from the Department of Neurology, General University Hospital in Prague. The study was conducted in compliance with the Declaration of Helsinki and was approved by the Ethics Committee of the General University Hospital in Prague. We included 13 patients (Table 7.1) with heterogeneous dystonia (7F, 6M, mean age: 47.8 ± (SD) 13.5 y.) chronically treated with double-sided DBS of the posteroventro-lateral portion of the GPi. DBS electrodes were bilaterally implanted using standard stereotactic methods and incorporating intraoperative microelectrode recording using the following stimulation settings (avgs: voltage = 1.9 V, current = 1.8 mA; DBS: 50-130 Hz). Detailed neurosurgical protocols with annotations were documented. Every participant signed an informed consent before enrolment in the study.

The long-term effect (LTE; 38.8 ± (SD) 42.6%) was determined as a change in the dystonic score (Burke Fahn Marsden Dystonia Scale (BFMDS) in generalized dystonia, Toronto Western Spasmodic Torticollis Rating Scale (TWSTRS) in cervical dystonia) between the postoperative status with the pallidal DBS switched on and preoperative status. We consider the LTE > 50% as a responder (N = 6). In contrast, 3 patients showed a negative LTE.

7.1.2 DBS Implantation Procedure and Signal Acquisition

In total endotracheal anaesthesia, a stereotactic device was established and access to the basal ganglia was provided. The patient was then awakened allowing the neurologist to communicate with the patient to ensure that the intended parts of the brain are stimulated. MER activity was recorded using microelectrodes in several parallel trajectories, which are used for GPi detection (Fig. 7.1A). A prediction of the target position was performed by skiagraphy. A permanent stimulation electrode (Fig. 7.1B) was implanted into the best trajectory to the right and left according to neurological expertise operating protocol, and then the skiagraphy targeting was inspected (Fig. 7.2).

ID, sex	implantation (age)	onset (age)	duration (years)	aetiology	DBS sensitivity		LTE (%)	type
1m	37	27	10	ACTB	R	R	79	GD
2f	54	27	27	PINK1	P	N	44	GD
3m	31	20	11	Parkinson	N	N	-14	GD
4f	25	15	10	PKAN	N	N	-19	GD
5f	36	11	25	DYT1	R	R	91	GD
6f	44	22	22	idiopathic	P	N	21	CD
7f	52	35	17	idiopathic	P	N	45	CD
8m	68	56	12	idiopathic	R	R	100	GD
9m	43	31	12	idiopathic	R	R	67	CD
10m	76	62	14	KMT2B	R	R	63	GD
11f	43	26	17	idiopathic	N	N	-26	GD
12m	57	47	10	idiopathic	R	R	72	CD
13f	58	43	15	idiopathic	P	N	21	CD

Table 7.1: (cervical dystonia), GD (generalized dystonia), 1st column DBS sensitivity: N = non-responder (0 – 25% improvement in dystonic score after DBS implantation), P = partial responder (25 – 50% improvement), R = responder (at least 50% improvement); 2nd column: N = non-responder (0 – 50% improvement), R = responder (at least 50% improvement); ACTB = mutation in the beta-actin gene (OMIM:607371), PINK1 = young-onset Parkinson disease (OMIM:608309), PKAN = panthothenate kinase-associated neurodegeneration (OMIM:234200), DYT1 = torsion dystonia (OMIM:128100), KMT2B = childhood-onset (OMIM:606834)

A T1-weighted 1.5 T MRI brain imaging (MPRAGE, 0.9x0.9x0.9 mm) was examined in each patient after the implantation of the electrodes. Coordinates were measured in native space using susceptible artifacts at the contact location of the electrode. The x-coordinate (x-distance) of each contact was measured in the medio-lateral direction at a distance from the third chamber wall.

Many trajectory depths were recorded, from -10 mm up to +4 mm, for the intended target = 0 mm. The GPi was most often found from -6 mm to +2 mm, where the distal end of the DBS electrode was located near the planned position at a depth of 0. To reduce the risk of bleeding, the recommended microelectrode speed is < 0.5 mm/s.

The sampling rate was 24 kHz and the record length at each depth was recorded for 10 seconds with a Medtronic LeadPoint System. The recorded electrodes typically have a resistance of 1 MΩ (at 1000 Hz). The digitized data was retrieved via the Leadpoint Export Utility (Medtronic, Minn., MN, USA). Export is available in micro and millivolts units. The typical number of files per patient is greater than 1000. Signals were band-pass filtered (Butterworth 2nd order) in the 0.5–5 kHz band. The bandpass filter was used to remove the slow shift, which can significantly influence signal properties and spike detection. All the processing steps were provided by developed batches of MATLAB scripts. Due to the small size of the electrode tip (1 μm) and the low voltage of the source signal, a MER is predisposed to mechanical and electromagnetic interference, creating artifacts (see Chapter 6).

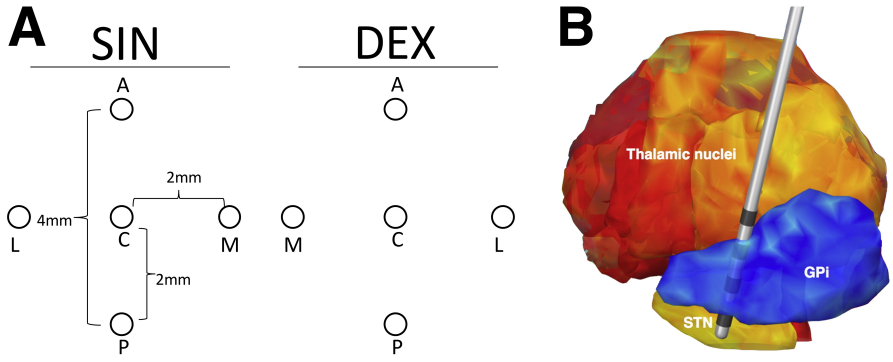

Figure 7.1: An illustration of two types of electrodes in this study. A) Five parallel trajectories in a cross, A – anterior, C – central, L – lateral, M – medial, P – posterior, the trajectory with the best micro activity was selected by the neurologist. B) DBS permanent electrode targetted in GPi, scheme reprinted from [153], with quoting. SIN: left side, DEX: right side.

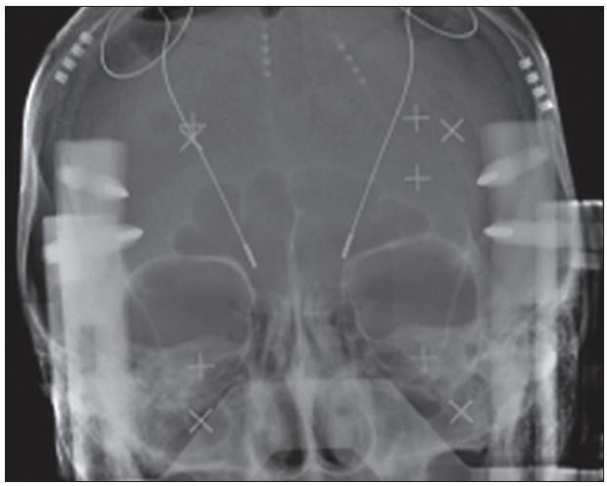

Figure 7.2: An illustration of an intraoperative X-ray scanning deep electrodes in the basal ganglia (originates from the in-house database).

7.1.3 Leadpoint Export Utility – Data Conversion

Signals obtained during DBS implantation were converted to the .txt files using the Leadpoint Export Utility. Data conversion through the desktop application consists of five steps.

The first step is selecting the patient whose data we want to export. Following phase is the selection of channels. In the next step, user can select specific signals from available channels. All available channels for all the patients were converted successfully. Each MER signal is displayed with channel ID, position and time, see Fig. 7.3. Subsequently, options for selecting the format, content and structure of the header file, exporting all channels into one folder, and saving the exported file are enabled. Converting data into the text files took about 3 hours for 28 patients.

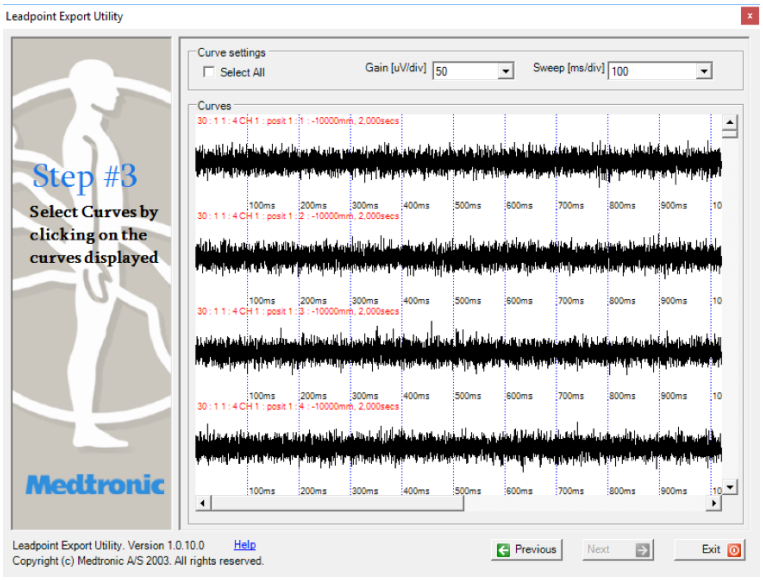

Figure 7.3: Software Leadpoint Export Utility.

pat ID	bilateral	depth range [mm]	notes
1	1	-10000; 4000	3 el – centr, med, lat
2	0	-10000; 1500	-
3	0	-10000; 1000	dex 3 el – centr, med, lat
4	1	-10000; 500	3 el – med, centr, lat

Table 7.2: An example of a directory structure.

To control the accuracy of data export and easy access for the subsequent analysis, a directory structure was created based on the file header and information available from the raw folders. Table 7.2 serves as a demonstration of the directory structure. The header file contains a list and description of all available files. The first column representing the names of the files obtained after the conversion. The following is the patient's name and surname, date when the procedure was performed, the dex/sin is describing DBS bilaterality. The note column is containing the name of the original file, and the last column showing the depths in which the MER signals were recorded. Further information such as sampling frequency, channel, length and description of signal recording are also written in the header file (Fig. 7.4).

7.1.4 MER Artifacts Detection

As it has been already described in the Chapter 6. The artifacts in a MER are divided into three groups in a simplified way: basic, power and frequency. Basic artifacts are the result of interference with the low frequencies that cause oscillation of the base line of the signal. Power artifacts are described as large changes in the signal amplitude. It lasts from 100 ms to 2 seconds. It is mainly caused by the patient's movements during the recording.

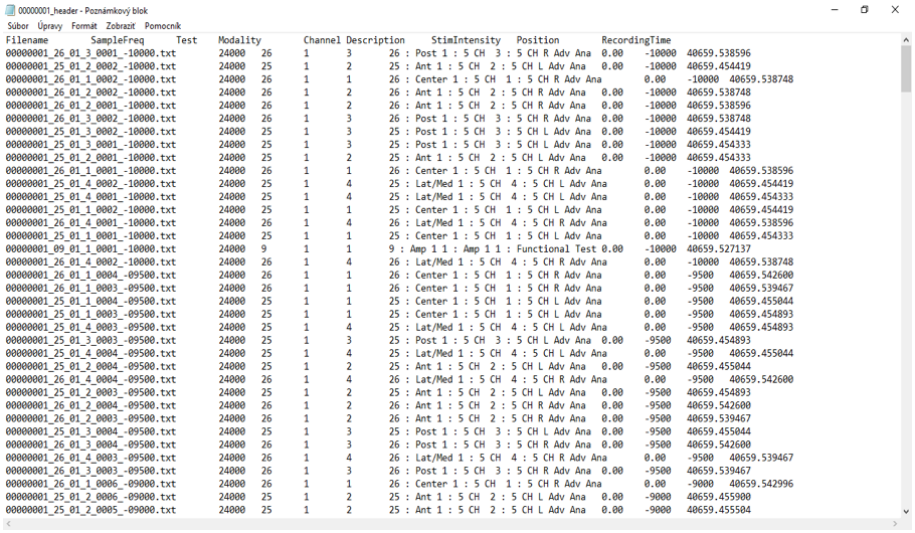

Figure 7.4: Example Leadpoint header file from patient ID11.

Technical artifacts are represented by a long-term constant frequency in the signal frequency spectrum. Technical artifacts come from electromagnetic interference from other devices, such as lights and instruments in the operating room. Two automatic classification methods were implemented based on an available MATLAB toolbox [119] and their consensus for artifact removal was considered (MaxDiffPSD and COV).

Finally, we chose a more conservative approach for the resulting artifact detection. If the sample was automatically classified by at least one of the methods, then it was an artifact that was subsequently removed from the signal. Artifact-free segments were glued with a piecewise cubic interpolation to alleviate possible rapid point changes. Signals shorter than 5 seconds were not considered for further analysis.

7.1.5 Feature Extraction

Five whole-signal features independent of signal length were calculated based on the analysis of a 10 second MER. Previously [154], 13 features were used to describe the STN within a MER in PD, mostly requiring spike detection prior to calculation. With inspiration and de novo design, we used the following markers to describe the GPi and its vicinity.

Normalized Root Mean Square (NRMS)

The root-mean-square (RMS) level of a MER reflects the signal energy:

$$MER_{rms} = \sqrt{\frac{1}{N}\sum_{n=1}^{N}(MER_n)^2} \tag{7.1}$$

RMS values were normalized relative to the average RMS values from the first five depths in the trajectory due to different possible impedances (NRMS).

Hjort mobility (hjort)

A Hjort mobility parameter is defined as the square root of the ratio of the variance of the first derivative of the signal and that of the signal (2). This parameter has a proportion of standard deviation of the power spectrum [155].

$$MER_{hjort} = \sqrt{\frac{var(\frac{dMER}{dt})}{var(MER)}} \tag{7.2}$$

Spikes per second (spiking)

The number of spikes detected by the spike detection process. Since the detection trade-off is related to the signal to noise ratio of the recording, an amplitude WaveClus detector was used for spike detection [72]. The number of spikes was normalized by a signal length in seconds (spikes per second).

$$Thr = 4\sigma_n, \sigma_n = median\left\{\frac{|MER|}{0.6745}\right\} \tag{7.3}$$

Nonlinear energy (nonlin)

The nonlinear Teager-Kaiser Energy Operator (TEO) is considered to be a very high resolution energy operator. TEO is determined as [156]:

$$max(MER^2[n] + MER[n-1]MER[n+1]) \tag{7.4}$$

Cepstral coeffs (ceps)

Since neurologists assess signals by listening, we included an audio signal processing parameter typically describing mp3 files. MEL-Frequency Cepstral Coefficients (MFCC) have parametric features based on the perceptual bandwidth of the human hearing system [157]. An average from 13 MFCC values were used for signal description according to [158].

7.1.6 Statistical Methods

Offline scripts for all analytical experiments have been implemented in the Matlab (Mathworks, USA). The study was conducted in accordance with the Cross-Industry Process for Data Mining methodology. Paired Wilcoxon test was used for hypothesis testing. Averaged activity across the GPi in a certain trajectory was input for the testing. The relationship of variables was assessed by the Spearman correlation coefficient. Robust bisquare type regression was used for relationship modelling. P-values of 0.05 or lower were considered as statistically significant.

7.1.7 Machine Learning Methods

We trained 3 supervised machine learning models for obtaining a discriminative power based on the AUC: Logistic Regression, Linear Support Vector Machine and Naive Bayes. Model implementations included validation on the training input data and a 5-fold cross validation. The accuracy of the values obtained employing the models was calculated using a confusion matrix. Averaged activity across the GPi in a certain trajectory was input for the discriminative models (positive class) vs. its vicinity (negative class). ROC curve analysis was performed to assess the diagnostic accuracy. The area under the ROC curve (AUC) results were considered as excellent for AUC values between 0.9-1, AUC values between 0.8-0.9 were considered as good and AUC values between 0.5-0.6 would have failed the accuracy test [159].

7.2 Results

The following results were obtained from the available patient recordings that were preprocessed, including artifacts detection and features computation (Fig. 7.5). Semi-automatic analysis involved processing thousands of recordings. Partially annotated and processed recordings were input for statistical evaluation.

7.2.1 GPi Nucleus Activity Differs from Its Vicinity

By using the NRMS, we visualized the values of the parameter in the best trajectories selected by neurologist. Annotations contain data where the GPi begins and ends according to the operating protocol. The NRMS parameter can distinguish the GPi core from its vicinity (preGPi) (Fig. 7.6).

The beginning of the GPi was not annotated in many of the operating protocols and the NRMS parameter was used to recognize it based on the profile of the NRMS trajectory shape and expertise knowledge. We processed 26 paired values (preGPi vs. GPi), left and right sides together (Fig. 7.7). We found a significant difference in NRMS ($p < 0.001$). The area under the curve

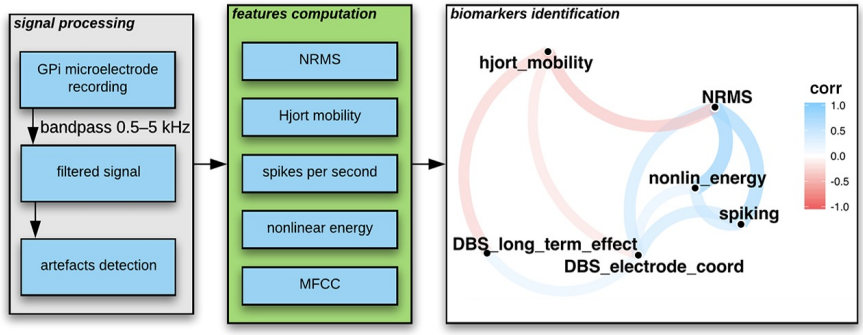

Figure 7.5: High level overview. Correlation network of the biomarkers was computed by mutidimensional scaling method.

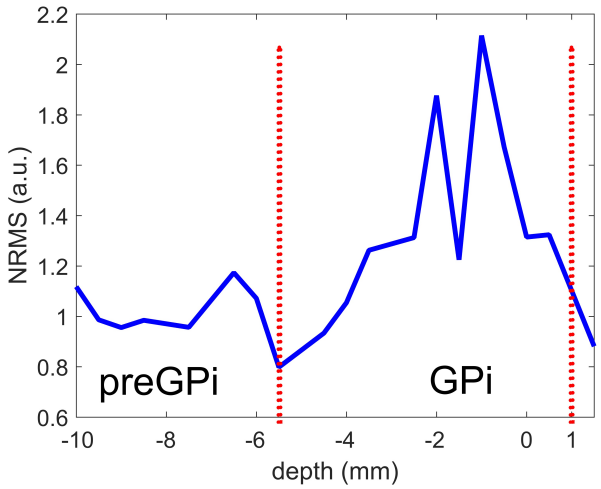

Figure 7.6: An example of the central NRMS trajectory course. GPi annotations show where the GPi was located (vertical dashed red lines). The final target was in +1 mm.

for 5-fold cross validated Linear SVM model was 0.91, which corresponds to an excellent classifier. In this regard, a cross validated model slightly outperforms model fit on the training data (Fig. 7.7B).

NRMS can be considered as a predictor of the location of the GPi. The second important fact that is visible from Fig. 7.8 is that many other computed parameters are significantly correlated within the GPi. No differences were found between the left vs. right side: NRMS: $p = 0.54$, hjort: $p = 0.15$, spiking: $p = 0.64$, nonlin: $p = 0.34$, ceps: $p = 0.06$.

7.2.2 GPi Nucleus Activity Correlates with Postoperative Neuromodulation Effects

It has been shown that the antidystonic benefit of pallidal DBS, expressed in standardized long term effects, is quantitatively related to the Hjort

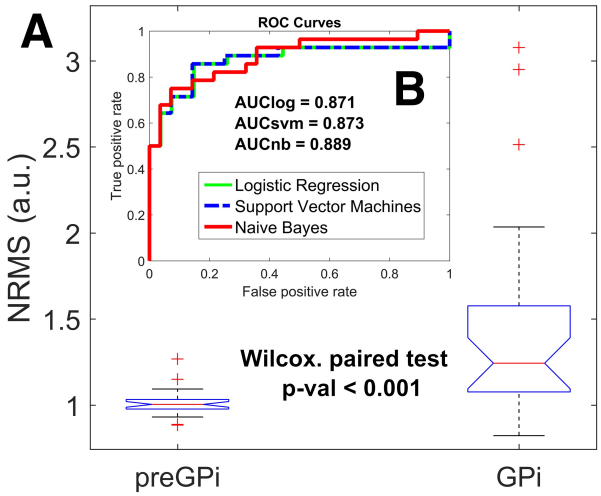

Figure 7.7: A) Boxplots preGPi vs. GPi. The Wilcoxon test demonstrates a significant difference in GPi detection. B) The nested graph describes 3 trained classifiers with the calculation of posterior probabilities using validation on the training data, which also demonstrated high discriminative powers (min. AUC > 0.87; n = 52; 26 preGPi vs. 26 GPi).

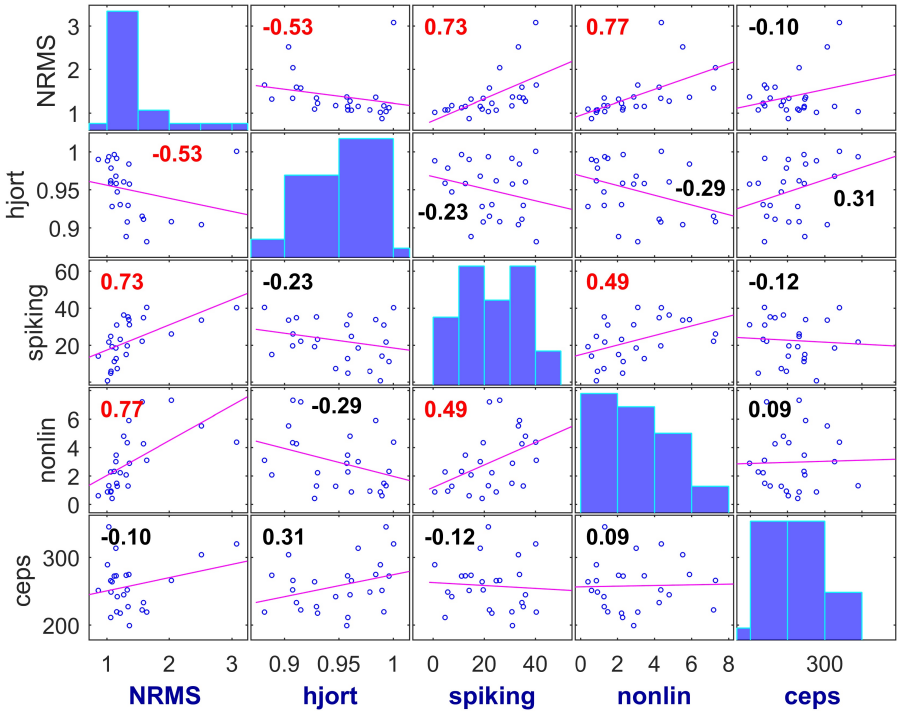

Figure 7.8: Correlation scatter plots of the computed parameters. The red mark indicates a significant correlation.

mobility parameter. Based on the correlation analysis, it was shown that hjort correlates negatively with the antidystonic effect expressed by LTE (Spearman's rho = –0.4; $p < 0.05$) (Fig. 7.9). Moreover, LTE is in line

with the acute effect of DBS (postoperative DBS OFF vs. ON; rho = 0.54; p = 0.04).

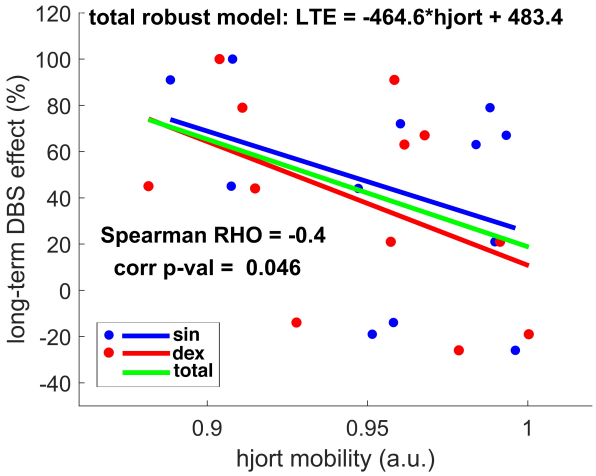

Figure 7.9: The quantitative relationship between the LTE and the biomarker. The relationship is further described by a linear equation obtained by robust regression.

7.2.3 GPi Nucleus Activity Correlates with the Neurosurgical Placement of the Stimulation Electrode

The coordinates of the placement of the stimulation electrodes were known in 12 patients. The highest GPi neuronal activity was found in patients with the active contacts placed laterally (Fig. 7.10). Namely, we have revealed a significant increase in activity associated with the medio-lateral direction (NRMS rho = 0.51, spiking rho = 0.5; $p < 0.05$).

7.3 Discussion

The main finding is the quantitative relationship between the electrophysiological parameter and the clinical score. Hjort mobility is a parameter that reflects the dispersion of spectrum values. Therefore, the relationship suggests that the signal of the responder will dominate in a narrow spectral component, which is probably related to GPi neuronal activity, which occurs around 600 Hz (spike duration is 1.5 ms). We have also found that the correlation with LTE is quite comparable on the both the left and right side. Their relationship is not completely tight—there is a trend, but there is also interpersonal variability. However, the multi-correlation structure (Fig. 7.8) ensures that more than one parameter is transitive related to a clinical scale, but more data would be needed to make these relationships significant at under $p < 0.05$.

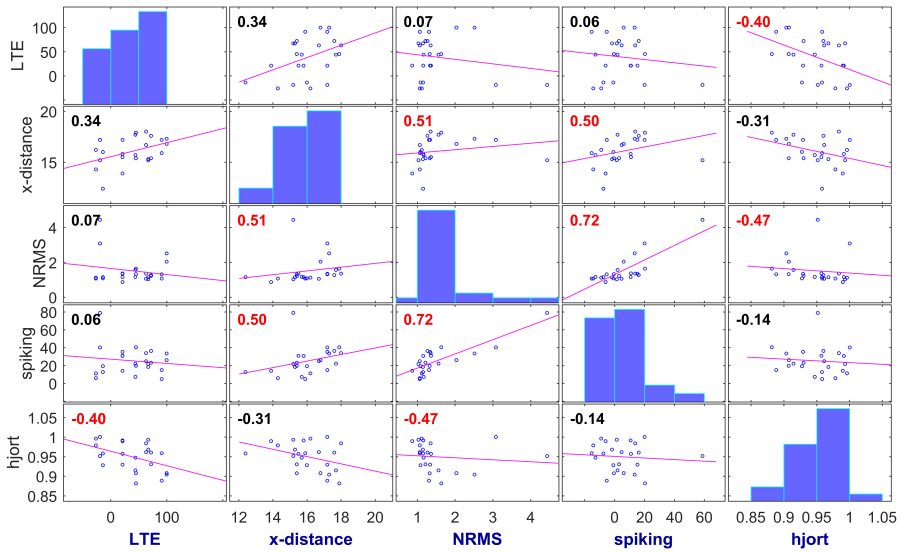

Figure 7.10: The multi-correlation structure represents the relationship between the change in the LTE of the pallidal DBS, the distal contact distance of the DBS electrode from the third chamber wall and electrophysiological parameters. In some cases, outliers that reduce the correlation coefficients are evident. X-distance: the distance of the distal contact from the third chamber wall in the medio-lateral direction (mm).

The recognition of the GPi is based on the NRMS. The problem with GPi detection can be given when there is another basal ganglia nucleus in front of the GPi. This issue will be examined in the future. We plan to map 3D anatomical models using Lead-DBS software package [153] .

Since neurologists generally "listen" the electrode signals, their audio content is definitively informative, so we included the psychoacoustic properties such as MFCCs. But the correlation analysis shows finally that the MFCC feature carries no information useful for classification. We conclude that the averaging operation muffle a potential distinctive psychoacoustic property.

From a modern research perspective it can be stated that we have found a similar biomarker, which is related to the signal spectrum as Neumann et al. [57]. However, in that study they examined patients with cervical dystonia and focused on the theta activity. Correlations of the biomarkers were given the same absolute value (rho = 0.4). Also, in the future theta activity can be tested with our data.

The clinical effects of pallidal stimulation in dystonia were quantitatively related to the placement of the stimulation electrode in the direction of the medio-lateral axis and electrophysiological parameters. It could therefore show evidence of the presence of a motor gradient within the GPi along the medio-lateral axis, which reflects the long-term clinical effect of DBS in dystonia, regardless of its aetiology. Our results follow previous research showing a relationship between the deterioration of speech fluency and the

medio-lateral placement of the DBS GPi electrode [43]. It can be assumed that patients who have electrodes placed too medially will benefit little or insufficiently. The position of the x-axis active contact in conjunction with biomarker value should be the main predictor of the future success of the DBS GPi. These phenomena were significant in spite of the large phenotypic and genotypic heterogeneity of dystonic syndromes, suggesting a common pathophysiological mechanism that DBS GPi induces. This research supports the current hypothesis that the GPi also has some mapping as a macro brain. We acknowledge that no control group was included due to inherent challenges of intraoperative recording.

Traditional recording methods such as functional magnetic resonance imaging are capable of recording a summarized activity of a population of neurons in a particular area of the brain but gives no information about individual neurons. We have analysed the neuronal activity of the GPi, but in the future it is also possible to focus on the GPe. In conclusion, we have shown that the NRMS is a GPi predictor and the other parameters are correlated, which generally reflects the patient's long-term effect.

We assume that this research will contribute to a better description of the type of GPi neurons involved in motor and non-motor functions, as well as a better understanding of the underlying mechanisms of deep brain stimulation.

7.4 Conclusion

The methodology for processing MER signals during the DBS implantation procedure has been implemented. This paper has demonstrated the quantitative relationship between electrophysiological findings and the clinical effects of pallidal stimulation in dystonia and suggested objectification predictors of the effectiveness in this therapy. Last but not least, the GPi nucleus location in dystonia has been described, which will help in further clinical analyses. This result gives the chance to optimally target stereotactic surgery for patients who will be implanted in the future and can give hope for existing non-responders for a successful reoperation.

Chapter 8

Reshaping Cortical Activity with Subthalamic Stimulation in Parkinson's Disease During Finger Tapping and Gait Mapped by Near Infrared Spectroscopy

The brain and its functions are inherently multiscale, that is, they consist of multiple spatial and temporal scales. For instance, their descriptions may involve at the molecular, cellular, microcircuit, brain-wide network, and cognitive and behavioural levels. Within each level, the timescales can vary widely. Further, subsystems may interact and influence each other across scales. This chapter describes how DBS, which was implanted based on the manifestations of individual neurons during microrecording, affects the patterns of cortex activation in simple motor task and gait.

- This chapter shows how fNIRS can be used to detect functional changes in the motor cortex with DBS-STN.
- DBS-STN led to an increased activity in the contralateral motor cortex areas during finger tapping.
- This is the first study to investigate gait in Parkinson's disease with DBS using multichannel fNIRS imaging.

8.1 Introduction

Motor cortex activity is key to understanding the pathophysiological mechanisms of movement control in Parkinson's disease (PD), as well as the function of its treatment. However, functional brain imaging with magnetic resonance (fMRI) is not feasible during gait [160]. Gait disorders seriously affect the functional state and quality of life of patients with PD. With time, about 50–70% of patients will develop gait and balance disorders and show freezing of gait (FOG) which is characterized by brief episodes of inability to step and lift their feet from the ground or by extremely short steps [161]. Deep brain

stimulation of the subthalamic nucleus (DBS-STN) has proven to be effective for bradykinesia, tremor, dystonia and gait disorder in PD [162].

The purpose of this chapter is to verify the applicability of a fNIRS to detect changes in motor cortex activity during gait in PD patients treated with bilateral DBS-STN and to explore the neuronal network involved.

8.2 Related Work

Previous fMRI/PET studies have shown many types of motor activations in healthy controls (HC subjects) and PD patients. Self-initiated (18 PD patients) finger tapping (FT) activated the left primary motor cortex (M1), the premotor cortex (PMC), the pre-supplementary motor area (SMA) and the parietal cortex (PC) [163]. Relatively decreased activities in the rostral part of the SMA and in the right dorsolateral prefrontal cortex (PFC) during sequential motor task were demonstrated when comparing 6 patients with PD with 6 HC subjects [164]. Neuronal activity is modulated by the amplitude and the frequency of the tapping [165–168]. PD patients, after Levodopa drug administration, showed significant differences in the motor cortico-striatal network (motor cortex, PMC, SMA, putamen and thalamus) and the cerebellum while using their more affected hand during FT [169]. Two PET studies [170, 171] showed movement-associated activation in the PMC, dorsal PFC and around the SMA (ipsilateral to stimulation and contralateral to movement) during DBS-STN.

A series of NIRS neuroimaging experiments for detecting the characteristics of brainwaves under different conditions have appeared in the past and during recent years. A wearable, multi-channel fNIRS imaging system was presented and tested in 8 HC subjects while riding bicycles outdoors [172]. In HC subjects, the evoked activity of simple hand movement increased linearly in the SM1 and SMA in images from a NIRS [173, 174]. A recent pilot study [175] showed increased activity in motor-associated cortical activity following unilateral GPi DBS surgery measured by a fNIRS (ON vs. OFF condition in 6 PD patients). Cortical activity was relatively increased in the contralateral primary motor area and the prefrontal cortex. In another study, high frequency (120 Hz) GPi stimulation consistently increased oxygenated hemoglobin (oxyHb) with a decrease of deoxyHb in an intensity and time dependent manner in a NIRS imaging of the frontal lobe [176]. In addition to the improved motor symptoms of patients with PD, DBS-STN may alter emotional evocation, as it was demonstrated that the STN is correlated with unique patterns of NIRS oxy-Hb changes in PFC during an emotion evocation task [177]. NIRS shows bilateral activations in the SM1, SMA and PM during walking [178, 179]. Levodopa PD ON had a higher oxyHb concentration in the frontal lobe during usual walking, as measured by 2 probes placed on the subject's forehead [180].

To our knowledge, no study has directly examined DBS-STN related

changes in cortical activity specifically during gait and FT tasks in images of a multichannel NIRS. We hypothesized the following: for PD patients, the cortex activity in the ON state for both FT and gait will be higher than in the OFF state.

8.3 Methods

8.3.1 Study Participants and Neurological Assessment

We included 9 patients with advanced PD (1F, 8M, median age: 65, interquartile range: 6.3 yrs.), chronically treated with double-sided DBS-STN with a quadripolar electrode (Medtronic DBS system, Fridley, Minnesota, USA). Participants were recruited from a randomized control study on DBS. The study was approved by the Ethics Committee of the General University Hospital in Prague and therefore performed in accordance with the ethical standards established in the 1964 Declaration of Helsinki. A written, informed consent was obtained prior to data collection. The clinical status of the patients was expressed through the unified Parkinson's disease rating scale (UPDRS), part III: clinician-scores monitored the motor evaluation. Akinesia, rigidity and tremor were assessed as subscore items of UPDRS-III. Patients were examined in two sessions after an overnight withdrawal of dopaminergic medication in the DBS-STN OFF state (UPDRS-III: 53.4 ± (SD) 11) and DBS-STN ON at 130 Hz (UPDRS-III: 29.1 ± (SD) 11.5). The order and the interval of days between examinations were randomized. A 1.5h interval was considered sufficient for the onset of full effects and to become accustomed to the frequency change. DBS electrodes were bilaterally implanted using standard stereotactic methods and incorporating intraoperative microelectrode recording. The examinations were performed at least one year after the DBS implantation.

8.3.2 NIRS Data Acquisition and Tasks Design

Optical signals are strongly attenuated when passing through biological tissue. The intensity decreases by several orders of magnitude at the distance of several centimeters. A physical model derived from the modified Lambert-Beer law was used for the purpose of determining the changes in oxyhemoglobin concentrations from raw centered signals. The following equation can be defined based on knowledge of recorded time series for 2 wavelengths and extinction coefficient values for 2 chromophores (HbO and HbR) [181]:

$$\Delta C_{HbO} = \frac{e_{HbR,\lambda_1}\frac{\Delta A_{\lambda_2}}{L_{\lambda_2}} - e_{HbR,\lambda_2}\frac{\Delta A_{\lambda_1}}{L_{\lambda_1}}}{e_{HbR,\lambda_1}e_{HbO,\lambda_2} - e_{HbR,\lambda_2}e_{HbO,\lambda_1}} \tag{8.1}$$

760 nm		850 nm	
HbO	HbR	HbO	HbR
1.49	3.84	2.53	1.8

Table 8.1: Values of extinction coefficients ($M^{-1}cm^{-1}$) used to calculate the time series of HbO and HbR concentrations for the NIRS device (taken from the device documentation).

C_{HbO} denotes the HbO concentration, e_i represents the extinction coefficient of the given chromophore for a particular wavelength (Table 8.1), corresponds to the raw signal and is proportional to the negative logarithm of the ratio of detected and emitted light intensity, L_i represents the mean free path length describing the most likely path of a photon towards the detector (set to 3 cm). In a similar way, the equation can be defined for the deoxyhemoglobin.

Cortical activity was acquired simultaneously in 22 channels using a portable NIRS system (NIRSport by NIRX Medizintechnik, Berlin, Germany, sampling frequency = 8.93 Hz), which consists of 7 sources and 8 detectors in a head cap. The NIRS usually incorporates lasers or light-emitting diodes as a lights source. The device emits NIR radiation at 2 wavelengths, 760 and 850 nm. Photodetectors were arranged on the scalp using the international 10-20 EEG system for positioning: F1, FC1, CP1, FC3, F2, FC2, CP2, FC4 (Fig. 8.1A). An accurate 3D neuroanatomic position is available through the coordinate atlas of the MNI standard (Montreal Neurological Institute). The NIRS cap was placed so that the source Cz was located halfway between the nasion-inion. We chose to use NIRS because it is noninvasive, compatible with implanted electrodes and has good motion tolerance for tremors.

Each task was repeated 10 times continuously in a block diagram (Fig. 8.2):

a) For the right hand FT task, each cycle consisted of 15 seconds of alternating finger motion and 15 seconds of rest. We tested finger tapping for the right hands (more severely affected right sides were observed for all patients).

b) For gait, each cycle comprised of about 12 seconds including the gait phase (starting from standing) and about a 60 seconds break, including sitting down, resting on a chair, rising from the chair and a few seconds for stabilization before the next gait cycle.

8.3.3 Finger Tapping Movement Measurement

For the purpose of objectively comparing motor changes in finger tapping, we simultaneously measured FT subtest of the UPDRS-III (item 23: the patient taps the index finger on the thumb as quickly and as extended as possible). The movement characteristics were measured by the Optitrack V120:Trio (NaturalPoint, Inc., Corvallis, USA) validated by [182]. The system measured

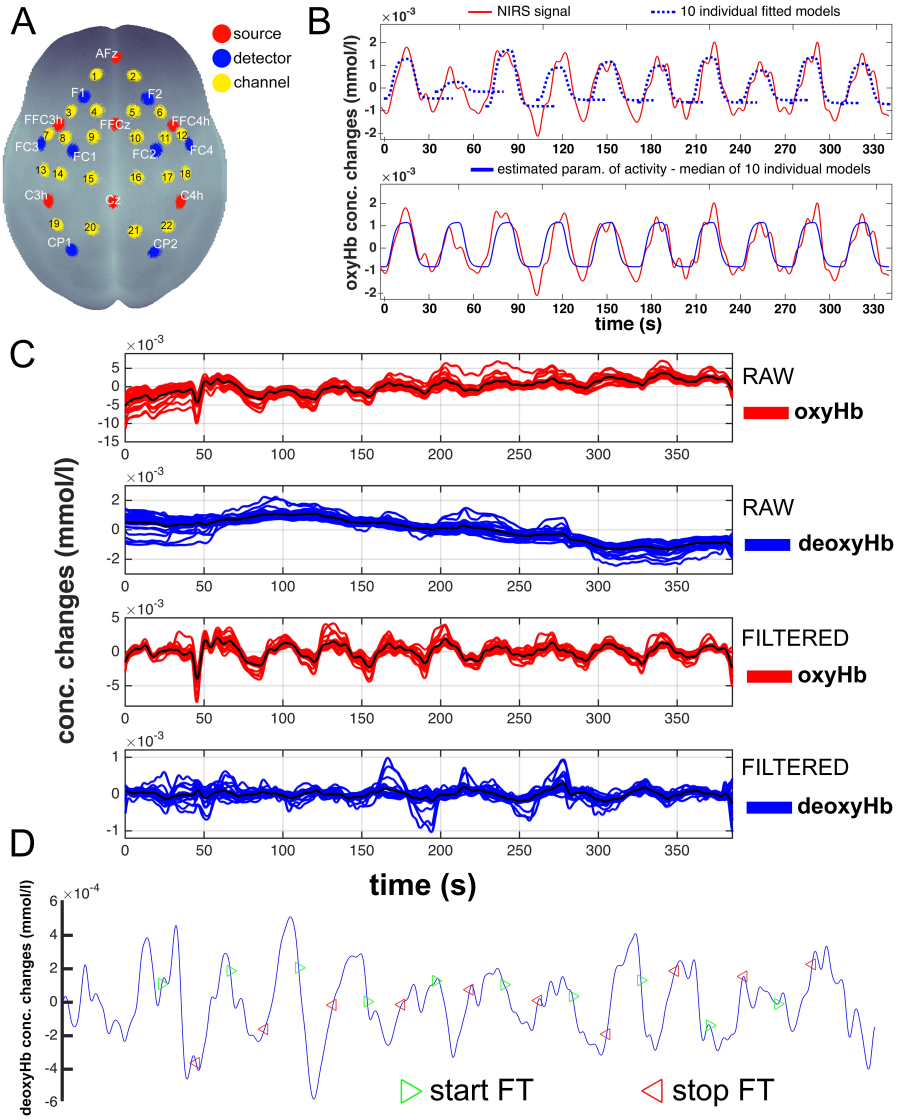

Figure 8.1: A: Scheme of the spatial distribution of detectors, sources and channels above cortical regions of the brain with respect to the EEG 10-20 system. 22 channels covered frontal cortex to parietal areas of the cortex. B: NIRS signal for one patient in the ON state (red), for 10 repetitions of finger tapping and resting periods. The top panel additionally shows the hemodynamic functions fitted to the individual repetitions (blue, dashed lines) and the lower panel shows median time course computed from 10 repetitions (blue, solid line). C: Raw finger tapping data from a single representative subject from all the channels in the DBS ON state showing oxy and deoxy responses before and after filtering. D: Deoxygenated hemoglobin signal is characterized by much lower amplitudes compared to oxyHb.

the spatial position of the markers placed on the first knuckle of the index finger and the first knuckle of the thumb. The mutual Euclidean distance of markers were used for computation of FT PD relevant movement parameters:

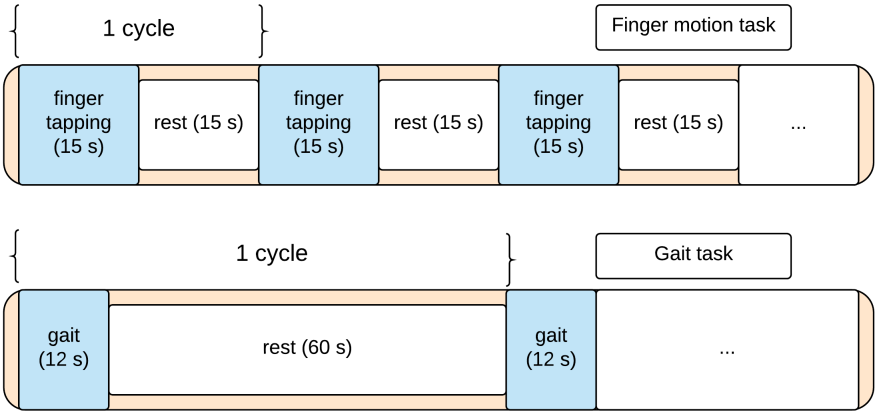

Figure 8.2: An illustrative diagram of sessions in the NIRS experiment. The NIRS experiments consisted of two sessions. Each session was a block design consisting of ten resting states alternated with ten motion task states.

a) The finger tapping frequency [Hz] (FRQ).

b) Maximum opening velocity [cm/s] (VELO) as a mean of maximum opening velocities in all tapping cycles.

c) The power of tapping (POW) as an integral of the tapping signal.

8.3.4 Walkway System Assessment

Gait was assessed using a 5.15 m long and 0.9 m wide instrumented walkway (Platinum model GAITRite®, CIRSystem Inc., Franklin, USA) placed 2.43 m from chair in the middle of the straight gait walkway. The walking trial had a length of 10 m in a straight line, with a GAITRite positioned in the middle. Processed spatio-temporal gait characteristics are: velocity (cm/s) - mean velocity of walking (distance travelled per time), cadence (steps/min), step length (cm).

8.3.5 Statistical Analysis and Signal Processing

Raw data was processed offline using Matlab (MathWorks, Natick, Massachusetts, USA). Changes in (de)oxyHb concentrations were calculated from a demeaned NIRS signal using a modified Beer-Lambert transformation (1). The signals were filtered in a range from 0.015 to 0.3 Hz to attenuate global drifts and extracerebellar artifacts (Fig. 8.1C) generated by respiration and cardiac variation (3rd order Butterworth band-pass filter) [183, 184]. We have adapted the standard version of the General Linear Model to estimate neuronal activity, i.e. the amplitude of the BOLD signal for each channel—each cycle was separately fitted with a physiologically based Boynton Hemodynamic Response Function in the sense of least mean squares to minimize difference

between obtained response and desired model-based response (Fig. 8.1B). Finally, the median amplitude from the 10 individual cycles was calculated and input for statistical comparison between DBS-STN states ON and OFF (2-sided Wilcoxon paired test; uncorrected). An alpha of 0.05 was used as the cutoff for significance. The NIRS signal (typically μmol/l) corresponded to the area under curve (AUC) of the HbO/HbR concentration variation during the duration of the movement (Fig. 8.1C, 8.1D). The total number of automatically processed recordings was nearly 1600 (oxyHb, deoxyHb, 22 channels, 2 conditions, 9 patients, 2 tasks). When applicable, Cohen's d analyses were done in order to estimate the effect size (via effsize package in R programming language). The magnitude was assessed using the thresholds, i.e. $|d| < 0.2$ = negligible, $|d| < 0.5$ = small, $|d| < 0.8$ = medium, and otherwise large.

The most commonly used method for determining signal activity and for examining the relationships between variables in neuroscience has become a general linear model (2), in a better interpretable case (3).

$$Y = X \cdot \beta + \varepsilon \tag{8.2}$$

$$NIRSsignal = design \cdot \beta + error \tag{8.3}$$

The simplest GLM design matrix consists of 2 explanatory variables: a variable containing the only ones for the computation of the absolute member and a variable for estimating the size of the experiment factor (i.e. motor task). It is determined by the value 1 in the case of a stimulus and the value 0 in its absence. The modification of the box-car course closer to the known physiological BOLD nature of the response can be reached by convolution with Boynton HRF. Estimation of parameter values $\hat{\beta}$ is calculated using the least squares method:

$$\hat{\beta} = (X^T X)^{-1} X^T Y \tag{8.4}$$

The proposed median method leads to robust estimates for irregular signals, which are often obtained from patients with advanced progressive pathophysiology. In such cases, the estimate behaves empirically better and considers the time change of the parameter $\hat{\beta}$ values during a block experiment.

8.3.6 NIRS Brain Mapping

The NIRS Brain Mapping tool was implemented on top of Matlab based on the knowledge of accurate neuroanatomical standardized MNI coordinates for

Brain area	**EEG 10-20** **NIRS channel**
intermediate frontal	AFz-F1, AFz-F2, FFC3h-F1, FFC4h-F2 Ch1, Ch2, Ch3, Ch6
intermediate, agranular frontal	FFCz-F1, FFCz-F2 Ch4, Ch5
premotor cortex, supplementary motor cortex	FFC3h-FC3, FFC3h-FC1, FFCz-FC1, FFCz-FC2, FFC4h-FC4 Ch7, Ch8, Ch9, Ch10, Ch11, Ch12
primary somatosensory cortex, primary motor cortex	C3h-FC3, C4h-FC4 Ch13, Ch18
primary motor cortex	C3h-FC1, Cz-FC1, Cz-FC2, C4h-FC2 Ch14, Ch15, Ch16, Ch17
primary somatosensory cortex, somatosensory association cortex	C3h-CP1, C4h-CP2 Ch19, Ch22
preparietal	Cz-CP1, Cz-CP2 Ch20, Ch21

Table 8.2: Result of expertise mapping of NIRS channels to anatomical brain areas.

individual channels. The NIRS Brain Mapping tool is based on triangulation-cubic interpolation of estimated activity values (Z) in channels according to MNI (X, Y) coordinates and fits a hypersurface of the form (Fig. 8.3):

$$v = f(X, Y, Z) \tag{8.5}$$

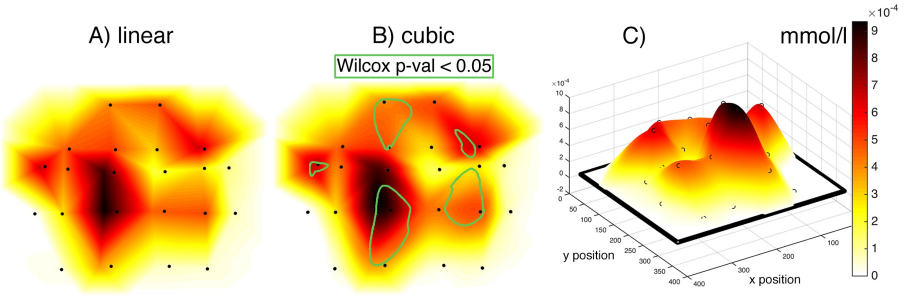

Figure 8.3: Comparison of linear (A) and cubic (B) interpolation. (C) 3D view of the interpolation curve that passes through all MNI coordinates with median activity for an average of 9 patients DBS-STN ON–OFF differential map. Input grid in the form of a matrix has 375 rows and 329 columns. Blackpoints represent the position of individual channels. Linear and cubic give a comparable result of interpolation. Points define a network between which activity is interpolated. The griddata() Matlab function has been used, which interpolates with a triple grid resolution. The color scale represents activity intensity. The 2D map is created by displaying the scalp into 2D space, which thus causes a distortion of the position of some optodes. A) linear interpolation leads to a sharper map compared to cubic. B) contains the representation of statistically significant areas according to the Wilcoxon paired test.

Anatomical mapping of NIRS channels to EEG 10-20 positions was evaluated by an expert and can be performed according to Table 8.2.

8.4 Results

NIRS examinations have been shown to be appropriate, safe and clinically feasible. Complications in using the system to measure FT and gait were not observed. The wearable multi-channel NIRS system ran without technical problems for all nine subjects throughout all experimental conditions.

8.4.1 Increased Cortical Activity during FT in DBS-STN state ON

The measurement area covered the bilateral cortex, since we expected the left hemisphere to be activated by right hand FT. Investigation of spectroscopic parameters in 9 patients during FT revealed differences of the oxyHb NIRS signal in different cortical regions in different conditions (ON vs. OFF). For both conditions, the average activity in all channels increased in comparison to the resting phase ($p < 0.01$). Interpolated maps (Fig. 8.4A) show a qualitatively similar pattern of activity in the ON and OFF state. Nevertheless, the differential map (ON–OFF) pinpoints to statistically significant activated areas associated with planning and execution of movements (Fig. 8.5). The DBS-STN stimulators influenced activity on both sides but were more pronounced on the contralateral side of the used hand. The correlations between spectroscopic and clinical parameters were not significant. We have not observed any significant changes in deoxyHb responses.

Regarding UPDRS-III ($p = 0.0091$; Fig. 8.6) scores, statistical analyses indicated significant effects of DBS-STN (Fig. 8.7): AKINESIA ON versus OFF ($p = 0.015$), as well as the RIGIDITY ($p = 0.0084$). These results show that STN DBS helped to reduce motor symptoms in participants.

Regarding motion capture analysis (higher value = better movement), concordant results were obtained (Fig. 8.8). The change in stimulation mainly affected the signal power ($p < 0.01$) and opening velocity ($p < 0.01$), despite finger tapping frequency ($p = 0.076$). The correlation between velocity and power was significant and strongly positive (Spearman's rho = 0.88, $p = 0.003$).

Overall, the significant increases in the oxyHb ON state as compared to the OFF state of the stimulator were found in the following channels (Fig. 8.4A, Fig. 8.5):

a) The contralateral intermediate frontal area (AFz-F1, Ch1): Cohen's effect size value ($d = 0.84$) suggests a high practical significance;

b) The contralateral PMC and Supplementary Motor Cortex (SMC) (FFC3h-FC3, Ch7): Cohen's effect size value ($d = 0.77$) suggests a medium to high practical significance;

c) The contralateral M1 (Cz-FC1, Ch15): Cohen's effect size value ($d = 0.81$) suggests a high practical significance;

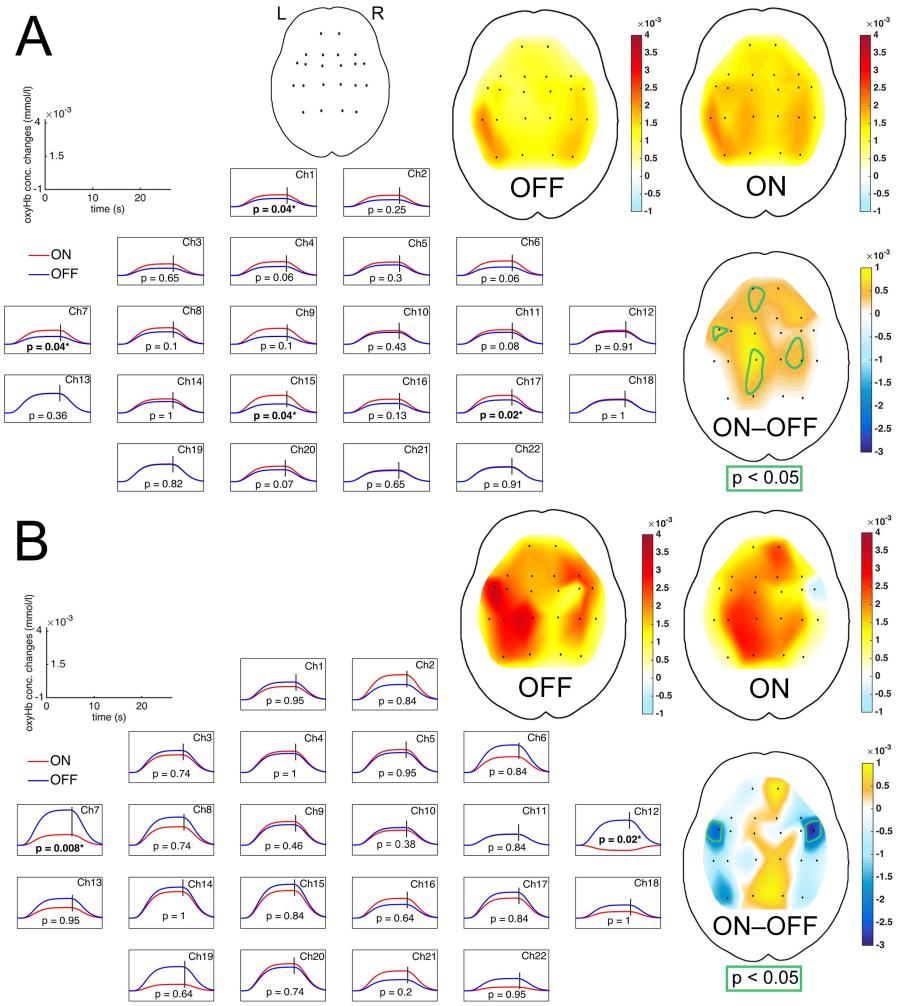

Figure 8.4: NIRS brain mapping: Map of average concentration changes (oxygenated hemoglobin) in DBS ON vs. OFF state. The black lines indicate the time of maximum amplitude of hemoglobin concentration. A: Right hand finger tapping. B: Gait. The difference between DBS OFF and ON is caused by a decrease in channel 7 and 12 during gait, and the ON map appears to be more focused (centered) above the vertex.

d) The ipsilateral PMC and M1 (C4h-FC2, Ch17): Cohen's effect size value (d = 0.76) suggests a medium to high practical significance;

It is also to be noted that, on an individual level, the majority of participants followed all the trends mentioned above.

8.4.2 More Localized Activity During Gait in DBS-STN state ON

Gait recordings from 8 patients were investigated. The other (one remaining patient) contained 3 short-term FOG and was excluded from analysis after

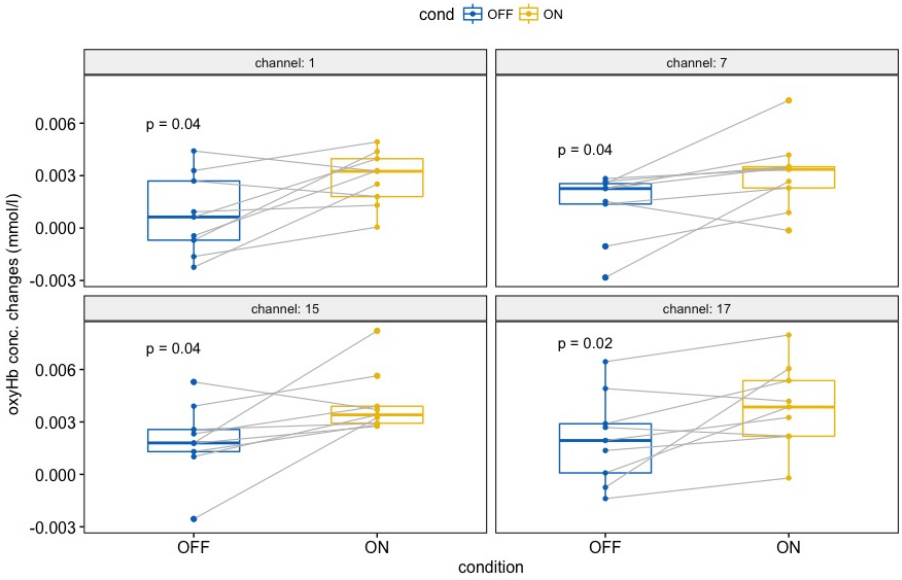

Figure 8.5: Paired box plots with significant FT channels.

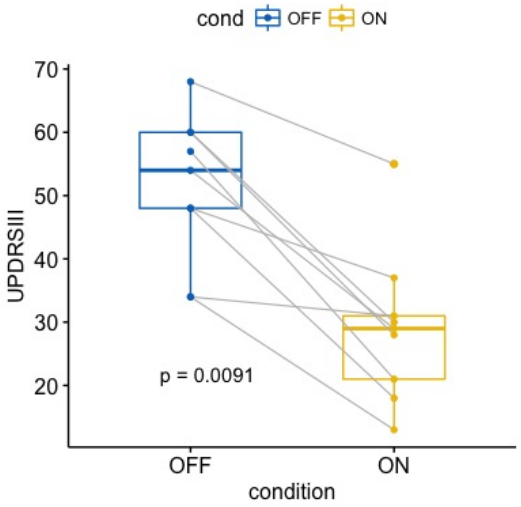

Figure 8.6: Paired box plot with change in UPDRS-III. DBS-STN led to the improvement in the overall clinical status.

video assessment. We did not register any quantitative signs of the effects of the short-term FOG on gait in the NIRS image.

The average DBS-STN ON state oxyHb activity was more localized towards the longitudinal fissure compared to the OFF state (Fig. 8.4B). For both oxyHb conditions, the average activity against the resting phase was elevated in almost all channels ($p < 0.01$) (with the exception of the Ch12 in the ON condition). The significant highest activity in the OFF state was associated with the PMC and the SMC on both sides (FFC3h-FC3, FFC4h-FC4; $p < 0.05$). No differences in other regions were found. We observed twice the

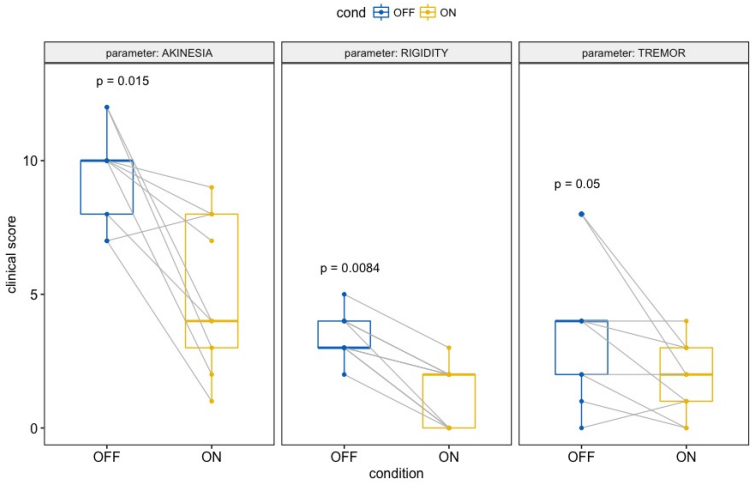

Figure 8.7: Paired box plots with changes in UPDRS-III subscores.

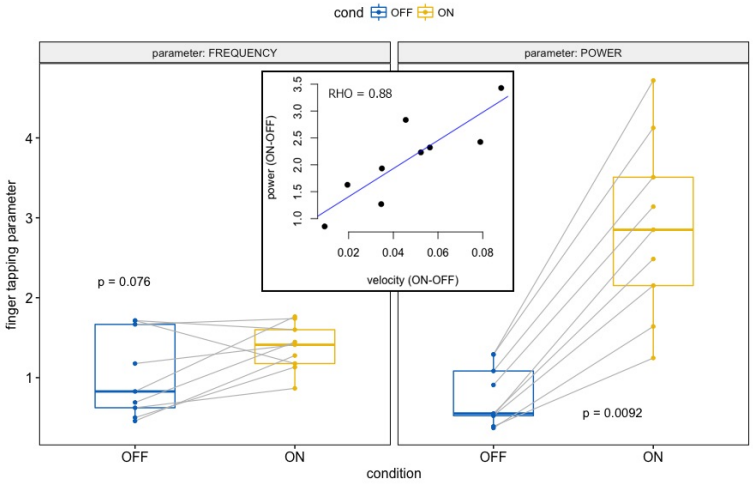

Figure 8.8: Paired box plots capturing results from the motion capture camera. DBS-STN led to an improvement in finger movement characteristics. In addition, in the nested graph, finger opening velocity correlates with signal power. The change of frequency was not significant.

activity values during gait in comparison with FT. Responses for deoxyHb were not significantly affected by DBS switched on.

The GAITRite system in the ON state vs. the OFF (Fig. 8.9) produced a longer left-sided step length (71.9 cm ± 7.0 vs. 66.2 cm ± 9.7, p = 0.008) and right-sided step length (72.4 cm ± 6.2 vs. 66.1 cm ± 10.3, p = 0.008). The change in cadence was not significant (122.7 steps/min ± 10.4 vs. 121.6 steps/min ± 12.7, p = 0.55), as well as no change in normalized velocity (1.59 ± 0.28 vs. 1.45 ± 0.35, p = 0.08).

Overall, a statistical difference in the oxyHb ON state as compared to the OFF state of the stimulator was found in the following (Fig. 8.4B, Fig. 8.10):

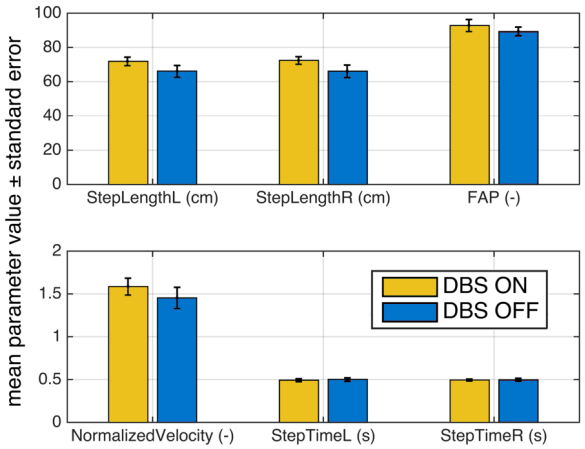

Figure 8.9: GAITRite parameters. FAP: Functional Ambulation Performance score; L: left side; R: right side.

a) The left PMC and the SMC (FFC3h-FC3, Ch7): Cohen's effect size value (d = 0.70) suggests a medium to high practical significance;

b) The right PMC and the SMC (FFC4h-FC4, Ch12): Cohen's effect size value (d = 0.62) suggests a medium to high practical significance;

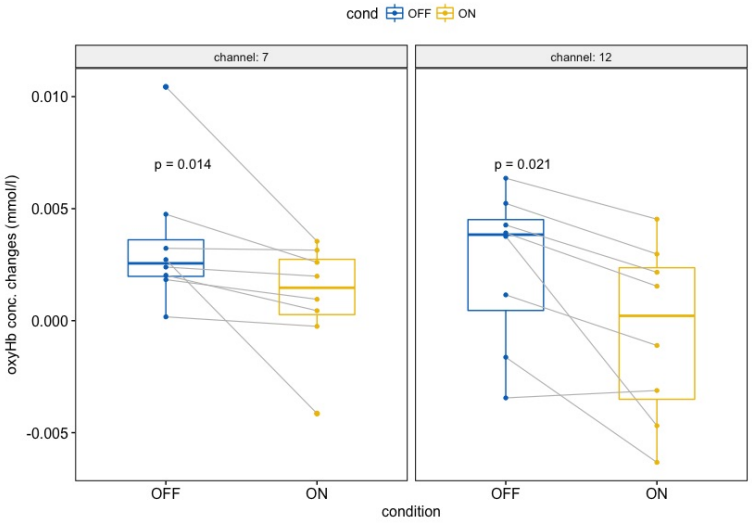

Figure 8.10: Paired box plots with significant gait channels.

8.5 Discussion

We propose a measurement protocol for capturing motor cortex activity patterns in a wearable, multi-channel fNIRS imaging system in patients with

PD. We show how the required measurement protocol can be implemented with simultaneous measurements of finger movements with a motion capture camera and the GAITRite walkway system. These parallel measurements allow for the alignment of neuroimaging and biomechanical methods. We investigated cortical activity changes in both hemispheres of patients with PD that were treated with bilateral DBS-STN. As expected, our results show an increase in NIRS activity against the resting state during FT and gait.

The primary finding in the domain is the new way to measure the change in cortical activity induced by the subthalamic DBS, where left-sided motor and sensorimotor regions were more activated during tapping with the right upper limb. We do not know whether this is a sign of normalization or compensation, because we did not measure healthy controls. However, we feel that our discovery—namely, that these changes took place in the motor region of the contralateral hemisphere—is quite significant. We can exclude that our results are driven by global extra-cerebral noise because only very few channels but not most of them show significant differences. Furthermore, these channels are located in expected regions of the somatomotoric cortex and were filtered by the Butterworth band-pass filter [183, 184]. We have to further mention that we present the contrast between two states (DBS-ON and DBS-OFF). Under the assumption of equal global noise between these two states, global hemodynamics were thereby subtracted.

A very perspective method proposed to separate the global and local components in functional near-infrared spectroscopy signals is the principal component spatial filtering [185]. Nevertheless, as it is not yet fully integrated into the standard work flow for NIRS analysis and the algorithm might exclude small portions of actual neuronal activity, i.e. it might be too conservative. The effect of this method can be the topic of further research, specifically with focus on the effect of the spatial filtering on gait.

Our second significant finding is the change in cortical activity during gait, when it was demonstrated paradoxically with the opposite phenomenon, such as a decrease in the ON activity in the lateral cortex, which can be seen as a focusing of previously diffusive activity over a region in the vertex that is known to somatotopically correspond to the lower limbs. We have found that DBS-STN has a varied influence on the activity of the motor cortex. Higher motor cortex activity shown in the DBS OFF state compared to ON state may reflect an impairment of gait control in patients with PD. We emphasize the main advantage over PET and a fMRI in that is real, not imagined, gait. The seemingly contradictory change, the decrease in oxygenation, does not necessarily mean a different pathophysiological mechanism as opposed to its increase in finger tapping. This can be a plastical change of the cortex associated with consolidating activity into a smaller area. The higher activity values for the gait condition are not surprising though gait implies much more movement than just finger tapping. Nevertheless, deoxyhemoglobin did not show any significant effects. It is debated that deoxygenated hemoglobin is more stable in comparison to oxygenated hemoglobin but also has much

lower amplitudes. E.g. a study by [183] on classification accuracy of finger tapping (right vs left) showed equal results for both chromophores (71.1% and 73.3%). We therefore rely on oxygenated hemoglobin dynamics. The study [175] accurately shows the status of pre and post DBS-GPi and the differences were also observed only using oxyHb signals. Very low amplitude deoxyHb signals remain unaffected across the entire measured cortex.

DBS-STN caused higher level of the dopamine in the brain, allowing higher activity in the motion tasks (number of finger tapps or change in cadency etc.). Subsequently, higher performance of the movement was reflected in increased NIRS activity. We did not control for changes in FT or gait kinematics of DBS-ON versus DBS-OFF. Thus, we cannot rule out the influence of these factors on obtained NIRS images. These factors were generally different between neuromodulation conditions and thus, by themselves, can explain differences in oxyHb between conditions. For this reason, we cannot confirm that higher NIRS activity were due to higher movement activity or higher dopamine levels.

We showed that DBS-STN alters contralateral cortical hemodynamics during a simple FT motor task. Our results of contralateral activation during FT confirmed and outperformed earlier findings [175] in a smaller sample with 6 patients, in terms their results were not considered statistically significant and involved GPi stimulation solely. Moreover, our FT results are consistent with previous fMRI/PET/NIRS studies. Our data shows a relative increase in activity in the motor areas going along with UPDRS-III clinical improvement as shown by changes in oxyHb levels for FT task. In other words, we observed a significant reduction in clinical UPDRS-III score between ON vs OFF (Fig. 8.6) while NIRS activity increased with DBS ON (Fig. 8.5).

Assessments of brain activity during complex tasks, like gait, are unsuited for both fMRI and PET, and can only be investigated with motor imagery [186]. In a previous NIRS study in healthy individuals, gait led to increased activity primarily in the prefrontal and supplementary motor area [187]. Currently, the measurement of NIRS during gait in patients with PD takes place with a small 2-probe system that captures frontal areas. In comparison with Maidan et al., where patients were examined during complex walking for 30 seconds in the ON state, we provide information about changes in oxyHb concentrations during gait for both conditions (DBS-STN ON and OFF), as measured in 22 channels covering the frontal, central and parietal cortical areas.

There are many relevant available packages, tools and libraries that can easily be integrated into the work of biomedical software programmers. They are usually downloadable via GitHub. The following list of tools for NIRS time series analysis and fMRI brain mapping is worth mentioning: NFRI toolbox (`jichi.ac.jp/brainlab/tools.html`), xTopo (`www.alivelearn.net/?p=785`), AFNI (`afni.nimh.nih.gov`), Nitime (`nipy.org/nitime`), NIfTI (`nifti.nimh.nih.gov`) and Nilearn (`nilearn.github.io`). The advantage of the proposed method over the available implementations is easy to under-

stand; a clear algorithm of the method. Also, easy script scalability. The use of available tools often leads users to access a black box, while self-realization helps deeper understanding of the analysis procedures.

Despite promising results, this study had some limitations that must be taken into consideration when interpreting the findings of this study. First, this investigation was conducted with a small number of participants (nine PD patients). Generalization of these results must, therefore, be viewed with caution and the large inter- and intra-variability in movement disorders. The primary reason of this poor recruitment was that a large proportion of the patients were excluded because they did not meet the inclusion criteria for appropriate documentation and all the measurements. Second, more patients should be recruited to confirm the obtained results in future studies, but it is challenging both in terms of measurement and DBS implantation. In addition, a larger population could also facilitate a more in-depth investigation of correlations with clinical status and motion capture systems. Regarding uncorrected results—the Bonferroni correction using the classical interpolation is too conservative [188] and would suppress all results as non-significant in this study—a correction is generally needed for mutually independent channels. In contrast, the channels in our study are spatially dependent and interacting on overlapping areas. As part of the publicly-available NIRS processing toolboxes, the uncorrected curation is used by default, e.g. in FC-NIRS [189], NIRS-SPM [188], and even in other NIRS studies with multiple subjects [190, 191].

8.6 Conclusion

At the macro-level, a recent technique, the functional near infrared spectroscopy, is used to extract the brain cortex activity. The toolbox is able to map the NIRS cortex activity at many locations of the brain. Moreover, a new median method for estimation of signal activity is suggested to measure hemoglobin changes.

This is the first pilot study describing brain activity patterns obtained with multichannel neuroimaging using NIRS during gait in patients with PD. We found that DBS-STN performed during simple FT motor tasks led to an increase in the activity of the contralateral motor cortex areas. DBS ON state decreased activity more in lateralized areas but increased activity near the longitudinal fissure during gait. Our study demonstrates the utility of NIRS in detecting functional changes of the motor cortex in patients with PD and indicates its future use for applications that are not suited for PET and fMRI. Our findings of altered motor cortex activity during finger tapping task and gait contributes to our understanding of the pathophysiological mechanisms of movement control in PD and the function of DBS-STN stimulators. In general terms, the present study demonstrates the potential utility of the NIRS method in detecting functional changes of the brain during gait in patients with PD and other movement disorders.

Part IV

Summary and Perspectives

Chapter 9

Thesis Achievements

To further highlight the relevance and future application of the recently developed workflows, I listed below a summary of the relevant outcomes of this thesis:

- The spike detection and sorting pipeline has been validated on a large set of real neuronal spiking data (TiN and BDD-MEA) and it may be a potential therapeutic marker strategy for dystonia.
- My CNN solution works by turning a microelectrode signal processing problem into a visual problem. The MERs are fed into a deep learning AI program that identifies and classifies the images, much like the AI used in self-driving cars to identify stop signs and lane markers. It first decides if an artifact is present in the MER, and if so, what type of artifact it is.
- In addition to the extraction of basic time series parameters (frequency, change-point detection) and their statistical analysis in order to detect artifacts, I carried out more advanced time series analysis of the recorded signals (the novel MER signal representation with CWT + CNN).
- NeuroEDA Exploratory Tool
  - Interactive and dynamic.
  - Easily quantifies and compares trends and relationships for heterogeneous biomedical data.
  - Flexibility across datasets.
  - A software package for standardized and reproducible data analysis.
- A methodology that permits to simultaneously record the NIRS imaging of the brain, fingers, and gait, and to carry out multimodal analysis of these recordings. This novel methodological combination is particularly suited for advancing the differential diagnostics of PD. Max Planck Institute for Human Cognitive and Brain Sciences in Leipzig, Germany, has longstanding collaboration with our department on analysis of functional MRI. This institution assisted in design of the fNIRS.

- We developed and published algorithms and applications, which utilise motion capture camera systems (MOCAP) and accelerometric systems to analyse the position and movements of different parts of the human body [182].

I started my PhD in 2016. In the first authored publications (Appendix B), I participated in a majority of the designs of experiments, I performed all the data science experiments as well as wrote the first drafts. Subsequent drafts were edited by a subset of co-authors and submitted after approval from all authors.

Beyond the main outputs of my doctoral studies, I worked on other advanced tasks in neuroinformatics. I have experience with the analysis of speech and voice in basal ganglia disorders [192]. Motor speech disorder is a common clinical manifestation occurring in patients with parkinsonism as well as in other basal ganglia disorders including dystonia. I also studied repeatability and prediction bands of turn signals in patients with PD [193]. Nowadays, turn analyses utilizing inertial measurement units (IMU) have expanded. We demonstrated the methods for estimating prediction bands, namely the Gaussian point-by-point and bootstrap method.

Within research and development in technological companies, I completed an IBM internship in the position of Cognitive IoT Developer and Consultant in 2017. I have recently started working in the field of deep learning in genomics [194].

9.1 Community Recognition and Awards

- Reviewer of ČSN EN IEC 80601-2-71: Particular requirements for the basic safety and essential performance of functional near-infrared spectroscopy (NIRS) equipment. *Expert review.*
- Co-author of utility model for tremor measurement and analysis in patients with nervous system diseases [195].
- Josef Hlávka Award in 2019, for the best students, who have proved their exceptional capabilities and creative thinking in their branch of science.
- Stanislav Hanzl Award for CTU students in 2019.
- IEEE Excellent Paper Award at the IEEE Conference Healthcom 2018.
- 1st place in the competition for the best publication and contribution at the Summer School of Mathematical Biology, Masaryk University in Brno.

9.2 Grants

- AZV Grant no. 16-28119a, Analysis of movement disorders for the study of extrapyramidal diseases mechanism using motion capture camera systems.
- GAČR 17-15319S, Diamond based microelectrode arrays for dual mode neural recording.
- SGS17/114/OHK4/1T/17, Processing and analysis of heterogeneous neuroinformatics data, Grant Agency of the Czech Technical University in Prague. *Principal investigator.*
- SGS18/102/OHK4/1T/17, Application of data mining techniques to heterogeneous biomedical sources, Grant Agency of the Czech Technical University in Prague. *Principal investigator.*
- SGS19/090/OHK4/1T/17, Application of deep learning approach for classification of heterogenous biomedical data, Grant Agency of the Czech Technical University in Prague. *Principal investigator.*
- RPAPS 2017 FBME CTU, The innovation of existing exercises and support of the lectures in the Bioinformatics class. *Principal investigator.*

9.3 Future Work

The focus will be on the extraction of low-dimensional temporal patterns in high-dimensional spiking and local field potentials datasets in motor and working memory tasks, and the development of new tools for causal inference (e.g. Granger-causality in fNIRS imaging). I would like to explore development and application of novel and existing deep generative models (e.g. GANs, VAEs) to explain the high-dimensional structure and time course of neural population activity.

Part V

List of References

Bibliography

[1] PTÁČEK, Radek and Petr BARTŮNĚK. *Etické problémy medicíny na prahu 21. století.* Praha: Grada, 2014. Edice celoživotního vzdělávání ČLK. ISBN 978-80-247-5471-0.

[2] KREMLÁČEK, Jan. *Event related potentials: principles and practice: Educational Course BME.* Praha, 2018. Available at: https://guarant.topinfo.cz/iupesm2018/en/programme-in-details

[3] KRUPICKA, Radim, Zoltan SZABO, Slavka VITECKOVA and Evzen RUZICKA. Motion Capture System for Finger Movement Measurement in Parkinson Disease. *Radioengineering.* Společnost pro radioelektronické inženýrství, 2014, **23**(2), 659-664. ISSN 1210-2512. Available at: http://hdl.handle.net/11012/36464

[4] REDLICH, Ronny, Nils OPEL, Dominik GROTEGERD, et al. Prediction of Individual Response to Electroconvulsive Therapy via Machine Learning on Structural Magnetic Resonance Imaging Data. *JAMA Psychiatry.* 2016, **73**(6). DOI: 10.1001/jamapsychiatry.2016.0316. ISSN 2168-622X.

[5] IBM's Watson - Best Doctor In The World? In: *WORLDHEALTH.NET* [online]. Chicago: worldhealth.net, 2017 [cit. 2019-12-14]. Available at: https://worldhealth.net/news/ibm-watson-supercomputer-best-doctor-world/

[6] The Emerging Influence of Digital Biomarkers on Healthcare. In: *Rock Health* [online]. San Francisco: Rock Health, 2018 [cit. 2019-12-15]. Available at: https://rockhealth.com/reports/the-emerging-influence-of-digital-biomarkers-on-healthcare/

[7] STRIMBU, Kyle and Jorge A TAVEL. What are biomarkers? *Current Opinion in HIV and AIDS.* 2010, **5**(6), 463-466. DOI: 10.1097/COH.0b013e32833ed177. ISSN 1746-630X. Available at: https://insights.ovid.com/crossref?an=01222929-201011000-00003

[8] The Digital Health Hype Cycle 2020. In: *Healthcare.digital* [online]. USA: www.healthcare.digital, 2020 [cit. 2020-03-19]. Available at: https://www.healthcare.digital/single-post/2020/01/29/Digital-Health-Hype-Cycle-2020

[9] HODGKIN, A. L. and A. F. HUXLEY. A quantitative description of membrane current and its application to conduction and excitation in nerve. *The Journal of Physiology.* 1952, **117**(4), 500-544. DOI: 10.1113/jphysiol.1952.sp004764. ISSN 0022-3751. Available at: https://onlinelibrary.wiley.com/doi/abs/10.1113/jphysiol.1952.sp004764

[10] REES, Christopher L., Charise M. WHITE and Giorgio A. ASCOLI. Neurochemical Markers in the Mammalian Brain: Structure, Roles in Synaptic Communication, and Pharmacological Relevance. *Current Medicinal Chemistry.* 2017, **24**(28). DOI: 10.2174/0929867324666170414163506. ISSN 09298673. Available at: http://www.eurekaselect.com/151628/article

[11] How Neurons Communicate. In: *OpenStacks CNX* [online]. Rice University, 2019 [cit. 2020-01-31]. Available at: `https://cnx.org/contents/GFy_h8cu@9.87:cs_Pb-GW@5/How-Neurons-Communicate` post.aspx?PostID=476

[12] GRAY, Charles M., Pedro E. MALDONADO, Mathew WILSON and Bruce MCNAUGHTON. Tetrodes markedly improve the reliability and yield of multiple single-unit isolation from multi-unit recordings in cat striate cortex. *Journal of Neuroscience Methods.* 1995, **63**(1-2), 43-54. DOI: 10.1016/0165-0270(95)00085-2. ISSN 01650270. Available at: https://linkinghub.elsevier.com/retrieve/pii/0165027095000852

[13] BUZSÁKI, György, Costas A. ANASTASSIOU and Christof KOCH. The origin of extracellular fields and currents — EEG, ECoG, LFP and spikes. *Nature Reviews Neuroscience.* 2012, **13**(6), 407-420. DOI: 10.1038/nrn3241. ISSN 1471-003X. Available at: http://www.nature.com/articles/nrn3241

[14] FRACKOWIAK, Richard S. Human brain function. San Diego: Academic Press, c1997. ISBN 0122648404.

[15] ANEMA, Helen A. and H. Chris DIJKERMAN. Motor and Kinesthetic Imagery. *Multisensory Imagery.* New York, NY: Springer New York, 2013, 2013-12-3, 93-113. DOI: `10.1007/978-1-4614-5879-1_6`. ISBN 978-1-4614-5878-4. Available at: `http://link.springer.com/10.1007/978-1-4614-5879-1_6`

[16] DRUGA, Rastislav, Miloš GRIM and Petr DUBOVÝ. Anatomie centrálního nervového systému. 1. ed. Praha: Galén, c2011. ISBN 9788072627066.

[17] WICHMANN, T. and J.O. DOSTROVSKY. Pathological basal ganglia activity in movement disorders. *Neuroscience.* 2011, **198**, 232-244. DOI: 10.1016/j.neuroscience.2011.06.048. ISSN 03064522. Available at: https://linkinghub.elsevier.com/retrieve/pii/S0306452211007329

[18] HASHEMIYOON, Rowshanak, Jens KUHN and Veerle VISSER-VANDEWALLE. Putting the Pieces Together in Gilles de la Tourette Syndrome: Exploring the Link Between Clinical Observations and the Biological Basis of Dysfunction. *Brain Topography.* 2017, **30**(1), 3-29. DOI: 10.1007/s10548-016-0525-z. ISSN 0896-0267. Available at: http://link.springer.com/10.1007/s10548-016-0525-z

[19] VITEK, Jerrold L., Vijay CHOCKKAN, Jian-Yu ZHANG, et al. Neuronal activity in the basal ganglia in patients with generalized dystonia and hemiballismus. *Annals of Neurology.* 1991, **46**(1), 22-35.

[20] VITEK, Jerrold L. Pathophysiology of dystonia: A neuronal model. *Movement Disorders.* 2002, **17**(S3), S49-S62. DOI: 10.1002/mds.10142. ISSN 0885-3185. Available at: http://doi.wiley.com/10.1002/mds.10142

[21] SCHROLL, Henning and Fred H. HAMKER. Computational models of basal-ganglia pathway functions: focus on functional neuroanatomy. *Frontiers in Systems Neuroscience.* 2013, **7**. DOI: 10.3389/fnsys.2013.00122. ISSN 1662-5137. Available at: http://journal.frontiersin.org/article/10.3389/fnsys.2013.00122/abstract

[22] ALBANESE, Alberto, Kailash BHATIA, Susan B. BRESSMAN, et al. Phenomenology and classification of dystonia: A consensus update. *Movement Disorders.* 2013, **28**(7), 863-873. DOI: 10.1002/mds.25475. ISSN 08853185. Available at: http://doi.wiley.com/10.1002/mds.25475

[23] O'RIORDAN, S., D. RAYMOND, T. LYNCH, R. SAUNDERS-PULLMAN, S. B. BRESSMAN, L. DALY and M. HUTCHINSON. Age at onset as a factor in determining the phenotype of primary torsion dystonia. *Neurology.* 2004, **63**(8), 1423-1426. DOI: 10.1212/01.WNL.0000142035.26034.C2. ISSN 0028-3878. Available at: http://www.neurology.org/cgi/doi/10.1212/01.WNL.0000142035.26034.C2

[24] MCINERNEY-LEO, A.M., J.E. HARRIS, P.J. LEO, et al. Whole exome sequencing is an efficient, sensitive and specific method for determining the genetic cause of short-rib thoracic dystrophies. *Clinical Genetics.* 2015, **88**(6), 550-557. DOI: 10.1111/cge.12550. ISSN 00099163. Available at: http://doi.wiley.com/10.1111/cge.12550

[25] POEWE, Werner, Klaus SEPPI, Caroline M. TANNER, Glenda M. HALLIDAY, Patrik BRUNDIN, Jens VOLKMANN, Anette-Eleonore SCHRAG and Anthony E. LANG. Parkinson disease. *Nature Reviews Disease Primers.* 2017, **3**(1). DOI: 10.1038/nrdp.2017.13. ISSN 2056-676X. Available at: http://www.nature.com/articles/nrdp201713

[26] DUFFY, Joseph R. *Motor speech disorders: substrates, differential diagnosis, and management.* Third edition. St. Louis, Missouri: Elsevier, [2013]. ISBN 978-032-3072-007.

[27] HUGHES, A J, S E DANIEL, L KILFORD and A J LEES. Accuracy of clinical diagnosis of idiopathic Parkinson's disease: a clinico-pathological study of 100 cases. *Journal of Neurology, Neurosurgery & Psychiatry.* 1992, **55**(3), 181-184. DOI: 10.1136/jnnp.55.3.181. ISSN 0022-3050. Available at: http://jnnp.bmj.com/cgi/doi/10.1136/jnnp.55.3.181

[28] RUSZ, Jan, Jan HLAVNIČKA, Roman ČMEJLA and Evžen RŮŽIČKA. Automatic Evaluation of Speech Rhythm Instability and Acceleration in Dysarthrias Associated with Basal Ganglia Dysfunction. *Frontiers in Bioengineering and Biotechnology.* 2015, **3**. DOI: 10.3389/fbioe.2015.00104. ISSN 2296-4185. Available at: http://journal.frontiersin.org/Article/10.3389/fbioe.2015.00104/abstract

[29] BOUTON, C. Cracking the neural code, treating paralysis and the future of bioelectronic medicine. *Journal of Internal Medicine.* 2017, **282**(1), 37-45. DOI: 10.1111/joim.12610. ISSN 0954-6820. Available at: https://onlinelibrary.wiley.com/doi/abs/10.1111/joim.12610

[30] WICHMANN, Thomas and Mahlon R. DELONG. Deep Brain Stimulation for Movement Disorders of Basal Ganglia Origin: Restoring Function or Functionality? *Neurotherapeutics.* 2016, **13**(2), 264-283. DOI: 10.1007/s13311-016-0426-6. ISSN 1933-7213. Available at: http://link.springer.com/10.1007/s13311-016-0426-6

[31] JECH, Robert. Hluboká mozková stimulace u dystonií. *Neurologie pro praxi. 2013*, **14**(5), 232-236.

[32] FEČÍKOVÁ, Anna, Robert JECH, Václav ČEJKA, et al. Benefits of pallidal stimulation in dystonia are linked to cerebellar volume and cortical inhibition. *Scientific Reports.* 2018, **8**(1). DOI: 10.1038/s41598-018-34880-z. ISSN 2045-2322. Available at: http://www.nature.com/articles/s41598-018-34880-z

[33] LEE, John Y.K., Milind DEOGAONKAR and Ali REZAI. Deep brain stimulation of globus pallidus internus for dystonia. *Parkinsonism & Related Disorders.* 2007, **13**(5), 261-265. DOI: 10.1016/j.parkreldis.2006.07.020. ISSN 13538020. Available at: https://linkinghub.elsevier.com/retrieve/pii/S1353802006002070

[34] MUKHERJEE, Siddhartha. *The laws of medicine: field notes from an uncertain science.* New York, 2015. Ted books. ISBN 14-767-8484-1.

[35] Mixed Results for Long-Term Effects of DBS on Pain in Parkinson's. In: *NeurologyToday* [online]. New York: American Academy of Neurology, 2015 [cit. 2019-12-17]. Available at:

https://journals.lww.com/neurotodayonline/blog/breakingnews/pages/post.aspx?PostID=476

[36] Medtronic deep brain stimulation software earns FDA nod. In: *FierceBiotech* [online]. San Diego: FierceBiotech, 2016 [cit. 2019-12-17]. Available at: https://www.fiercebiotech.com/medical-devices/medtronic-deep-brain-stimulation-software-earns-fda-nod

[37] CHEN, Shuo, Adam Z. WEITEMIER, Xiao ZENG, et al. Near-infrared deep brain stimulation via upconversion nanoparticle–mediated optogenetics. *Science.* 2018, **359**(6376), 679-684. DOI: 10.1126/science.aaq1144. ISSN 0036-8075. Available at: http://www.sciencemag.org/lookup/doi/10.1126/science.aaq1144

[38] BENNET, Kevin E., Jonathan R. TOMSHINE, Hoon-Ki MIN, et al. A Diamond-Based Electrode for Detection of Neurochemicals in the Human Brain. *Frontiers in Human Neuroscience.* 2016, 10. DOI: 10.3389/fnhum.2016.00102. ISSN 1662-5161. Available at: https://www.frontiersin.org/articles/10.3389/fnhum.2016.00102/full

[39] PRIORI, Alberto, Guglielmo FOFFANI, Lorenzo ROSSI and Sara MARCEGLIA. Adaptive deep brain stimulation (aDBS) controlled by local field potential oscillations. *Experimental Neurology.* 2013, 10. DOI: 10.1016/j.expneurol.2012.09.013. ISSN 00144886. Available at: https://linkinghub.elsevier.com/retrieve/pii/S0014488612003755

[40] SINGH, Manmohan, KV SHABARI GIRISHAN, Jitin BAJAJ and Kanwaljeet GARG. Deep brain stimulation for movement disorders: Surgical nuances. *Neurology India.* 2018, **66**(7). DOI: 10.4103/0028-3886.226461. ISSN 0028-3886. Available at: http://www.neurologyindia.com/text.asp?2018/66/7/122/226461

[41] GOENSE, Jozien B.M. and Nikos K. LOGOTHETIS. Neurophysiology of the BOLD fMRI Signal in Awake Monkeys. *Current Biology.* 2008, **18**(9), 631-640. DOI: 10.1016/j.cub.2008.03.054. ISSN 09609822. Available at: https://linkinghub.elsevier.com/retrieve/pii/S0960982208004429

[42] JECH, Robert. *Patofyziologické mechanismy neuromodulační léčby u dystonií: ZÁVĚREČNÁ ZPRÁVA GRANTU.* IGA MZ ČR NT12282-5. Praha: Všeobecná fakultní nemonice v Praze, 2016.

[43] RUSZ, Jan, Tereza TYKALOVÁ, Anna FEČÍKOVÁ, Daniela ŠŤASTNÁ, Dušan URGOŠÍK and Robert JECH. Dualistic effect of pallidal deep brain stimulation on motor speech disorders in dystonia. *Brain Stimulation.* 2018, **11**(4), 896-903. DOI: 10.1016/j.brs.2018.03.007. ISSN 1935861X. Available at: https://linkinghub.elsevier.com/retrieve/pii/S1935861X18300901

[44] WECKSTROM, Matti. Intracellular recording. *Scholarpedia.* 2010, **5**(8). DOI: 10.4249/scholarpedia.2224. ISSN 1941-6016.

[45] KUMAR, Jayanth, Juneeth KUMAR, Shanmukha MURALI and Ramesh BHAKTHAVATCHALU. Design and implementation of Izhikevich, Hodgkin and Huxley spiking neuron models and their comparison. *2016 International Conference on Advanced Communication Control and Computing Technologies (ICACCCT).* IEEE, 2016, 2016, , 111-116. DOI: 10.1109/ICACCCT.2016.7831611. ISBN 978-1-4673-9545-8. Available at: http://ieeexplore.ieee.org/document/7831611/

[46] NESS, Torbjørn V., Chaitanya CHINTALURI, Jan POTWOROWSKI, Szymon ŁĘSKI, Helena GŁĄBSKA, Daniel K. WÓJCIK and Gaute T. EINEVOLL. Modelling and Analysis of Electrical Potentials Recorded in Microelectrode Arrays (MEAs). *Neuroinformatics.* 2015, **13**(4), 403-426. DOI: 10.1007/s12021-015-9265-6. ISSN 1539-2791. Available at: http://link.springer.com/10.1007/s12021-015-9265-6

[47] DIPALO, Michele, Hayder AMIN, Laura LOVATO, et al. Intracellular and Extracellular Recording of Spontaneous Action Potentials in Mammalian Neurons and Cardiac Cells with 3D Plasmonic Nanoelectrodes. *Nano Letters.* 2017, **17**(6), 3932-3939. DOI: 10.1021/acs.nanolett.7b01523. ISSN 1530-6984. Available at: https://pubs.acs.org/doi/10.1021/acs.nanolett.7b01523

[48] OBEID, lyad. Comparison of Spike Detectors based on Simultaneous Intracellular and Extracellular Recordings. *2007 3rd International IEEE/EMBS Conference on Neural Engineering.* IEEE, 2007, 2007, , 410-413. DOI: 10.1109/CNE.2007.369696. ISBN 1-4244-0791-5. Available at: http://ieeexplore.ieee.org/document/4227301/

[49] KOCABICAK, Ersoy, Onur ALPTEKIN, Linda ACKERMANS, Pieter KUBBEN, Mark KUIJF, Erkan KURT, Rianne ESSELINK and Yasin TEMEL. Is there still need for microelectrode recording now the subthalamic nucleus can be well visualized with high field and ultrahigh MR imaging? *Frontiers in Integrative Neuroscience.* 2015, 9. DOI: 10.3389/fnint.2015.00046. ISSN 1662-5145. Available at: http://journal.frontiersin.org/Article/10.3389/fnint.2015.00046/abstract

[50] ABOSCH, Aviva, Lars TIMMERMANN, Sylvia BARTLEY, Hans Guido RIETKERK, Donald WHITING, Patrick J. CONNOLLY, David LANCTIN and Marwan I. HARIZ. An International Survey of Deep Brain Stimulation Procedural Steps. *Stereotactic and Functional Neurosurgery.* 2013, **91**(1), 1-11. DOI: 10.1159/000343207. ISSN 1011-6125. Available at: https://www.karger.com/Article/FullText/343207

[51] BOUR, Lo J., M. Fiorella CONTARINO, Elisabeth M. J. FONCKE, Rob M. A. DE BIE, Pepijn VAN DEN MUNCKHOF, Johannes D. SPEELMAN and P. Richard SCHUURMAN. Long-term

experience with intraoperative microrecording during DBS neurosurgery in STN and GPi. *Acta Neurochirurgica.* 2010, **152**(12), 2069-2077. DOI: 10.1007/s00701-010-0835-y. ISSN 0001-6268. Available at: http://link.springer.com/10.1007/s00701-010-0835-y

[52] HORN, Andreas, Wolf-Julian NEUMANN, Katharina DEGEN, Gerd-Helge SCHNEIDER and Andrea A. KÜHN. Toward an electrophysiological "sweet spot" for deep brain stimulation in the subthalamic nucleus. Human Brain Mapping. 2017. DOI: 10.1002/hbm.23594. ISSN 10659471. Available at: http://doi.wiley.com/10.1002/hbm.23594

[53] BOOTIN, Martin L. Deep Brain Stimulation: Overview And Update. *Journal of Clinical Monitoring and Computing.* 2006, **20**(5), 341-346. DOI: 10.1007/s10877-006-9031-2. ISSN 1387-1307. Available at: http://link.springer.com/10.1007/s10877-006-9031-2

[54] MCCLELLAND, V M, A VALENTIN, H G REY, D E LUMSDEN, M C ELZE, R SELWAY, G ALARCON and J-P LIN. Differences in globus pallidus neuronal firing rates and patterns relate to different disease biology in children with dystonia. *Neurology, Neurosurgery & Psychiatry.* 2016, **87**(9), 958-967. DOI: 10.1136/jnnp-2015-311803. ISSN 0022-3050. Available at: http://jnnp.bmj.com/lookup/doi/10.1136/jnnp-2015-311803

[55] TANG, Joyce K. H., Elena MORO, Neil MAHANT, William D. HUTCHISON, Anthony E. LANG, Andres M. LOZANO and Jonathan O. DOSTROVSKY. Neuronal Firing Rates and Patterns in the Globus Pallidus Internus of Patients With Cervical Dystonia Differ From Those With Parkinson's Disease. *Journal of Neurophysiology.* 2007, **98**(2), 720-729. DOI: 10.1152/jn.01107.2006. ISSN 0022-3077. Available at: https://www.physiology.org/doi/10.1152/jn.01107.2006

[56] TINKHAUSER, Gerd, Alek POGOSYAN, Ines DEBOVE, et al. Directional local field potentials: A tool to optimize deep brain stimulation. *Movement Disorders.* 2018, **33**(1), 159-164. DOI: 10.1002/mds.27215. ISSN 08853185. Available at: http://doi.wiley.com/10.1002/mds.27215

[57] NEUMANN, Wolf-Julian, Andreas HORN, Siobhan EWERT, Julius HUEBL, Christof BRÜCKE, Colleen SLENTZ, Gerd-Helge SCHNEIDER and Andrea A. KÜHN. A localized pallidal physiomarker in cervical dystonia. *Annals of Neurology.* 2017, **82**(6), 912-924. DOI: 10.1002/ana.25095. ISSN 0364-5134. Available at: https://onlinelibrary.wiley.com/doi/abs/10.1002/ana.25095

[58] MADANY MAMLOUK, Amir, Hannah SHARP, Kerstin M.L. MENNE, Ulrich G. HOFMANN and Thomas MARTINETZ. Unsupervised spike sorting with ICA and its evaluation using GENESIS simulations. *Neurocomputing.* 2005, 65-66, 275-282. DOI: 10.1016/j.neucom.2004.10.019. ISSN 09252312. Available at: https://linkinghub.elsevier.com/retrieve/pii/S0925231204004047

[59] WILD, Jiri, Zoltan PREKOPCSAK, Tomas SIEGER, Daniel NOVAK and Robert JECH. Performance comparison of extracellular spike sorting algorithms for single-channel recordings. *Journal of Neuroscience Methods.* 2012, **203**(2), 369-376. DOI: 10.1016/j.jneumeth.2011.10.013. ISSN 01650270. Available at: https://linkinghub.elsevier.com/retrieve/pii/S0165027011006133

[60] BAKSTEIN, Eduard. *Deep Brain Recordings in Parkinson's Disease: Processing, Analysis and Fusion with Anatomical Models.* Praha, 2016. PhD Thesis. Czech Technical University in Prague.

[61] BESTEL, Robert, Andreas W. DAUS and Christiane THIELEMANN. A novel automated spike sorting algorithm with adaptable feature extraction. *Journal of Neuroscience Methods.* 2012, **211**(1), 168-178. DOI: 10.1016/j.jneumeth.2012.08.015. ISSN 01650270. Available at: https://linkinghub.elsevier.com/retrieve/pii/S0165027012003263

[62] YANG, Kai, Haifeng WU and Yu ZENG. A Simple Deep Learning Method for Neuronal Spike Sorting. *Journal of Physics: Conference Series.* 2017, 910. DOI: 10.1088/1742-6596/910/1/012062. ISSN 1742-6588.

[63] EHRLICH, Tobin. Single Neuron Studies of the Human Brain: Probing Cognition. 2015, **74**(10), 1039-1039. DOI: 10.1097/NEN.0000000000000242. ISSN 0022-3069. Available at: https://academic.oup.com/jnen/article-lookup/doi/10.1097/NEN.0000000000000242

[64] QUIROGA, Rodrigo. Spike sorting. *Scholarpedia.* 2007, **2**(12). DOI: 10.4249/scholarpedia.3583. ISSN 1941-6016.

[65] LOPES, M. V., E. AGUIAR, E. SANTANA, E. SANTANA and A. K. BARROS. ICA feature extraction for spike sorting of single-channel records. *2013 ISSNIP Biosignals and Biorobotics Conference: Biosignals and Robotics for Better and Safer Living (BRC).* IEEE, 2013, 2013, , 1-5. DOI: 10.1109/BRC.2013.6487468. ISBN 978-1-4673-3025-1. Available at: http://ieeexplore.ieee.org/document/6487468/

[66] DIMITRIADIS, George, Joana P. NETO and Adam R. KAMPFF. T-SNE Visualization of Large-Scale Neural Recordings. *Neural Computation.* 2018, **30**(7), 1750-1774. ISSN 0899-7667

[67] LOURENS, M.A.J., H.G.E. MEIJER, M.F. CONTARINO, P. VAN DEN MUNCKHOF, P.R. SCHUURMAN, S.A. VAN GILS and L.J. BOUR. Functional neuronal activity and connectivity within the subthalamic nucleus in Parkinson's disease. *Clinical Neurophysiology.* 2013, **124**(5), 967-981. DOI: 10.1016/j.clinph.2012.10.018. ISSN 13882457. Available at: https://linkinghub.elsevier.com/retrieve/pii/S1388245712007158

[68] Comparison of Spike Sorting Software. In: *Spike Sorting Software* [online]. Github: http://simonster.github.io/, 2017 [cit. 2019-12-19]. Available at: http://simonster.github.io/SpikeSortingSoftware/

[69] MClust. In: *Free-ware spike sorting* [online]. University of Minnesota: A David Redish, 2017 [cit. 2019-12-19]. Available at: http://redishlab.neuroscience.umn.edu/MClust/MClust.html

[70] KlustaKwik spike sorting. In: *KlustaKwik spike sorting* [online]. SOURCEFORGE: SOURCEFORGE, 2014 [cit. 2019-12-19]. Available at: https://sourceforge.net/projects/klustakwik/

[71] Overview of OSort - A spike detection and sorting Matlab package. In: *Ueli Rutishauser's homepage* [online]. California Institute of Technology: https://www.urut.ch/, 2012 [cit. 2019-12-19]. Available at: https://www.urut.ch/new/serendipity/index.php?/pages/osort.html

[72] CHAURE, Fernando J., Hernan G. REY and Rodrigo QUIAN QUIROGA. A novel and fully automatic spike-sorting implementation with variable number of features. *Journal of Neurophysiology.* 2018, **120**(4), 1859-1871. DOI: 10.1152/jn.00339.2018. ISSN 0022-3077. Available at: https://www.physiology.org/doi/10.1152/jn.00339.2018

[73] KRAMER, Mark A. and Uri T. EDEN. *Case studies in neural data analysis: a guide for the practicing neuroscientist.* Cambridge, Massachusetts: The MIT Press, [2016]. ISBN 978-0262529372.

[74] TEZUKA, Taro. Multineuron spike train analysis with R-convolution linear combination kernel. *Neural Networks.* 2018, 102, 67-77. DOI: 10.1016/j.neunet.2018.02.013. ISSN 08936080. Available at: https://linkinghub.elsevier.com/retrieve/pii/S0893608018300674

[75] KIM, Hak Yeong, Kain SEO, Hong Jin JEON, Unjoo LEE and Hyosang LEE. Application of Functional Near-Infrared Spectroscopy to the Study of Brain Function in Humans and Animal Models. *Molecules and Cells.* 2017, **40**(8), 523-532. DOI: 10.14348/molcells.2017.0153. ISSN 1016-8478. Available at: `http://www.molcells.org/journal/view.html?doi=10.14348/molcells.2017.0153`

[76] BOUSHEL, R. and C.A. PIANTADOSI. Near-infrared spectroscopy for monitoring muscle oxygenation. *Acta Physiologica Scandinavica.* 2000, **168**(4), 615-622. DOI: 10.1046/j.1365-201x.2000.00713.x. ISSN 0001-6772. Available at: http://doi.wiley.com/10.1046/j.1365-201x.2000.00713.x

[77] TORRICELLI, Alessandro, Davide CONTINI, Antonio PIFFERI, Matteo CAFFINI, Rebecca RE, Lucia ZUCCHELLI and Lorenzo SPINELLI. Time domain functional NIRS imaging for human brain mapping. *NeuroImage.* 2014, 85, 28-50. DOI:

10.1016/j.neuroimage.2013.05.106. ISSN 10538119. Available at: https://linkinghub.elsevier.com/retrieve/pii/S1053811913006095

[78] SCHOLKMANN, Felix, Stefan KLEISER, Andreas Jaakko METZ, Raphael ZIMMERMANN, Juan MATA PAVIA, Ursula WOLF and Martin WOLF. A review on continuous wave functional near-infrared spectroscopy and imaging instrumentation and methodology. *NeuroImage.* 2014, 85, 6-27. DOI: 10.1016/j.neuroimage.2013.05.004. ISSN 10538119. Available at: https://linkinghub.elsevier.com/retrieve/pii/S1053811913004941

[79] GIACOMETTI, Paolo and Solomon G. DIAMOND. Compliant head probe for positioning electroencephalography electrodes and near-infrared spectroscopy optodes. *Journal of Biomedical Optics.* 2013, **18**(2). DOI: 10.1117/1.JBO.18.2.027005. ISSN 1083-3668. Available at: `http://biomedicaloptics.spiedigitallibrary.org/article.aspx?doi=10.1117/1.JBO.18.2.027005`

[80] CUI, Xu, Signe BRAY, Daniel M. BRYANT, Gary H. GLOVER and Allan L. REISS. A quantitative comparison of NIRS and fMRI across multiple cognitive tasks. *NeuroImage.* 2011, **54**(4), 2808-2821. DOI: 10.1016/j.neuroimage.2010.10.069. ISSN 10538119. Available at: https://linkinghub.elsevier.com/retrieve/pii/S1053811910013777

[81] TOHKA, Jussi, Karin FOERDE, Adam R. ARON, Sabrina M. TOM, Arthur W. TOGA and Russell A. POLDRACK. Automatic independent component labeling for artifact removal in fMRI. *NeuroImage.* 2008, **39**(3), 1227-1245. DOI: 10.1016/j.neuroimage.2007.10.013. ISSN 10538119. Available at: https://linkinghub.elsevier.com/retrieve/pii/S1053811907009482

[82] STRANGMAN, Gary, Joseph P. CULVER, John H. THOMPSON and David A. BOAS. A Quantitative Comparison of Simultaneous BOLD fMRI and NIRS Recordings during Functional Brain Activation. *NeuroImage.* 2002, **17**(2), 719-731. DOI: 10.1006/nimg.2002.1227. ISSN 10538119. Available at: https://linkinghub.elsevier.com/retrieve/pii/S1053811902912279

[83] MEHNERT, Jan. *Evaluation and Optimization of Recent Analytical Approaches for In-Vivo Measurements with Near-Infrared Spectroscopy.* Berlin, 2012. PhD Thesis. Technischen Universitat Berlin.

[84] ARGELAGUET, Ricard, Britta VELTEN, Damien ARNOL, et al. Multi-Omics Factor Analysis—a framework for unsupervised integration of multi-omics data sets. *Molecular Systems Biology.* 2018, **14**(6). DOI: 10.15252/msb.20178124. ISSN 1744-4292. Available at: https://onlinelibrary.wiley.com/doi/abs/10.15252/msb.20178124

[85] MATHYS, Hansruedi, Jose DAVILA-VELDERRAIN, Zhuyu PENG, et al. Single-cell transcriptomic analysis of Alzheimer's disease. *Nature.*

2019, **570**(7761), 332-337. DOI: 10.1038/s41586-019-1195-2. ISSN 0028-0836. Available at: http://www.nature.com/articles/s41586-019-1195-2

[86] ZHANG, Fan, Kevin WEI, Kamil SLOWIKOWSKI, et al. Defining inflammatory cell states in rheumatoid arthritis joint synovial tissues by integrating single-cell transcriptomics and mass cytometry. *Nature Immunology.* 2019, **20**(7), 928-942. DOI: 10.1038/s41590-019-0378-1. ISSN 1529-2908. Available at: http://www.nature.com/articles/s41590-019-0378-1

[87] SÖLLNER, Julia F., German LEPARC, Tobias HILDEBRANDT, Holger KLEIN, Leo THOMAS, Elia STUPKA and Eric SIMON. An RNA-Seq atlas of gene expression in mouse and rat normal tissues. *Scientific Data.* 2017, **4**(1). DOI: 10.1038/sdata.2017.185. ISSN 2052-4463. Available at: http://www.nature.com/articles/sdata2017185

[88] HABIB, Naomi, Yinqing LI, Matthias HEIDENREICH, et al. Div-Seq: Single-nucleus RNA-Seq reveals dynamics of rare adult newborn neurons. *Science.* 2016, **353**(6302), 925-928. DOI: 10.1126/science.aad7038. ISSN 0036-8075. Available at: http://www.sciencemag.org/lookup/doi/10.1126/science.aad7038

[89] SONG, Min, Minseok KANG, Hyeonsu LEE, Yong JEONG and Se-Bum PAIK. Classification of Spatiotemporal Neural Activity Patterns in Brain Imaging Data. *Scientific Reports.* 2018, **8**(1). DOI: 10.1038/s41598-018-26605-z. ISSN 2045-2322. Available at: http://www.nature.com/articles/s41598-018-26605-z

[90] JOHNSTONE, Andrew F.M., Guenter W. GROSS, Dieter G. WEISS, Olaf H.-U. SCHROEDER, Alexandra GRAMOWSKI and Timothy J. SHAFER. Microelectrode arrays: A physiologically based neurotoxicity testing platform for the 21st century. *NeuroToxicology.* 2010, **31**(4), 331-350. DOI: 10.1016/j.neuro.2010.04.001. ISSN 0161813X. Available at: https://linkinghub.elsevier.com/retrieve/pii/S0161813X10000677

[91] VASSALLO, Andrea, Michela CHIAPPALONE, Ricardo DE CAMARGOS LOPES, et al. A multi-laboratory evaluation of microelectrode array-based measurements of neural network activity for acute neurotoxicity testing. *NeuroToxicology.* 2017, 60, 280-292. DOI: 10.1016/j.neuro.2016.03.019. ISSN 0161813X. Available at: https://linkinghub.elsevier.com/retrieve/pii/S0161813X16300419

[92] COLOMBI, Ilaria, Sameehan MAHAJANI, Monica FREGA, Laura GASPARINI and Michela CHIAPPALONE. Effects of antiepileptic drugs on hippocampal neurons coupled to micro-electrode arrays. *Frontiers in Neuroengineering.* 2013, 6. DOI: 10.3389/fneng.2013.00010. ISSN 1662-6443. Available at: http://journal.frontiersin.org/article/10.3389/fneng.2013.00010/abstract

[93] JONES, Ian L., Paolo LIVI, Marta K. LEWANDOWSKA, Michele FISCELLA, Branka ROSCIC and Andreas HIERLEMANN. The potential of microelectrode arrays and microelectronics for biomedical research and diagnostics. *Analytical and Bioanalytical Chemistry.* 2011, **399**(7), 2313-2329. DOI: 10.1007/s00216-010-3968-1. ISSN 1618-2642. Available at: http://link.springer.com/10.1007/s00216-010-3968-1

[94] LEWICKI, Michael S. A review of methods for spike sorting: the detection and classification of neural action potentials. *Network: Computation in Neural Systems.* 2009, **9**(4), R53-R78. ISSN 0954-898X.

[95] ROSSANT, Cyrille, Shabnam N KADIR, Dan F M GOODMAN, et al. Spike sorting for large, dense electrode arrays. *Nature Neuroscience.* 2016, **19**(4), 634-641. DOI: 10.1038/nn.4268. ISSN 1097-6256. Available at: http://www.nature.com/articles/nn.4268

[96] WILSON, Scott B. and Ronald EMERSON. Spike detection: a review and comparison of algorithms. *Clinical Neurophysiology.* 2002, **113**(12), 1873-1881. DOI: 10.1016/S1388-2457(02)00297-3. ISSN 13882457. Available at: https://linkinghub.elsevier.com/retrieve/pii/S1388245702002973

[97] OBIEN, Marie Engelene J., Kosmas DELIGKARIS, Torsten BULLMANN, Douglas J. BAKKUM and Urs FREY. Revealing neuronal function through microelectrode array recordings. *Frontiers in Neuroscience.* 2015, 8. DOI: 10.3389/fnins.2014.00423. ISSN 1662-453X. Available at: http://journal.frontiersin.org/article/10.3389/fnins.2014.00423/abstract

[98] REY, Hernan Gonzalo, Carlos PEDREIRA and Rodrigo QUIAN QUIROGA. Past, present and future of spike sorting techniques. *Brain Research Bulletin.* 2015, 119, 106-117. DOI: 10.1016/j.brainresbull.2015.04.007. ISSN 03619230. Available at: https://linkinghub.elsevier.com/retrieve/pii/S0361923015000684

[99] TIBSHIRANI, Robert, Guenther WALTHER and Trevor HASTIE. Estimating the number of clusters in a data set via the gap statistic. *Journal of the Royal Statistical Society: Series B (Statistical Methodology).* 2001, **63**(2), 411-423. DOI: 10.1111/1467-9868.00293. ISSN 1369-7412. Available at: http://doi.wiley.com/10.1111/1467-9868.00293

[100] NOVAK, D., J. WILD, T. SIEGER and R. JECH. Identifying number of neurons in extracellular recording. *2009 4th International IEEE/EMBS Conference on Neural Engineering.* IEEE, 2009, 2009, 742-745. DOI: 10.1109/NER.2009.5109403. ISBN 978-1-4244-2072-8. Available at: http://ieeexplore.ieee.org/document/5109403/

[101] LINDOVSKÝ, J., K. PYSANENKO, J. POPELÁŘ and J. SYKA. Fast Tonotopy Mapping of the Rat Auditory Cortex With a Custom-Made Electrode Array. *Physiological Research.* 2018, **67**(6), 5726-5741. DOI: 10.33549/physiolres.933835. ISSN 1802-9973.

[102] BENNET, Kevin, Kendall LEE, James KRUCHOWSKI, Su-Youne CHANG, Michael MARSH, Alexander VAN ORSOW, Aurelio PAEZ and Felicia MANCIU. Development of Conductive Boron-Doped Diamond Electrode: A microscopic, Spectroscopic, and Voltammetric Study. *Materials.* 2013, **6**(12), 5726-5741. DOI: 10.3390/ma6125726. ISSN 1996-1944. Available at: http://www.mdpi.com/1996-1944/6/12/5726

[103] RUSINEK, Cory A., Yue GUO, Robert RECHENBERG, Michael F. BECKER, Erin PURCELL, Matthew VERBER, Collin MCKINNEY and Wen LI. All-Diamond Microfiber Electrodes for Neurochemical Analysis. *Journal of The Electrochemical Society.* 2018, **165**(12), G3087-G3092. DOI: 10.1149/2.0141812jes. ISSN 0013-4651. Available at: http://jes.ecsdl.org/lookup/doi/10.1149/2.0141812jes

[104] TYSZCZUK-ROTKO, Katarzyna, Izabela JAWORSKA and Katarzyna JĘDRUCHNIEWICZ. Application of unmodified boron-doped diamond electrode for determination of dopamine and paracetamol. *Microchemical Journal.* 2019, 146, 664-672. DOI: 10.1016/j.microc.2019.01.064. ISSN 0026265X. Available at: https://linkinghub.elsevier.com/retrieve/pii/S0026265X18315960

[105] MATSUBARA, Teruhiko, Michiko UJIE, Takashi YAMAMOTO, Miku AKAHORI, Yasuaki EINAGA and Toshinori SATO. Highly sensitive detection of influenza virus by boron-doped diamond electrode terminated with sialic acid-mimic peptide. *Proceedings of the National Academy of Sciences.* 2016, **113**(32), 8981-8984. DOI: 10.1073/pnas.1603609113. ISSN 0027-8424. Available at: http://www.pnas.org/lookup/doi/10.1073/pnas.1603609113

[106] ZEHANI, Nedjla, Philippe FORTGANG, Mohamed SADDEK LACHGAR, Abdoullatif BARAKET, Madjid ARAB, Sergei V. DZYADEVYCH, Rochdi KHERRAT and Nicole JAFFREZIC-RENAULT. Highly sensitive electrochemical biosensor for bisphenol A detection based on a diazonium-functionalized boron-doped diamond electrode modified with a multi-walled carbon nanotube-tyrosinase hybrid film. *Biosensors and Bioelectronics.* 2015, 74, 830-835. DOI: 10.1016/j.bios.2015.07.051. ISSN 09565663. Available at: https://linkinghub.elsevier.com/retrieve/pii/S0956566315302992

[107] MAYBECK, Vanessa, Robert EDGINGTON, Alexandre BONGRAIN, Joseph O. WELCH, Emanuel SCORSONE, Philippe BERGONZO, Richard B. JACKMAN and Andreas OFFENHÄUSSER. Boron-Doped Nanocrystalline Diamond Microelectrode Arrays Monitor Cardiac Action Potentials. *Advanced Healthcare Materials.* 2014, **3**(2), 283-289. DOI: 10.1002/adhm.201300062. ISSN 21922640. Available at: http://doi.wiley.com/10.1002/adhm.201300062

[108] PIRET, Gaëlle, Clément HÉBERT, Jean-Paul MAZELLIER, et al. 3D-nanostructured boron-doped diamond for microelectrode

array neural interfacing. *Biomaterials.* 2015, 53, 173-183. DOI: 10.1016/j.biomaterials.2015.02.021. ISSN 01429612. Available at: https://linkinghub.elsevier.com/retrieve/pii/S0142961215001313

[109] TAYLOR, A., P. ASHCHEULOV, P. HUBÍK, et al. Precursor gas composition optimisation for large area boron doped nano-crystalline diamond growth by MW-LA-PECVD. *Carbon.* 2018, 128, 164-171. DOI: 10.1016/j.carbon.2017.11.063. ISSN 00086223. Available at: https://linkinghub.elsevier.com/retrieve/pii/S0008622317311776

[110] KRŮŠEK, Jan, Ivan DITTERT, Tereza SMEJKALOVÁ, et al. Molecular Functionalization of Planar Nanocrystalline and Porous Nanostructured Diamond to Form an Interface with Newborn and Adult Neurons. *Physica status solidi (b).* 2019, **256**(3). DOI: 10.1002/pssb.201800424. ISSN 03701972. Available at: http://doi.wiley.com/10.1002/pssb.201800424

[111] WOLF, F. Alexander, Philipp ANGERER and Fabian J. THEIS. SCANPY: large-scale single-cell gene expression data analysis. *Genome Biology.* 2018, **19**(1). DOI: 10.1186/s13059-017-1382-0. ISSN 1474-760X. Available at: https://genomebiology.biomedcentral.com/articles/10.1186/s13059-017-1382-0

[112] STRATTON, Peter, Allen CHEUNG, Janet WILES, Eugene KIY-ATKIN, Pankaj SAH, François WINDELS and Ehsan ARABZADEH. Action Potential Waveform Variability Limits Multi-Unit Separation in Freely Behaving Rats. *PLoS ONE.* 2012, **7**(6). DOI: 10.1371/journal.pone.0038482. ISSN 1932-6203. Available at: https://dx.plos.org/10.1371/journal.pone.0038482

[113] BECHT, Etienne, Leland MCINNES, John HEALY, Charles-Antoine DUTERTRE, Immanuel W H KWOK, Lai Guan NG, Florent GINHOUX and Evan W NEWELL. Dimensionality reduction for visualizing single-cell data using UMAP. *Nature Biotechnology.* 2019, **37**(1), 38-44. DOI: 10.1038/nbt.4314. ISSN 1087-0156. Available at: http://www.nature.com/articles/nbt.4314

[114] KIM, Sunghan and James MCNAMES. Automatic spike detection based on adaptive template matching for extracellular neural recordings. *Journal of Neuroscience Methods.* 2007, **165**(2), 165-174. DOI: 10.1016/j.jneumeth.2007.05.033. ISSN 01650270. Available at: https://linkinghub.elsevier.com/retrieve/pii/S0165027007002634

[115] KUNZINGER, S. Signal recording of 3D neurospheres on high-resolution CMOS MEA platform. *In: PROCEEDINGS OF THE INTERNATIONAL STUDENT SCIENTIFIC CONFERENCE POSTER.* PRAGUE, CZECHIA: Czech Technical University in Prague, 2019, pp. 1-3.

[116] TAYLOR, A., S. SEDLÁKOVÁ, J. KRŮŠEK, O. KLEMPÍŘ, V. BENSON, S. BALUCHOVÁ, K. SCHWARZOVÁ-PECKOVÁ and V. PETRÁKOVÁ. Boron doped diamond based MEAs / microprobes for dual mode neural recording. *In: 30th International Conference on Diamond and Carbon Materials.* SEVILLE, SPAIN: Elsevier, 2019, pp. 1-3.

[117] BALUCHOVÁ, Simona, Andrew TAYLOR, Vincent MORTET, Silvia SEDLÁKOVÁ, Ladislav KLIMŠA, Jaromír KOPEČEK, Ondřej HÁK and Karolina SCHWARZOVÁ-PECKOVÁ. Porous boron doped diamond for dopamine sensing: Effect of boron doping level on morphology and electrochemical performance. *Electrochimica Acta.* 2019, **327**. DOI: 10.1016/j.electacta.2019.135025. ISSN 00134686. Available at: https://linkinghub.elsevier.com/retrieve/pii/S0013468619318961

[118] ALCAIDE, María, Andrew TAYLOR, Morten FJORBACK, Vladimir ZACHAR and Cristian P. PENNISI. Boron-Doped Nanocrystalline Diamond Electrodes for Neural Interfaces: In vivo Biocompatibility Evaluation. *Frontiers in Neuroscience.* 2016, 10. DOI: 10.3389/fnins.2016.00087. ISSN 1662-453X. Available at: http://journal.frontiersin.org/Article/10.3389/fnins.2016.00087/abstract

[119] BAKŠTEIN, Eduard, Tomáš SIEGER, Jiří WILD, Daniel NOVÁK, Jakub SCHNEIDER, Pavel VOSTATEK, Dušan URGOŠÍK and Robert JECH. Methods for automatic detection of artifacts in microelectrode recordings. *Journal of Neuroscience Methods.* 2017, 290, 39-51. DOI: 10.1016/j.jneumeth.2017.07.012. ISSN 01650270. Available at: https://linkinghub.elsevier.com/retrieve/pii/S0165027017302492

[120] CAGNAN, Hayriye, Kevin DOLAN, Xuan HE, et al. Automatic subthalamic nucleus detection from microelectrode recordings based on noise level and neuronal activity. *Journal of Neural Engineering.* 2011, **8**(4). DOI: 10.1088/1741-2560/8/4/046006. ISSN 1741-2560.

[121] FALKENBERG, J.H., J. MCNAMES, M. ABOY and K.J. BURCHIEL. Segmentation of extracellular microelectrode recordings with equal power. *Proceedings of the 25th Annual International Conference of the IEEE Engineering in Medicine and Biology Society (IEEE Cat. No.03CH37439).* IEEE, 2003, , 2475-2478. DOI: 10.1109/IEMBS.2003.1280417. ISBN 0-7803-7789-3. Available at: http://ieeexplore.ieee.org/document/1280417/

[122] ABOY, Mateo and J. Haakon FALKENBERG. An Automatic Algorithm for Stationary Segmentation of Extracellular Microelectrode Recordings. *Medical and Biological Engineering and Computing.* 2006, **44**(6), 511-515. DOI: 10.1007/s11517-006-0052-2. ISSN 0140-0118. Available at: http://link.springer.com/10.1007/s11517-006-0052-2

[123] GUARNIZO, Cristian, Alvaro OROZCO and German CASTELLANOS. Microelectrode Signals Segmentation Using Stationary

Wavelet Transform. *2008 International Conference on BioMedical Engineering and Informatics.* IEEE, 2008, 2008, , 450-454. DOI: 10.1109/BMEI.2008.363. ISBN 978-0-7695-3118-2. Available at: http://ieeexplore.ieee.org/document/4549213/

[124] BAKSTEIN, Eduard, Jakub SCHNEIDER, Tomas SIEGER, Daniel NOVAK, Jiri WILD and Robert JECH. Supervised segmentation of microelectrode recording artifacts using power spectral density. *2015 37th Annual International Conference of the IEEE Engineering in Medicine and Biology Society (EMBC).* IEEE, 2015, 2015, , 1524-1527. DOI: 10.1109/EMBC.2015.7318661. ISBN 978-1-4244-9271-8. Available at: https://ieeexplore.ieee.org/document/7318661/

[125] WEEGINK, Kristian James, Paul A. BELLETTE, John J. VARGHESE, Peter A. SILBURN, Paul A. MEEHAN and Andrew P. BRADLEY. A Parametric Simulation of Neuronal Noise From Microelectrode Recordings. *IEEE Transactions on Neural Systems and Rehabilitation Engineering.* 2017, **25**(1), 4-13. DOI: 10.1109/TNSRE.2016.2573318. ISSN 1534-4320. Available at: http://ieeexplore.ieee.org/document/7480817/

[126] MORAN, Anan, Izhar BAR-GAD, Hagai BERGMAN and Zvi ISRAEL. Real-time refinement of subthalamic nucleus targeting using Bayesian decision-making on the root mean square measure. *Movement Disorders.* 2006, **21**(9), 1425-1431. DOI: 10.1002/mds.20995. ISSN 0885-3185. Available at: http://doi.wiley.com/10.1002/mds.20995

[127] DOLAN, Kevin, H. C. F. MARTENS, P. R. SCHUURMAN and L. J. BOUR. Automatic noise-level detection for extra-cellular microelectrode recordings. *Medical and Biological Engineering and Computing.* 2009, **47**(7), 791-800. DOI: 10.1007/s11517-009-0494-4. ISSN 0140-0118. Available at: http://link.springer.com/10.1007/s11517-009-0494-4

[128] ESTEVA, Andre, Alexandre ROBICQUET, Bharath RAMSUNDAR, et al. A guide to deep learning in healthcare. *Nature Medicine.* 2019, **25**(1), 24-29. DOI: 10.1038/s41591-018-0316-z. ISSN 1078-8956. Available at: http://www.nature.com/articles/s41591-018-0316-z

[129] AL-AJLAN, Amani and Achraf EL ALLALI. CNN-MGP: Convolutional Neural Networks for Metagenomics Gene Prediction. *Interdisciplinary Sciences: Computational Life Sciences.* 2019, **11**(4), 628-635. DOI: 10.1007/s12539-018-0313-4. ISSN 1913-2751. Available at: http://link.springer.com/10.1007/s12539-018-0313-4

[130] BURSA, Miroslav and Lenka LHOTSKA. The Use of Convolutional Neural Networks in Biomedical Data Processing. *Information Technology in Bio- and Medical Informatics.* Cham: Springer International Publishing, 2017, 2017-07-26, , 100-119. Lecture Notes in Computer Science. ISBN 978-3-319-64264-2.

[131] KIETZMANN, Tim C., Patrick MCCLURE and Nikolaus KRIEGESKORTE. *Oxford Research Encyclopedia of Neuroscience.* 2019-01-25. DOI: 10.1093/acrefore/9780190264086.013.46.

[132] VÁSQUEZ-CORREA, J.C., Juan Rafael OROZCO-ARROYAVE and Elmar NÖTH. Convolutional Neural Network to Model Articulation Impairments in Patients with Parkinson's Disease. *Interspeech 2017.* ISCA: ISCA, 2017, 2017-8-20, , 314-318. DOI: 10.21437/Interspeech.2017-1078.

[133] COTE-ALLARD, Ulysse, Cheikh Latyr FALL, Alexandre DROUIN, Alexandre CAMPEAU-LECOURS, Clement GOSSELIN, Kyrre GLETTE, Francois LAVIOLETTE and Benoit GOSSELIN. Deep Learning for Electromyographic Hand Gesture Signal Classification Using Transfer Learning. *IEEE Transactions on Neural Systems and Rehabilitation Engineering.* 2019, **27**(4), 760-771. DOI: 10.1109/TNSRE.2019.2896269. ISSN 1534-4320. Available at: https://ieeexplore.ieee.org/document/8630679/

[134] ACHARYA, U. Rajendra, Shu Lih OH, Yuki HAGIWARA, Jen Hong TAN and Hojjat ADELI. Deep convolutional neural network for the automated detection and diagnosis of seizure using EEG signals. *Computers in Biology and Medicine.* 2018, 100, 270-278. DOI: 10.1016/j.compbiomed.2017.09.017. ISSN 00104825. Available at: https://linkinghub.elsevier.com/retrieve/pii/S0010482517303153

[135] AL RAHHAL, Mohamad M., Yakoub BAZI, Mansour AL ZUAIR, Esam OTHMAN and Bilel BENJDIRA. Convolutional Neural Networks for Electrocardiogram Classification. *Journal of Medical and Biological Engineering.* 2018, **38**(6), 1014-1025. DOI: 10.1007/s40846-018-0389-7. ISSN 1609-0985. Available at: http://link.springer.com/10.1007/s40846-018-0389-7

[136] YILDIRIM, Özal, Paweł PŁAWIAK, Ru-San TAN and U. Rajendra ACHARYA. Arrhythmia detection using deep convolutional neural network with long duration ECG signals. *Computers in Biology and Medicine.* 2018, 102, 411-420. DOI: 10.1016/j.compbiomed.2018.09.009. ISSN 00104825. Available at: https://linkinghub.elsevier.com/retrieve/pii/S0010482518302713

[137] YILDIRIM, Özal. A novel wavelet sequence based on deep bidirectional LSTM network model for ECG signal classification. *Computers in Biology and Medicine.* 2018, 96, 189-202. DOI: 10.1016/j.compbiomed.2018.03.016. ISSN 00104825. Available at: https://linkinghub.elsevier.com/retrieve/pii/S0010482518300738

[138] Convolutional Neural Network. *Deep Learning* [online]. USA: MathWorks, 2018 [cit. 2019-12-19]. Available at: https://www.mathworks.com/solutions/deep-learning/convolutional-neural-network.html

[139] GADHOUMI, Kais, Jean-Marc LINA and Jean GOTMAN. Discriminating preictal and interictal states in patients with temporal lobe epilepsy using wavelet analysis of intracerebral EEG. *Clinical Neurophysiology.* 2012, **123**(10), 1906-1916. DOI: 10.1016/j.clinph.2012.03.001. ISSN 13882457. Available at: https://linkinghub.elsevier.com/retrieve/pii/S1388245712002179

[140] GADHOUMI, Kais, Jean-Marc LINA and Jean GOTMAN. Seizure prediction in patients with mesial temporal lobe epilepsy using EEG measures of state similarity. *Clinical Neurophysiology.* 2013, **124**(9), 1745-1754. DOI: 10.1016/j.clinph.2013.04.006. ISSN 13882457. Available at: https://linkinghub.elsevier.com/retrieve/pii/S1388245713002733

[141] SHARMA, Neha, Vibhor JAIN and Anju MISHRA. An Analysis Of Convolutional Neural Networks For Image Classification. *Procedia Computer Science.* 2018, 132, 377-384. DOI: 10.1016/j.procs.2018.05.198. ISSN 18770509. Available at: https://linkinghub.elsevier.com/retrieve/pii/S1877050918309335

[142] MURPHY, Kevin P. *Machine learning: a probabilistic perspective.* Cambridge, MA: MIT Press, c2012. ISBN 978-0262018029.

[143] JIRUSKA, Premysl, Gerald T. FINNERTY, Andrew D. POWELL, Noosheen LOFTI, Roman CMEJLA and John G. R. JEFFERYS. Epileptic high-frequency network activity in a model of non-lesional temporal lobe epilepsy. *Brain.* 2010, **133**(5), 1380-1390. DOI: 10.1093/brain/awq070. ISSN 1460-2156. Available at: https://academic.oup.com/brain/article-lookup/doi/10.1093/brain/awq070

[144] CASSON, Alexander J., Elena LUNA and Esther RODRIGUEZ-VILLEGAS. Performance metrics for the accurate characterisation of interictal spike detection algorithms. *Journal of Neuroscience Methods.* 2009, **177**(2), 479-487. DOI: 10.1016/j.jneumeth.2008.10.010. ISSN 01650270. Available at: https://linkinghub.elsevier.com/retrieve/pii/S0165027008006110

[145] ROBIN, Xavier, Natacha TURCK, Alexandre HAINARD, Natalia TIBERTI, Frédérique LISACEK, Jean-Charles SANCHEZ and Markus MÜLLER. PROC: an open-source package for R and S to analyze and compare ROC curves. *BMC Bioinformatics.* 2011, **12**(1). DOI: 10.1186/1471-2105-12-77. ISSN 1471-2105. Available at: https://bmcbioinformatics.biomedcentral.com/articles/10.1186/1471-2105-12-77

[146] BOUGHORBEL, Sabri, Fethi JARRAY, Mohammed EL-ANBARI and Quan ZOU. Optimal classifier for imbalanced data using Matthews Correlation Coefficient metric. *PLOS ONE.* 2017, **12**(6). DOI: 10.1371/journal.pone.0177678. ISSN 1932-6203. Available at: https://dx.plos.org/10.1371/journal.pone.0177678

[147] KRIZHEVSKY, Alex, Ilya SUTSKEVER and Geoffrey E. HINTON. ImageNet classification with deep convolutional neural networks. *Communications of the ACM.* 2017, **60**(6), 84-90. DOI: 10.1145/3065386. ISSN 00010782. Available at: http://dl.acm.org/citation.cfm?doid=3098997.3065386

[148] MONTAVON, Grégoire, Geneviève B. ORR and Klaus-Robert MÜLLER, ed. *Neural Networks: Tricks of the Trade.* 2012. DOI: 10.1007/978-3-642-35289-8.

[149] SZEGEDY, Christian, WEI LIU, YANGQING JIA, et al. Going deeper with convolutions. *2015 IEEE Conference on Computer Vision and Pattern Recognition (CVPR).* IEEE, 2015, 2015, , 1-9. DOI: 10.1109/CVPR.2015.7298594. ISBN 978-1-4673-6964-0. Available at: http://ieeexplore.ieee.org/document/7298594/

[150] TALO, Muhammed, Ulas Baran BALOGLU, Özal YILDIRIM and U RAJENDRA ACHARYA. Application of deep transfer learning for automated brain abnormality classification using MR images. *Cognitive Systems Research.* 2019, 54, 176-188. DOI: 10.1016/j.cogsys.2018.12.007. ISSN 13890417. Available at: https://linkinghub.elsevier.com/retrieve/pii/S1389041718310933

[151] ARSALAN, Muhammad, Rizwan NAQVI, Dong KIM, Phong NGUYEN, Muhammad OWAIS and Kang PARK. IrisDenseNet: Robust Iris Segmentation Using Densely Connected Fully Convolutional Networks in the Images by Visible Light and Near-Infrared Light Camera Sensors. *Sensors.* 2018, **18**(5). DOI: 10.3390/s18051501. ISSN 1424-8220. Available at: http://www.mdpi.com/1424-8220/18/5/1501

[152] LLAMAS, Jose, Pedro M. LERONES, Roberto MEDINA, Eduardo ZALAMA and Jaime GÓMEZ-GARCÍA-BERMEJO. Classification of Architectural Heritage Images Using Deep Learning Techniques. *Applied Sciences.* 2017, **7**(10). DOI: 10.3390/app7100992. ISSN 2076-3417. Available at: http://www.mdpi.com/2076-3417/7/10/992

[153] LEAD-DBS. In: *A toolbox facilitating Deep Brain Stimulation electrode reconstructions and computer simulations based on postoperative MRI and CT imaging* [online]. Berlin: Charité – University Medicine, 2016 [cit. 2019-12-19]. Available at: `https://ars.els-cdn.com/content/image/1-s2.0-S1053811914009938-gr3_lrg.jpg`

[154] WONG, S, G H BALTUCH, J L JAGGI and S F DANISH. Functional localization and visualization of the subthalamic nucleus from microelectrode recordings acquired during DBS surgery with unsupervised machine learning. *Journal of Neural Engineering.* 2009, **6**(2). DOI: 10.1088/1741-2560/6/2/026006. ISSN 1741-2560.

[155] OH, Seung-Hyeon, Yu-Ri LEE and Hyoung-Nam KIM. A Novel EEG Feature Extraction Method Using Hjorth Parameter. *International*

Journal of Electronics and Electrical Engineering. 2014, 106-110. DOI: 10.12720/ijeee.2.2.106-110. ISSN 2301380X.

[156] Teager Keiser Energy Operator. In: *Computes the Teager energy operator* [online]. USA: Hooman Sedghamiz, 2014 [cit. 2019-12-19]. Available at: https://www.mathworks.com/matlabcentral/fileexchange/45406-teager-keiser-energy-operator-vectorized

[157] HOLGUIN, Mauricio, German A. HOLGUIN, Hernán Darío Vargas CARDONA, Genaro DAZA, Enrique GUIJARRO and Alvaro OROZCO. Recognition of Brain Structures from MER-Signals Using Dynamic MFCC Analysis and and HMC Classifier. *XIII Mediterranean Conference on Medical and Biological Engineering and Computing 2013.* Cham: Springer International Publishing, 2014, 2014, 742-745. IFMBE Proceedings. DOI: 10.1007/978-3-319-00846-2_184. ISBN 978-3-319-00845-5. Available at: http://link.springer.com/10.1007/978-3-319-00846-2_184

[158] HTK MFCC MATLAB. In: *Mel frequency cepstral coefficient feature extraction* [online]. USA: Kamil Wojcicki, 2011 [cit. 2019-12-19]. Available at: https://www.mathworks.com/matlabcentral/fileexchange/32849-htk-mfcc-matlab?focused=5199998&tab=function

[159] EL KHOULI, Riham H., Katarzyna J. MACURA, Peter B. BARKER, Mohamed R. HABBA, Michael A. JACOBS and David A. BLUEMKE. Relationship of temporal resolution to diagnostic performance for dynamic contrast enhanced MRI of the breast. *Journal of Magnetic Resonance Imaging.* 2009, **30**(5), 999-1004. DOI: 10.1002/jmri.21947. ISSN 10531807. Available at: http://doi.wiley.com/10.1002/jmri.21947

[160] GILAT, Moran, James M SHINE, Courtney C WALTON, Claire O'CALLAGHAN, Julie M HALL and Simon J G LEWIS. Brain activation underlying turning in Parkinson's disease patients with and without freezing of gait: a virtual reality fMRI study. *Npj Parkinson's Disease.* 2015, **1**(1). DOI: 10.1038/npjparkd.2015.20. ISSN 2373-8057. Available at: http://www.nature.com/articles/npjparkd201520

[161] VARRIALE, Pasquale, Antoine COLLOMB-CLERC, Angele VAN HAMME, et al. Decreasing subthalamic deep brain stimulation frequency reverses cognitive interference during gait initiation in Parkinson's disease. *Clinical Neurophysiology.* 2018, **129**(11), 2482-2491. DOI: 10.1016/j.clinph.2018.07.013. ISSN 13882457. Available at: https://linkinghub.elsevier.com/retrieve/pii/S138824571831174X

[162] HUANG, Chuyi, Heling CHU, Yan ZHANG and Xiaoping WANG. Deep Brain Stimulation to Alleviate Freezing of Gait and Cognitive Dysfunction in Parkinson's Disease: Update on Current Research and Future Perspectives. *Frontiers in Neuroscience.* 2018, 12. DOI: 10.3389/fnins.2018.00029. ISSN 1662-453X. Available at: http://journal.frontiersin.org/article/10.3389/fnins.2018.00029/full

[163] WU, Tao, Xiangyu LONG, Liang WANG, Mark HALLETT, Yufeng ZANG, Kuncheng LI and Piu CHAN. Functional connectivity of cortical motor areas in the resting state in Parkinson's disease. *Human Brain Mapping.* 2011, **32**(9), 1443-1457. DOI: 10.1002/hbm.21118. ISSN 10659471. Available at: http://doi.wiley.com/10.1002/hbm.21118

[164] SABATINI, U., K. BOULANOUAR, N. FABRE, et al. Cortical motor reorganization in akinetic patients with Parkinson's disease. *Brain.* 2000, **123**(2), 394-403. DOI: 10.1093/brain/123.2.394. ISSN 1460-2156. Available at: https://academic.oup.com/brain/article-lookup/doi/10.1093/brain/123.2.394

[165] BLINKENBERG, Morten, Christian BONDE, Søren HOLM, Claus SVARER, Jimmy ANDERSEN, Olaf B. PAULSON and Ian LAW. Rate Dependence of Regional Cerebral Activation during Performance of a Repetitive Motor Task: A PET Study. *Journal of Cerebral Blood Flow and Metabolism.* 2016, **16**(5), 794-803. DOI: 10.1097/00004647-199609000-00004. ISSN 0271-678X. Available at: http://journals.sagepub.com/doi/10.1097/00004647-199609000-00004

[166] RAO, S. M., P. A. BANDETTINI, J. R. BINDER, J. A. BOBHOLZ, T. A. HAMMEKE, E. A. STEIN and J. S. HYDE. Relationship between Finger Movement Rate and Functional Magnetic Resonance Signal Change in Human Primary Motor Cortex. *Journal of Cerebral Blood Flow and Metabolism.* 2016, **16**(6), 1250-1254. DOI: 10.1097/00004647-199611000-00020. ISSN 0271-678X. Available at: http://journals.sagepub.com/doi/10.1097/00004647-199611000-00020

[167] SADATO, Norihiro, Vicente IBAÑEZ, Marie-Pierre DEIBER, Gregory CAMPBELL, Marc LEONARDO and Mark HALLETT. Frequency-Dependent Changes of Regional Cerebral Blood Flow during Finger Movements. *Journal of Cerebral Blood Flow and Metabolism.* 2016, **16**(1), 23-33. DOI: 10.1097/00004647-199601000-00003. ISSN 0271-678X. Available at: http://journals.sagepub.com/doi/10.1097/00004647-199601000-00003

[168] KAWASHIMA, R., K. INOUE, M. SUGIURA, K. OKADA, A. OGAWA and H. FUKUDA. A positron emission tomography study of self-paced finger movements at different frequencies. *Neuroscience.* 1999, **92**(1), 107-112. DOI: 10.1016/S0306-4522(98)00744-1. ISSN 03064522. Available at: https://linkinghub.elsevier.com/retrieve/pii/S0306452298007441

[169] MARTINU, Kristina, Atsuko NAGANO-SAITO, Stuart FOGEL, Oury MONCHI and Véronique SGAMBATO-FAURE. Asymmetrical Effect of Levodopa on the Neural Activity of Motor Regions in PD. *PLoS ONE.* 2014, **9**(11). DOI: 10.1371/journal.pone.0111600. ISSN 1932-6203. Available at: http://dx.plos.org/10.1371/journal.pone.0111600

[170] CEBALLOS-BAUMANN, Andrés O., Henning BOECKER, Peter BARTENSTEIN, Isabella VON FALKENHAYN, Herrmann RIESCHER, Bastian CONRAD, Jean R. MORINGLANE and François ALESCH. A Positron Emission Tomographic Study of Subthalamic Nucleus Stimulation in Parkinson Disease. *Archives of Neurology.* 1999, **56**(8). DOI: 10.1001/archneur.56.8.997. ISSN 0003-9942. Available at: `http://archneur.jamanetwork.com/article.aspx?doi=10.1001/archneur.56.8.997`

[171] LIMOUSIN, Patricia, John GREENE, Pierre POLLAK, John ROTHWELL, Alim-Louis BENABID and Richard FRACKOWIAK. Changes in cerebral activity pattern due to subthalamic nucleus or internal pallidum stimulation in Parkinson's disease. *Annals of Neurology.* 1997, **42**(3), 283-291. DOI: 10.1002/ana.410420303. ISSN 0364-5134. Available at: http://doi.wiley.com/10.1002/ana.410420303

[172] PIPER, Sophie K., Arne KRUEGER, Stefan P. KOCH, Jan MEHNERT, Christina HABERMEHL, Jens STEINBRINK, Hellmuth OBRIG and Christoph H. SCHMITZ. A wearable multi-channel fNIRS system for brain imaging in freely moving subjects. *NeuroImage.* 2014, 85, 64-71. DOI: 10.1016/j.neuroimage.2013.06.062. ISSN 10538119. Available at: https://linkinghub.elsevier.com/retrieve/pii/S1053811913007003

[173] DEROSIÈRE, G., F. ALEXANDRE, N. BOURDILLON, K. MANDRICK, T.E. WARD and S. PERREY. Similar scaling of contralateral and ipsilateral cortical responses during graded unimanual force generation. *NeuroImage.* 2014, 85, 471-477. DOI: 10.1016/j.neuroimage.2013.02.006. ISSN 10538119. Available at: https://linkinghub.elsevier.com/retrieve/pii/S1053811913001262

[174] WILSON, Tony W., Max J. KURZ and David J. ARPIN. Functional specialization within the supplementary motor area: A fNIRS study of bimanual coordination. *NeuroImage.* 2014, 85, 445-450. DOI: 10.1016/j.neuroimage.2013.04.112. ISSN 10538119. Available at: https://linkinghub.elsevier.com/retrieve/pii/S1053811913004795

[175] MORISHITA, Takashi, Masa-aki HIGUCHI, Kazuya SAITA, Yoshio TSUBOI, Hiroshi ABE and Tooru INOUE. Changes in Motor-Related Cortical Activity Following Deep Brain Stimulation for Parkinson's Disease Detected by Functional Near Infrared Spectroscopy: A Pilot Study. *Frontiers in Human Neuroscience.* 2016, 10. DOI: 10.3389/fnhum.2016.00629. ISSN 1662-5161. Available at: http://journal.frontiersin.org/article/10.3389/fnhum.2016.00629/full

[176] SAKATANI, K., Y. KATAYAMA, T. YAMAMOTO and S. SUZUKI. Changes in cerebral blood oxygenation of the frontal lobe induced by direct electrical stimulation of thalamus and globus pallidus: a near infrared spectroscopy study. *Journal of Neurology, Neurosurgery and Psy-*

chiatry. 1999, **67**(6), 769-773. DOI: 10.1136/jnnp.67.6.769. ISSN 0022-3050. Available at: http://jnnp.bmj.com/cgi/doi/10.1136/jnnp.67.6.769

[177] BICK, Sarah K. B., Bradley S. FOLLEY, Jutta S. MAYER, et al. Subthalamic Nucleus Deep Brain Stimulation Alters Prefrontal Correlates of Emotion Induction. *Neuromodulation: Technology at the Neural Interface.* 2017, **20**(3), 233-237. DOI: 10.1111/ner.12537. ISSN 10947159. Available at: http://doi.wiley.com/10.1111/ner.12537

[178] MIYAI, Ichiro, Hiroki C. TANABE, Ichiro SASE, et al. Cortical Mapping of Gait in Humans: A Near-Infrared Spectroscopic Topography Study. *NeuroImage.* 2001, **14**(5), 1186-1192. DOI: 10.1006/nimg.2001.0905. ISSN 10538119. Available at: https://linkinghub.elsevier.com/retrieve/pii/S105381190190905X

[179] PERREY, Stephane. Possibilities for examining the neural control of gait in humans with fNIRS. *Frontiers in Physiology.* 2014, 5. DOI: 10.3389/fphys.2014.00204. ISSN 1664-042X. Available at: http://journal.frontiersin.org/article/10.3389/fphys.2014.00204/abstract

[180] MAIDAN, Inbal, Freek NIEUWHOF, Hagar BERNAD-ELAZARI, et al. The Role of the Frontal Lobe in Complex Walking Among Patients With Parkinson's Disease and Healthy Older Adults. *Neurorehabilitation and Neural Repair.* 2016, **30**(10), 963-971. DOI: 10.1177/1545968316650426. ISSN 1545-9683. Available at: http://journals.sagepub.com/doi/10.1177/1545968316650426

[181] COPE, M. and D. T. DELPY. System for long-term measurement of cerebral blood and tissue oxygenation on newborn infants by near infra-red transillumination. *Medical and Biological Engineering and Computing.* 1988, **26**(3), 289-294. DOI: 10.1007/BF02447083. ISSN 0140-0118. Available at: http://link.springer.com/10.1007/BF02447083

[182] KRUPICKA, Radim, Slavka VITECKOVA, Vaclav CEJKA, Ondrej KLEMPIR, Zoltan SZABO and Evzen RUZICKA. BradykAn: A motion capture system for objectification of hand motor tests in Parkinson Disease. *2017 E-Health and Bioengineering Conference (EHB).* IEEE, 2017, 2017, 446-449. DOI: 10.1109/EHB.2017.7995457. ISBN 978-1-5386-0358-1. Available at: http://ieeexplore.ieee.org/document/7995457/

[183] FAZLI, Siamac, Jan MEHNERT, Jens STEINBRINK, Gabriel CURIO, Arno VILLRINGER, Klaus-Robert MÜLLER and Benjamin BLANKERTZ. Enhanced performance by a hybrid NIRS–EEG brain computer interface. *NeuroImage.* 2012, **59**(1), 519-529. DOI: 10.1016/j.neuroimage.2011.07.084. ISSN 10538119. Available at: https://linkinghub.elsevier.com/retrieve/pii/S1053811911008792

[184] TAK, Sungho and Jong Chul YE. Statistical analysis of fNIRS data: A comprehensive review. *NeuroImage.* 2014, 85, 72-91.

DOI: 10.1016/j.neuroimage.2013.06.016. ISSN 10538119. Available at: https://linkinghub.elsevier.com/retrieve/pii/S1053811913006538

[185] ZHANG, Xian, Jack Adam NOAH and Joy HIRSCH. Separation of the global and local components in functional near-infrared spectroscopy signals using principal component spatial filtering. *Neurophotonics.* 2016, **3**(1). DOI: 10.1117/1.NPh.3.1.015004. ISSN 2329-423X. Available at: `http://neurophotonics.spiedigitallibrary.org/article.aspx?doi=10.1117/1.NPh.3.1.015004`

[186] PETERSON, Daniel S., Kristen A. PICKETT, Ryan P. DUNCAN, Joel S. PERLMUTTER and Gammon M. EARHART. Brain activity during complex imagined gait tasks in Parkinson disease. *Clinical Neurophysiology.* 2014, **125**(5), 995-1005. DOI: 10.1016/j.clinph.2013.10.008. ISSN 13882457. Available at: https://linkinghub.elsevier.com/retrieve/pii/S1388245713011292

[187] KOENRAADT, Koen L.M., Eefje G.J. ROELOFSEN, Jacques DUYSENS and Noël L.W. KEIJSERS. Cortical control of normal gait and precision stepping: An fNIRS study. *NeuroImage.* 2014, 85, 415-422. DOI: 10.1016/j.neuroimage.2013.04.070. ISSN 10538119. Available at: https://linkinghub.elsevier.com/retrieve/pii/S1053811913004175

[188] YE, J, S TAK, K JANG, J JUNG and J JANG. NIRS-SPM: Statistical parametric mapping for near-infrared spectroscopy. *NeuroImage.* 2009, **44**(2), 428-447. DOI: 10.1016/j.neuroimage.2008.08.036. ISSN 10538119. Available at: https://linkinghub.elsevier.com/retrieve/pii/S1053811908009695

[189] XU, Jingping, Xiangyu LIU, Jinrui ZHANG, Zhen LI, Xindi WANG, Fang FANG and Haijing NIU. FC-NIRS: A Functional Connectivity Analysis Tool for Near-Infrared Spectroscopy Data. *BioMed Research International.* 2015, 2015, 1-11. DOI: 10.1155/2015/248724. ISSN 2314-6133. Available at: http://www.hindawi.com/journals/bmri/2015/248724/

[190] CHANG, Pyung-Hun, Seung-Hee LEE, Kwang-Min GU, Seung-Hyun LEE, Sang-Hyun JIN, Sang Seok YEO, Jeong Pyo SEO and Sung Ho JANG. The cortical activation pattern by a rehabilitation robotic hand: a functional NIRS study. *Frontiers in Human Neuroscience.* 2014, 8. DOI: 10.3389/fnhum.2014.00049. ISSN 1662-5161. Available at: `http://journal.frontiersin.org/article/10.3389/fnhum.2014.00049/abstract`

[191] BAE, Sung Jin, Sung Ho JANG, Jeong Pyo SEO and Pyung Hun CHANG. The Optimal Speed for Cortical Activation of Passive Wrist Movements Performed by a Rehabilitation Robot: A Functional NIRS Study. *Frontiers in Human Neuroscience.* 2017, 11. DOI: 10.3389/fnhum.2017.00194. ISSN 1662-5161. Available at: http://journal.frontiersin.org/article/10.3389/fnhum.2017.00194/full

[192] KLEMPÍŘ, Ondřej and Radim KRUPIČKA. MACHINE LEARNING USING SPEECH UTTERANCES FOR PARKINSON DISEASE DETECTION. *Lekar a technika – Clinician and Technology.* 2018, **48**(2), 66–71.

[193] VITECKOVA, Slavka, Ondrej KLEMPIR, Petr DUSEK, Radim KRUPICKA, Zoltan SZABO and Evžen RŮŽIČKA. Statistical analysis of the 180 degree walking turn: Common patterns, repeatability and prediction bands of turn signals. *Biomedical Signal Processing and Control.* 2020, 56. DOI: 10.1016/j.bspc.2019.101689. ISSN 17468094. Available at: https://linkinghub.elsevier.com/retrieve/pii/S1746809419302708

[194] HANNIGAN, Geoffrey D, David PRIHODA, Andrej PALICKA, et al. A deep learning genome-mining strategy for biosynthetic gene cluster prediction. *Nucleic Acids Research.* 2019, **47**(18), e110-e110. DOI: 10.1093/nar/gkz654. ISSN 0305-1048. Available at: https://academic.oup.com/nar/article/47/18/e110/5545735

[195] *Equipment for tremor measurement and analysis in patients with nervous system diseases.* Available at: `https://isdv.upv.cz/webapp/resdb.print_detail.det?pspis=PUV/36514`

[196] TUKEY, John Wilder. *Exploratory data analysis.* Reading, Mass.: Addison-Wesley Pub. Co., c1977. ISBN 978-0201076165.

[197] HUANG, Chih-Wei, Richard LU, Usman IQBAL, et al. A richly interactive exploratory data analysis and visualization tool using electronic medical records. *BMC Medical Informatics and Decision Making.* 2015, **15**(1). DOI: 10.1186/s12911-015-0218-7. ISSN 1472-6947. Available at: `http://bmcmedinformdecismak.biomedcentral.com/articles/10.1186/s12911-015-0218-7`

[198] MATSUDA, Yoshio, Tomoko MANAKA, Makiko KOBAYASHI, Shuhei SATO and Michitaka OHWADA. Exploratory analysis of textual data from the Mother and Child Handbook using the text-mining method: Relationships with maternal traits and post-partum depression. *Journal of Obstetrics and Gynaecology Research.* 2016, **42**(6), 655-660. DOI: 10.1111/jog.12971. ISSN 13418076. Available at: http://doi.wiley.com/10.1111/jog.12971

[199] MORI, Etsuro, Manabu IKEDA, Kenya NAKAI, Hideaki MIYAGISHI, Masaki NAKAGAWA and Kenji KOSAKA. Increased plasma donepezil concentration improves cognitive function in patients with dementia with Lewy bodies: An exploratory pharmacokinetic/pharmacodynamic analysis in a phase 3 randomized controlled trial. *Journal of the Neurological Sciences.* 2016, 366, 184-190. DOI: 10.1016/j.jns.2016.05.001. ISSN 0022510X. Available at: https://linkinghub.elsevier.com/retrieve/pii/S0022510X16302465

[200] The problem with p-values. In: *Aeon* [online]. London: Aeon Media Group, 2016 [cit. 2019-12-19]. Available at: https://aeon.co/essays/it-s-time-for-science-to-abandon-the-term-statistically-significant

[201] Experts issue warning on problems with P values. In: *ScienceNews* [online]. Washington: Tom Siegfried, 2016 [cit. 2019-12-19]. Available at: sciencenews.org/blog/context/experts-issue-warning-problems-p-values

[202] Reactivity: An overview. In: *R Shiny* [online]. Boston: RStudio, 2017 [cit. 2019-12-19]. Available at: https://shiny.rstudio.com/articles/reactivity-overview.html

Appendices

Appendix A

NeuroEDA – an Interactive Web Tool for Neuroinformatics Data Analysis

This subchapter points out an interactive web application NeuroEDA, which implements current R packages and model making procedures and has been developed for the evaluation of neurological data analyses in the form of a BioData product. The presented software tool is a result of co-authorship between the author of this thesis and his bachelor student Bc. Laura Shala.

Several methods were implemented for dataset exploratory analysis:

- graph visualizations, using the "ggplot2" package: e.g. boxplot, histogram, scatter plot,
- interactive correlation analysis + kernel density estimation using the "Ggally" package,
- k-means algorithm for finding compact clusters in data,
- simple regression analysis with an independent and dependent variable using least squares method,
- locally weighted regression using the "ggplot2" package – able to find nonlinear trends, suitable for detection of rapid dropdowns or other interventions,
- robust regression using the "robust" package – lower sensibility to outliers, represents linear models with smaller counts of observations better than the least squares regression method,
- the mclust - package provides models and methods to estimate the number of clusters in the multivariate dataset. The algorithm uses 10 models to calculate default 1 to 10 Gaussian Mixture Model (GMM) components (clusters) and Bayesian Information Criterion (BIC) to select final optimal number of clusters.

The most beneficial clinical property of the NeuroEDA related to this thesis is the mclust package (Normal Mixture Modeling for Model-Based

Clustering, Classification, and Density Estimation), which is practically used in our neuroinformatics research to automatically determine the number of clusters in the 2D data and for the subsequent classification, including the quantification of the uncertainty of the decision algorithm. In short, the number of detected clusters represent the number of neurons in the MER (for details see the Chapter 4).

A.1 Introduction

Exploratory data analysis (EDA) has been systematically studied from the age of statistician John W. Tukey. In his book (1977), EDA was defined as a statistical method for finding interesting hypotheses and relations in data [196]. It was mainly about the graphical techniques of data representation: boxplots, histograms, scatter plots or manually calculated analysis of principal components etc. Deep analysis of data integrity and the variance of values, correlations and i.e. groups of discrimination in data, plays a key role in pre-processing and the subsequent creation of descriptive and predictive models. EDA is even more important in medicine, typically for small dataset counts or due to outlier observations.

Research and the application of EDA methods are constantly progressing and this progress reflects the rapid rise of the importance of areas related to computational data analysis and data science in general. The number of scientific papers from all data science fields grows every year in the Web of Science (WoS). Recent medical examples of EDA progress are, for instance, in application for electronic medical records [197], text mining in obstetrics [198] or methodology in neurosciences [199].

Despite the mathematical nature and recommended methods, modern EDA is a form of art and an expression of the author/analyst's creativity. Creativity and the authors knowledge in the form of various packages, tools and libraries can easily be integrated into the work of biomedical software programmers. The creation of a precise, and compendious graph is in many cases more efficient than inductive analysis based on p-values. Current statistical studies point to an excessive or automated problem of statistical significance usage by p-values in medicine and psychology [200, 201]. Visual analysis (visual mining) seems to be an appropriate alternative to inductive statistics.

A.2 Design

The application was developed because of the need for an integrating interface with new statistical methods for biomedical data analysis at our department. It was programmed using the open source programming language R, which is a significant member in the statistical computing field. The app kernel is based on Shiny framework, standing on the reactive programming paradigm [202].

Reactive programming was designed, above all, to simplify interactive user interface creations. The Shiny application is composed of two main parts, the user (ui.R) in the form of a webpage, and the server part (server.R). Within Shiny, reactivity is provided by reactive inputs and outputs. Typical input is the user's demand with a web interface. For example, picking one of several form choices, filling out the text field or clicking on a button. These actions set parameters, with which the application immediately reacts by rendering an output (graph display, table operation etc.). It can be executed on a local server and used within a web browser. The user controls the application within the user interface, and sends requests to the server, where computations are made and outputs are updated (Fig. A.1).

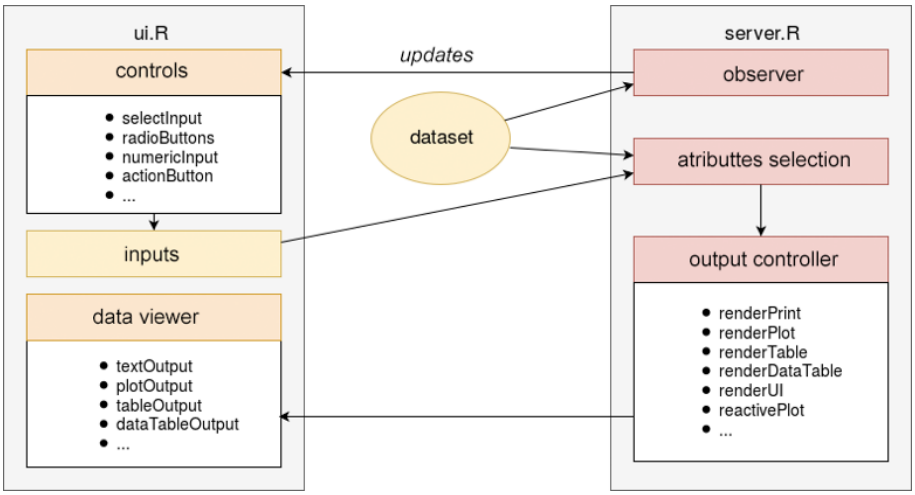

Figure A.1: A simple object-oriented NeuroEDA model.

This application allows the user to import data in the .csv format. A file is chosen in the file system. It is possible to change a delimiter (comma, semicolon, tab) and turn the header on or off. Basic information is reactively displayed after uploading the dataset. The user can see basic attribute summaries or view datasets as a table, with paginating, sorting, filtering and searching options (Fig. A.2).

The program is composed of five functional units: Upload, Summary, Table, Plotting and Analysis. It operates in graphical user interfaces (GUI). Four basic plots implemented in NeuroEDA are: BIC plot (Fig. A.3, A.4), classification plot, uncertainty plot and density plot. In the case of BIC plot, you can see results of Bayesian criterion for each model and each calculated number of components. Case with the highest BIC is selected and data are classified according to it, visualised on the classification plot. Uncertainty plot provides view on the measure of the quality of the classification. Circles on classification and uncertainty plots correspond to the covariances of the components. If you assume more than 9 clusters in your data, or if you can see rising trend beyond 9 components in various models in the BIC plot, you can select higher maximum number of components.

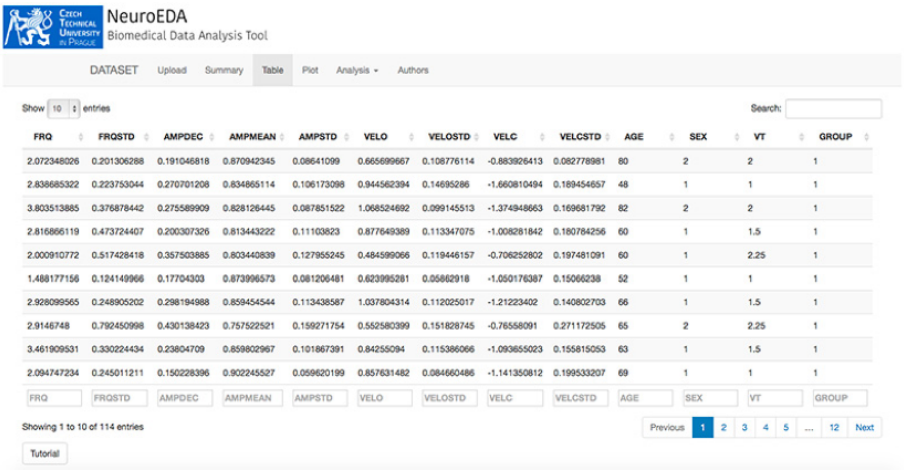

Figure A.2: View on NeuroEDA application environment with imported data and table visualization.

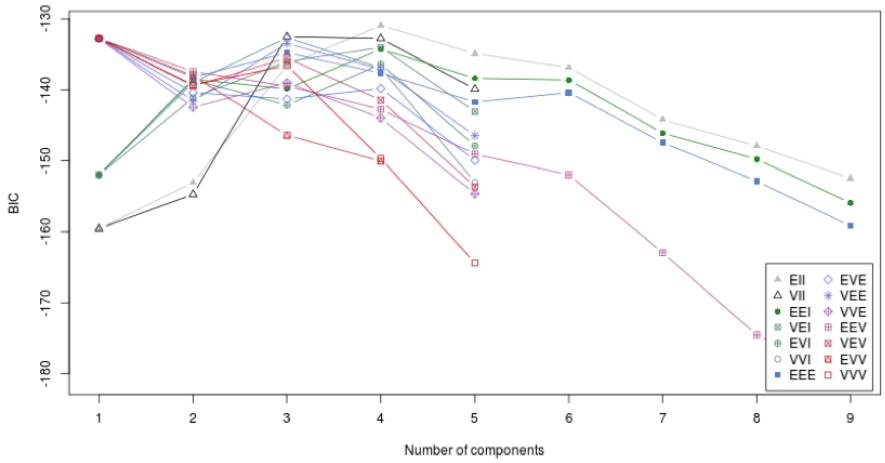

Figure A.3: BIC diagram example. The highest BIC is at number 4.

identifier	Model	HC	EM	Distribution	Volume	Shape	Orientation
E		•	•	(univariate)	equal		
V		•	•	(univariate)	variable		
EII	λI	•	•	Spherical	equal	equal	NA
VII	λ_k I	•	•	Spherical	variable	equal	NA
EEI	λA		•	Diagonal	equal	equal	coordinate axes
VEI	$\lambda_k A$		•	Diagonal	variable	equal	coordinate axes
EVI	λA_k		•	Diagonal	equal	variable	coordinate axes
VVI	$\lambda_k A_k$		•	Diagonal	variable	variable	coordinate axes
EEE	λDAD^T	•	•	Ellipsoidal	equal	equal	equal
EEV	$\lambda D_k A D_k^T$		•	Ellipsoidal	equal	equal	variable
VEV	$\lambda_k D_k A D_k^T$		•	Ellipsoidal	variable	equal	variable
VVV	$\lambda_k D_k A_k D_k^T$	•	•	Ellipsoidal	variable	variable	variable

Figure A.4: Models used to classify data. mclust version 4 for R: Normal Mixture Modeling for Model-Based Clustering, Classification, and Density Estimation.

Title	Description
GROUP	group membership: = 1 (disease)
SEX	sex: = 1 (female)
VT	expert rating (numeric)
FRQ	mean tapping frequency [Hz]
FRQSTD	FRQ standard deviation (std) [Hz]
AMPDEC	amplitude decrease of fingers distance [cm]
AMPMEAN	mean amplitude of fingers distance [cm]
AMPSTD	std amplitude of fingers distance [cm]
VELO	finger opening velocity [m/s]

Table A.1: Title and description of selected features from finger tapping measurements.

A.3 Testing Case: Clinical Neurology Dataset

The application was tested on several publicly accessible datasets of various extent (i.e. iris, mtcars of "datasets" package). Moreover, it was used for clinical neurological dataset exploratory data analysis of camera system measurements (Fig. A.5). Records represent parameters of periodic hand movements, or finger tapping (FT). FT stands for repetitive touching of a thumb and a forefinger following maximal expansion, as fast as possible. Measurements were taken in healthy controls (N = 59) and PD patients (N = 55). An overview of the selected features is shown in the table (Table A.1).

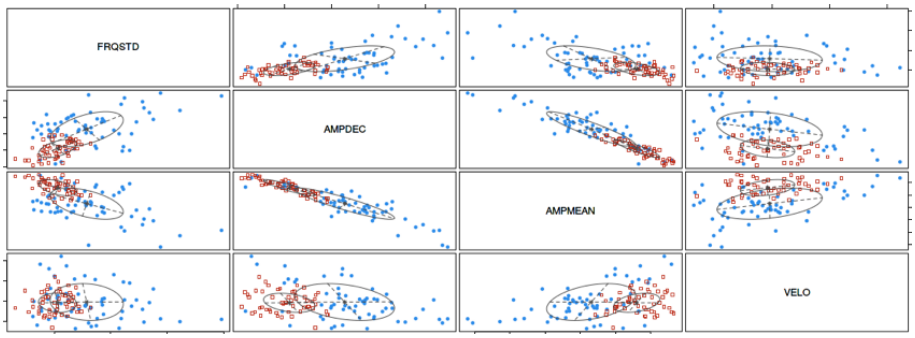

Figure A.5: Graphs showing clusters according to multidimensional analysis among variables FRQSTD, AMPDEC, AMPMEAN, and VELO based on GMM (mclust library).

Ways of working with the neurological dataset in NeuroEDA application are depicted in the process map (Fig. A.6). It is clearly visible, that based on FRQ and VELO parameters, it is possible to automatically distinguish between patients and healthy subjects, using k-means algorithm (two groups with an unsupervised separation).

The example of a visually found hypothesis by linear and robust regression methods has a practical importance. It was discovered that there is a difference between healthy vs. patient's groups considering a regression

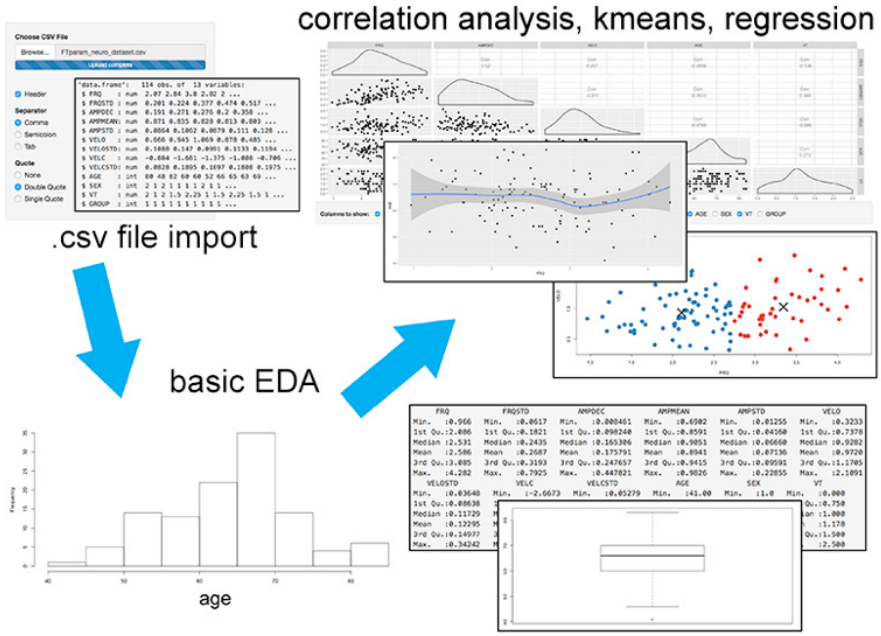

Figure A.6: NeuroEDA workflow.

model. The tapping frequency parameter (FRQ) on how an expert evaluates a patient's condition has a significantly greater impact in the group of patients. Moreover, an expert is much more focused on finger tapping frequency than in a healthy group (in which case the expert is most likely considering some other parameter).

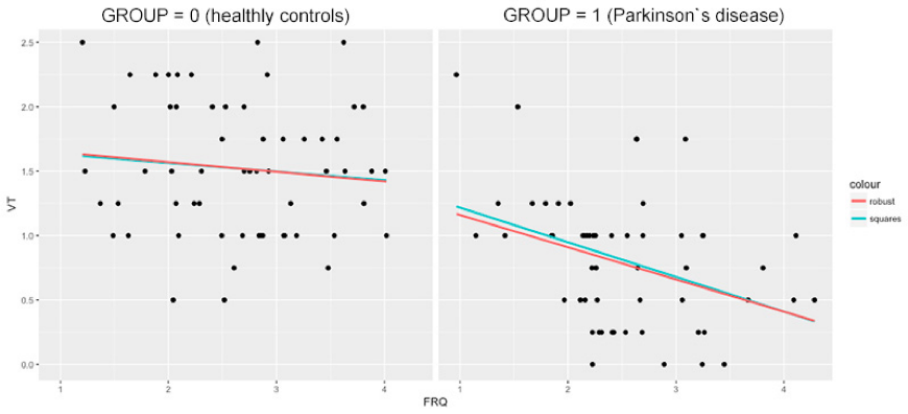

Figure A.7: Example of visually discovered clinical hypothesis by NeuroEDA: the FRQ parameter has a greater impact on expert assessment in the patients group.

A.4 Discussion and Conclusion

NeuroEDA application is an easy to use software developed by biomedical engineers. Its outstanding feature, which makes it different from all existing statistical software, is its quick extendibility with new available statistical R packages on demand. The application provides immediate response, even in cases with bigger data files. Functionality was also successfully tested in commonly used web browsers (Google Chrome, Safari, Mozilla Firefox, Internet Explorer). The main advantage of the application is the availability of robust regression and the mclust package, that are not usually contained in available commercial statistical programmes and are crucial for statistical evaluation of our biomedical data. The usage of the interactive interface allows for working with R functions without any scripting knowledge, therefore it offers usage by non-technical clinic staff. The application is still in an alpha version and is continuously tested and extended with new functions. We are considering direct connection to the database which stores data from various neurophysiological examinations, which is likewise developed at our department. Besides table data analysis modules, we also work on the module for analysing time series, according to new measured signals and hypotheses specified by medical doctors. In our opinion, the desktop version of Shiny NeuroEDA is capable of absorbing the high dimensional data and to analysing it efficiently. A web application, which implements various methods for exploratory data analysis was created. NeuroEDA can be executed without the need of programming knowledge. The application is actively used for neurological data assessment and discovering of potentially useable hypotheses. NeuroEDA Shiny demo app is available at `https://neuroeda.shinyapps.io/neuroeda/` and released under the MIT License.

Appendix B

List of Publications

B.1 The Dissertation Consists of the Following Impacted Articles

- KLEMPÍŘ, Ondřej, Radim KRUPIČKA, Eduard BAKŠTEIN and Robert JECH. Identification of Microrecording Artifacts with Wavelet Analysis and Convolutional Neural Network: An Image Recognition Approach. *Measurement Science Review.* 2019, **19**(5), 222-231. DOI: 10.2478/msr-2019-0029. ISSN 1335-8871. *WoS, Scopus.*

  IF (2018) = 1.12; SJR (2018): Q2 in Control and Systems Engineering

- KLEMPIR, Ondrej, Radim KRUPICKA, Jan MEHNERT, et al. Reshaping cortical activity with subthalamic stimulation in Parkinson's disease during finger tapping and gait mapped by near infrared spectroscopy. *Journal of Applied Biomedicine.* 2019, **17**(3), 157-166. DOI: 10.32725/jab.2019.014. ISSN 1214021X. *WoS, Scopus.*

  IF (2018) = 1.57; SJR (2018): Q2 in Pharmacology, Toxicology, Pharmaceutics

- KLEMPÍŘ, O., R. KRUPIČKA and R. JECH. Microelectrode Neuronal Activity of the Internal Globus Pallidus in Dystonia Correlates with Postoperative Neuromodulation Effects and Placement of the Stimulation Electrode. *IRBM.* 2019, **40**(4), 193-200. DOI: 10.1016/j.irbm.2019.05.006. ISSN 19590318. *WoS, Scopus.*

  IF (2018) = 0.93; SJR (2018): Q3 in Biomedical Engineering

- KLEMPÍŘ, O., R. KRUPIČKA, J. KRŮŠEK, I. DITTERT, V. PETRÁKOVÁ, V. PETRÁK and A. TAYLOR. Application of Spike Sorting Algorithm to Neuronal Signals Originated from Boron Doped Diamond Microelectrode Arrays. *Physiological Research. WoS, Scopus.*

  Accepted for publication.

  IF (2018) = 1.70; SJR (2018): Q2 in Medicine

B.2 Articles in Peer-Reviewed Journals

- KLEMPÍŘ, Ondřej and Radim KRUPIČKA. An Analysis of Neural Activity of the Human Basal Ganglia in Dystonia: A Review. *Lekar a technika – Clinician and Technology.* 2019, **49**(2), 66–71. *Scopus.*

  SJR (2018): Q4 in Biophysics

- KLEMPÍŘ, Ondřej and Radim KRUPIČKA. Machine Learning Using Speech Utterances for Parkinson Disease Detection. *Lekar a technika – Clinician and Technology.* 2018, **48**(2), 66–71. *Scopus.*

  SJR (2017): Q4 in Biophysics

- KLEMPÍŘ, Ondřej, Radim KRUPIČKA and Robert JECH. Median Method for Determining Cortical Brain Activity in a Near Infrared Spectroscopy Image. *Lekar a technika – Clinician and Technology.* 2018, **48**(1), 11–16. *Scopus.*

  SJR (2017): Q4 in Biophysics

- KLEMPÍŘ, Ondřej, Laura SHALA, Jan TESAŘ and Radim KRUPIČKA. NeuroEDA – an interactive web tool for neuroinformatics data analysis and teaching biomedical statistics. *MEFANET Journal.* 2017, **5**(2), 62–68. *ERIH PLUS.*

B.3 Other Method-Relevant Publications in Journals with Impact Factor

- KRUPIČKA, Radim, Stanislav MAREČEK, Christiane MALÁ, et al. Automatic substantia nigra segmentation in neuromelanin-sensitive MRI by deep neural network in patients with prodromal and manifest synucleinopathy. *Physiological Research. WoS, Scopus.*

  Accepted for publication.

  IF (2018) = 1.70; SJR (2018): Q2 in Medicine

- VITECKOVA, Slavka, Ondrej KLEMPIR, Petr DUSEK, Radim KRUPICKA, Zoltan SZABO and Evžen RŮŽIČKA. Statistical analysis of the 180 degree walking turn: Common patterns, repeatability and prediction bands of turn signals. *Biomedical Signal Processing and Control.* 2020, 56. DOI: 10.1016/j.bspc.2019.101689. ISSN 17468094. *WoS, Scopus.*

  IF (2018) = 2.94; SJR (2018): Q2 in Health Informatics

- HANNIGAN, Geoffrey D, David PRIHODA, Andrej PALICKA, et al. A deep learning genome-mining strategy for biosynthetic gene cluster prediction. *Nucleic Acids Research.* 2019, **47**(18), e110-e110. DOI: 10.1093/nar/gkz654. ISSN 0305-1048. *WoS, Scopus.*

  IF (2018) = 11.14; SJR (2018): Q1 in Genetics

B.4 Proceedings Excerpted in WoS/Scopus

- VÍTEČKOVÁ, Slávka, Radim KRUPIČKA, Tereza DUSPIVOVÁ, Ondřej KLEMPÍŘ, Jan TESAŘ, Zoltán SZABO and Evžen RŮŽIČKA. Maximal velocity and amplitude decrement angle: a novel parameter for finger tapping instrumental evaluation in Parkinson disease. *Gait and Posture.* 2019, **73**(Supplement 1), 474-475. DOI: 10.1016/j.gaitpost.2019.07.158. ISSN 09666362. *WoS, Scopus.*

- KLEMPÍŘ, Ondřej, Radim KRUPIČKA, Vladimíra PETRÁKOVÁ, Jan KRŮŠEK, Ivan DITTERT and Andrew TAYLOR. Automated Neurons Recognition and Sorting for Diamond Based Microelectrode Arrays Recording: A Feasibility Study. In: World Congress on Medical Physics and Biomedical Engineering 2018. Singapore: Springer Singapore, 2019, 2019-05-30, 281-286. IFMBE Proceedings. DOI: 10.1007/978-981-10-9038-7_52. ISBN 978-981-10-9037-0. *WoS, Scopus.*

- ČEJKA, V., A. FEČÍKOVÁ, O. KLEMPÍŘ, R. KRUPIČKA and R. JECH. System for Motor Evoked Potentials Acquisition and Analysis. In: *World Congress on Medical Physics and Biomedical Engineering 2018.* Singapore: Springer Singapore, 2019, 2019-05-30, 87-91. IFMBE Proceedings. DOI: 10.1007/978-981-10-9023-3_16. ISBN 978-981-10-9022-6. *WoS, Scopus.*

- KLEMPIR, Ondrej, Radim KRUPICKA, Vaclav CEJKA and Robert JECH. Microelectrode Neuronal Activity Biomarker of the Internal Globus Pallidus in Dystonia Correlates with Long-term Neuromodulation Effects. In: 2018 IEEE 20th International Conference on e-Health Networking, Applications and Services (Healthcom). IEEE, 2018, 2018, 1-6. DOI: 10.1109/HealthCom.2018.8531122. ISBN 978-1-5386-4294-8. *Scopus.*

  Excellent Paper Award.

- KLEMPÍŘ, O., R. KRUPIČKA, J. MEHNERT, et al. P 024 - Near-infrared spectroscopy patterns of cortical activity during gait in Parkinson's disease patients treated with DBS STN. *Gait and Posture.* 2018, 65, 273-275. DOI: 10.1016/j.gaitpost.2018.06.181. ISSN 09666362. *WoS, Scopus.*

- KRUPICKA, Radim, Slavka VITECKOVA, Vaclav CEJKA, Ondrej KLEMPIR, Zoltan SZABO and Evzen RUZICKA. BradykAn: A motion capture system for objectification of hand motor tests in Parkinson Disease. In: *2017 E-Health and Bioengineering Conference (EHB).* IEEE, 2017, 2017, 446-449. DOI: 10.1109/EHB.2017.7995457. ISBN 978-1-5386-0358-1. *WoS, Scopus.*

B.5 Other Publications

- KLEMPÍŘ, O., R. KRUPIČKA, T. SIEGER and R. JECH. P07-Automatic pallidal neurons recognition based on the detection of the number of clusters from microrecordings in dystonia. *Clinical Neurophysiology.* 2018, **129**(4), e15-e16. DOI: 10.1016/j.clinph.2018.01.052. ISSN 13882457. **Abstract and poster presentation.**

- KLEMPÍŘ, Ondřej and Radim KRUPIČKA. Analysis of Neural Activity of the Human Basal Ganglia in Dystonia: A Review. In: *The Eighth Young Biomedical Engineers and Researchers Conference YBERC 2018.* Košice: Technical University of Košice, 2018. **Oral presentation.**

- ČEJKA, Václav, Anna FEČÍKOVÁ, Ondřej KLEMPÍŘ and Radim KRUPIČKA. Detekce polohy motorických evokovaných potenciálů v MATLABU. In: *BYRON, P., ed. 24 th Annual Conference Proceedings Technical Computing Prague 2017.* Praha: HUMUSOFT s.r.o, 2017, s. 1-5. ISBN 978-80-7592-002-7. ISSN 2336-1662. **Poster presentation.**

- KLEMPÍŘ, Ondřej, Radim KRUPIČKA and Robert JECH. Analýza aktivity jednotlivých neuronů u lidských bazálních ganglií metodami strojového učení. In: *Zpracování, vizualizace a dolování dat z pohledu rozhodovacích procesů. Letní škola matematické biologie 2017.* Brno: Institut biostatistiky a analýz, 2017, s. 14-17. ISBN 978-80-210-8692-0.

  1st place in the competition for the best publication and oral presentation.

- KLEMPÍŘ, Ondřej, Václav ČEJKA, Jan TESAŘ and Radim KRUPIČKA. Pokroky v analýze heterogenních neuroinformatických dat. In: Data a znalosti 2017. Plzeň: Západočeská univerzita v Plzni, 2017, s. 157-161. ISBN 978-80-261-0720-0. **Poster presentation.**

- KLEMPÍŘ, Ondřej, Radim KRUPIČKA and Robert JECH. Stanovení aktivity kortikálních oblastí mozku v obrazu blízké infračervené spektroskopie. In: *Trendy v biomedicínském inženýrství 2017.* Ostrava: VŠB-TUO, 2017. ISBN 978-80-248-4099-4. **Oral presentation.**

- KLEMPÍŘ, Ondřej, Laura SHALA and Radim KRUPIČKA. NEUROEDA – interaktivní webová aplikace pro hodnocení neurologických dat. In: *MEDSOFT 2017.* Roztoky u Prahy: Creative Connections, 2017, s. 50-56. ISBN 978-80-86742-47-2. ISSN 1803-8115. **Oral presentation.**

- KLEMPÍŘ, Ondřej and Vojtěch KALÁB. Automatic Discovery of Hypotheses in Nuclear Cardiology. In: *Proceedings of the International Student Scientific Conference Poster.* Prague: Czech Technical University in Prague, 2017. ISBN 978-80-01-06153-4. **Poster presentation.**

- KLEMPÍŘ, Ondřej, Radim KRUPIČKA, Petr ŠMÍD, Zoltán SZABÓ and Libor SEIDL. Simulation Environment for Healthcare Message Integration in the Teaching of Hospital Information Systems at FBME CTU. In: Mefanet 2016. Brno: Masarykova univerzita, 2016. **Poster presentation.**
- KLEMPÍŘ, Ondřej, Václav ČEJKA, Jan MEHNERT, et al. P-36 Aktivita motorického kortexu ve vztahu k hybnosti při DBS STN u Parkinsonovy nemoci v obraze NIRS. *Česká a slovenská neurologie a neurochirurgie: 30. český a slovenský neurologický sjezd.* Česká lékařská společnost J. E. Purkyně, 2016. ISSN 1210-7859. **Poster presentation.**
- VÍTEČKOVÁ, Slávka, Radim KRUPIČKA, Ondřej KLEMPÍŘ, Zoltán SZABÓ, Hana VAŇKOVÁ, Martina KUCKIR and Iva HOLMEROVÁ. Software Suite for Data Collection and Processing in Long-term Care. *International Journal on Biomedicine and Healthcare.* EuroMISE, 2016, **4**(2), 35–41. ISSN 1805-8698. **Journal article.**
- KLEMPÍŘ, Ondřej, Radim KRUPIČKA and Robert JECH. Study of the DBS STN Effect on Parkinson's Disease Finger Tapping Using NIRS. In: *16th Conference on Human Biomechanics 2016.* Kladno: Faculty of biomedical engineering, Department of natural sciences, 2016. ISBN 9788001060391. **Oral presentation.**

Appendix C

List of Abbreviations

AC/PC Anterior Commissure/Posterior Commissure
AKE Adjusted Clinical Effect
APS Atypical Parkinsonian Syndromes
AUC Area Under Curve
BDD Boron Dopped Diamond
BG Basal Ganglia
BIC Bayesian Information Criterion
BPF Band Pass Filtering
BOLD Blood Oxygen Level Dependent
BFMDS Burke-Fahn-Marsden Dystonia Scale
CNN Convolutional Neural Network
COV autocorrelation-based approach
CT Computed Tomography
CV Coefficient of Variation
CWT Continuous Wavelet Transform
DBS Deep Brain Stimulation
DYT1 Early-Onset Torsion Dystonia
EDA Exploratory Data Analysis
EEG Electroencefalography
FT Finger Tapping
GUI Graphical User Interface
HbO, oxyHb oxyhemoglobin
HR Hemodynamic Response
fMRI Functional Magnetic Resonance Imaging
fNIRS Functional Near Infrared Spectroscopy

FOG Freezing of Gait

GC Gap Criterion

GMM Gaussian Mixture Model

GPi Globus Pallidus internus

GPe Globus Pallidus externus

ICA Independent Component Analysis

ICC Intra Class Correlation

LFP Local Field Potentials

M1 Primary Motor Cortex

MCC Matthews Correlation Coefficient

MEA MicroElectrode Array

MER, microEEG Microelectrode Recording

MNI Montreal Neurological Institute

MRI Magnetic Resonance Imaging

PC Parietal Cortex

PD Parkinson's Disease

PFC Prefrontal Cortex

PCA Principal Component Analysis

PMC Premotor Cortex

PSD Power Spectral Density

ROC Receiver Operating Characteristic

RMS Root Mean Square

S1 Somatosensory Area

SC Single Cell

SMA Supplementary Motor Area

STN Subthalamic Nucleus

TIN Titanium Nitride

TWSTRS Toronto Western Spasmodic Torticollis Scale

UMAP Uniform Manifold Approximation and Projection

UPDRS Unified Parkinson's Disease Rating Scale

WoS Web of Science